UC Berkeley
UC Berkeley Electronic Theses and Dissertations

Title
Elevated Temperature Small Scale Mechanical Testing of Uranium Dioxide

Permalink
https://escholarship.org/uc/item/6tk128sm

Author
Frazer, David

Publication Date
2018

Peer reviewed|Thesis/dissertation

eScholarship.org Powered by the California Digital Library
University of California

Elevated Temperature Small Scale Mechanical Testing of Uranium Dioxide

By

David Michael Frazer

A dissertation submitted in partial satisfaction of the requirements for the degree of

Doctor of Philosophy

in

Engineering- Nuclear Engineering

in the

Graduate Division

of the

University of California, Berkeley

Thesis committee:

Professor Peter Hosemann, Chair

Professor Andrew Minor

Professor Massimiliano Fratoni

Professor Per Peterson

Summer 2018

Elevated Temperature Small Scale Mechanical Testing of Uranium Dioxide

Copyright © 2018

By

David Michael Frazer

Abstract

Elevated Temperature Small Scale Mechanical Testing of Uranium Dioxide

By

David Michael Frazer

Doctor of Philosophy in Engineering – Nuclear Engineering

University of California, Berkeley

Professor Peter Hosemann, Chair

In an effort to increase the understanding of the mechanical properties of UO_2 small scale mechanical testing techniques were developed at room and elevated temperature. The small scale mechanical testing techniques, such as micro cantilever testing and nanoindentation, focused on measuring the elastic and creep properties of the UO_2 at room and elevated temperature. The elastic and creep properties of UO_2 are important for pellet clad mechanical interactions during service in a reactor. During the lifetime of a reactor the fuel swells and the cladding creeps down onto the fuel which causes them to come into contact. Due to the elastic anisotropy of the UO_2 this can lead to failures in the cladding and the release of radioactive material. In addition, the creep of the UO_2 fuel is important during this contact as it a mechanism to relive stress in the cladding and fuel.

This work used small scale mechanical testing to measure the elastic and creep properties at room and elevated temperature. Microcantilever testing was performed ex-situ and in-situ in a scanning electron microscopy and transmission electron microscopy to measure the fracture stress and elastic modulus of the material over temperature. It was observed that when the microcantilevers had a ratio of (length/height) > 5 the elastic modulus values matched well with literature values. In addition, the microcantilevers measured higher values of fracture stress as compared with bulk sample as the microcantilevers had little to no porosity in the microcantilever. The measured values for the room temperature in-situ microcantilevers were in the 3-4 GPa range. While having little to no porosity the microcantilevers still exhibited a large spread in the results. Tests were performed on a single crystal with different loading orientations to measure the elastic anisotropy in the UO_2. The results of the measurements show agreement between the experimental measured values and the theoretical values. The in-situ scanning electron microscope testing was also performed at elevated temperature in a reducing environment to measure the change in the elastic modulus values and fracture stress. The need for a reducing environment is because UO_2 can further oxide to U_3O_8. The elastic modulus values measured at elevated temperature show good agreement with literature values. The in-situ transmission electron microscope testing showed that there was no dislocation motion at room temperature in the UO_2. There was additional

microcantilever testing to evaluate the effects of the microstructure on the calculated elastic modulus values of the UO_2.

In addition to the microcantilever testing, nanoindentation was also performed on the UO_2 fuel at room evaluated temperature on a variety of different samples. The two main studies performed with nanoindentation were to measure the effect of grain size on the hardness of the UO_2 and to evaluate the effect of pre-straining the UO_2 material at elevated temperature. The grains size study had 3 UO_2 samples manufactured with spark plasma sintering with three different grain sizes (125 nm, 2 μm, and 10 μm) to evaluate the change in hardness of the samples. The 125 nm grain size sample had the highest hardness and maintained it hardness the best over the temperature range tested. The elastic modulus values measured with nanoindentation on all three samples agree with literature values. A sample was pre-strained prior to testing to evaluate the effects of an increased defect density in the sample. The pre-strained sample had a lower hardness and higher nanoindentation creep rates as compared with the un-strained results.

In summary this work demonstrates that small scale mechanical testing can be used to evaluate the mechanical properties of UO_2 at room and elevated temperature and that these techniques have the ability to be applied to irradiated UO_2 fuel.

This dissertation is dedicated to my parents, Richard and Sherri.

Acknowledgements

I would like to start off by thanking my advisor Professor Peter Hosemann for dealing with my antics for the last 5 years of graduated school and during my undergraduate time at UC Berkeley. His advice and constructive suggestions have made a better scientist.

I would also like to thank my thesis committee; Professor Peter Hosemann, Professor Andrew Minor, Professor Massimiliano Fratoni, and Professor Per Peterson, for their guidance through the experimental process and suggestions on this thesis.

I would also like to thank the institutions which were instrumental in my scientific development; The University of California at Berkeley, Los Alamos National Laboratory, Lawrence Berkeley National Laboratory, Biomolecular Nanotechnology Center, Nuclear Science User Facilities, National Center for Electron Microscopy, Idaho National Laboratory, Arizona State University.

This research would not have been possible with various funding sources that supported me during my graduate career. This work was supported by the DOE-NEUP award entitled "*Mechanical Behavior of UO_2 at Sub-grain Length Scales: Quantification of Elastic, Plastic and Creep Properties via Microscale Testing"* award number DE-NE0000670, Nuclear Science User Facilities with rapid turnaround proposals, and the National Center for Electron Microscopy (Work at the Molecular Foundry was supported by the Office of Science, Office of Basic Energy Sciences, of the U.S. Department of Energy under Contract No. DE-AC02-05CH11231).

I would also like to extend my gratitude to all of my fellow graduate students that offered advice during my graduate studies Scott Parker, Ashley Reichardt, Amanda Lupinacci, Madicken Munk, Hi Vo, Evan Still, Joey Kabel, David Krumwiede, Cameron Howard, Rachel Traylor, Anya Prasitthipayong, Thomas Pekin, Nathan Velez, Julian Sabisch, Claire Chisholm, Milos Atz, James Kendrick, Ryan Pavlovsky, Kelly Rowland, Alex Salazar III, Franziska Schmidt, Patricia Schuster, Joanna Szornel, Maria Simanovskaia, Samantha Lewis, Fei Teng, Chris Perovicky.

I would also to extend my gratitude to all of those have assisted and offered advice during my graduate studies; Andrew Minor, Per Peterson, Massimiliano Fratoni, Eric Norman, Rachel Slaybaugh, Christina Castellanos, AJ Gubser, Kirsten Hall, Pedro Peralta, Mark Asta, Daniel Jardenas, Mitch Meyer, Jeffery Giglio, Cheng Sun, Jason Harp, James Madden and all of those who have helped me along the way.

I have also to thank all of the people that made time during my graduate studies entrainment and keep me going during; Monika Haoui, Kari Leigh, Katie Robinson, Jacob Moe-Lange, Noah Horowitz, Katie Brown, Megan Ryan, Zach Sklar, Jonny Lee, Mary Dawason, and much of Ski Team (Cal Ski Team # 1).

I have to express my thanks to the water fountain in Cory which always had the coldest and most refreshing water and to La Val's for all of the weekly research discussions.

I would also to express, which is not possible in words, my thanks to my family who have supported me throughout my life. I promise to get a real "job" soon.

Table of Contents

List of Figures

List of Tables

Chapter 1
Introduction

1.1 Nuclear Background

Nuclear Energy

Today, nuclear energy provides 20% of United States and 11% of the world's electrical energy need [1, 2]. This is a significant and vital part of the electricity generation in the United States. In addition, nuclear energy is a low carbon source of base load electrical energy. Currently, nuclear power plants are being shut down in the United States due to the operational and maintenance costs and cheap, abundant natural gas supply form fracking in the United States. There have been some efforts to consider the low carbon emission of power production via nuclear power plants. However, in order for nuclear power to maintain/gain ground in the energy market in the Unites States the cost of producing nuclear electricity is going to have to decrease. Currently small modular reactors are looking to revive the nuclear industry in the United States by lowering the construction (capital) costs. NuScale, a small modular reactor company, plans on building their new small modular reactor design at Idaho National Laboratory with producing power to the grid in 2027. This will be a first test to see if small modular reactors can bring down the construction cost/overnight costs of nuclear reactors allowing them to compete against natural gas.

Low Carbon Source of Electricity

After the major accidents of Three Mile Island (United States, 1979) and Chernobyl (Ukraine, 1986) along with the political and environmental pressures from these accidents caused the stagnation of nuclear power in the United States, however; with the concerns of greenhouses gas, carbon emissions and global warming nuclear power is making a revival in the United States and can be part of the energy future [3-5]. A new commercial nuclear power plant is being built in the Unites States for the first time in over 30 years at Vogtle [6]. Even with the setbacks of the Fukushima accident (Japan, 2011) nuclear power is still gaining in popularity worldwide and viewed as low carbon source of electricity [7, 8]. In addition, nuclear energy is rapidly being built in countries such as China, Russia and Indian to combat pollution challenges form electrical production form coal and other fossil fuels in those locations [9-13]. The accident in Fukushima also raised questions about accident tolerant nuclear fuel systems and increased the research in both the cladding and fuel for nuclear reactors [14, 15]. The research outline later in this dissertation is examining the currently used UO_2 fuel to see if improvements can be made to increase the safety of today nuclear reactors. It is the belief of many that nuclear energy should have a place in combatting greenhouse gas, carbon and pollution worldwide in the coming future.

Development of New Reactors

Since the Chicago pile in December of 1942 nuclear energy has had a profound effect on the world from being a low carbon source of electricity to nuclear weapons [16]. From the Chicago Pile there have been 4 recognized generations of nuclear reactors. An image of the Chicago Pile can be seen in Figure 1.1. Generation I reactors were prototype and civilian power nuclear reactors developed in the 1950s to 1960s. These were generally proof of concept reactors and had lower power levels [17]. The reactors in generation II were a commercial class of reactor or reactors that designed to be reliable and economical with operating lifetimes of 40 years [17]. Generation II reactors were started to be built in the late 1960s and compromise the majority of the operating commercial reactors today [17]. An image of a generation II nuclear power plant can be seen in Figure 1.2. Generation III nuclear reactors are similar to generation II nuclear reactors, however; they contain state-of-the-art design improvements in the areas of fuel technology, thermal efficiency, modularized construction, safety systems and standardized design [17]. In addition, generation III reactors are also designed for lifetimes of 60 years and beyond [17]. Generation III also includes reactors known as generation III+ which are reactors that offer significant improvements in safety over generation III reactors designs that were licensed by the NRC in the 1990s. The major improvements were in passive safety systems that do not require operator involvement and instead rely on gravity or natural convection to mitigate accident scenarios [17]. An example of a generation III+ nuclear reactor would be the Westinghouse AP1000 design. Generation IV reactors are alternative types of nuclear reactors that still require considerable fundamental research [17] and could possibly be ready for commercialization in 20-30 years. These types of reactors includes high temperature reactors, liquid metal cooled reactors, traveling or stationary wave reactors, gas cooled reactors or liquid salt cooled reactors [17]. A few possible designs for generation IV nuclear reactors are shown in Figure 1.3. Lastly Figure 1.4 shows the evolutions of reactors that have been discussed in this section. One of the challenges with the development of the next generation of nuclear power plants is the performance of materials in the harsh operating environments. The performance and degradation of materials in current and proposed reactors are a limiting factor in their operation and development. Generation IV reactors are being designed for higher operating temperature, larger irradiation damage to materials, and exotic coolants that have new corrosion conditions [17-19]. The push for this new operating conditions will require a large amount of research into the development of more damage tolerant materials and into degradation in the operating conditions. The irradiation and corrosion testing of materials is expensive and would require a large amount of samples to be tested in order to cover the range of operating conditions. A way to increase the information and reduce the amount of material needed to be tested is to use small scale mechanical testing. Small scale mechanical testing can gather more information from a single specimen as compared to macro-scale testing which could reduce the amount of samples needed. The benefits and consideration of small scale mechanical testing will be examined in more depth later in the chapter.

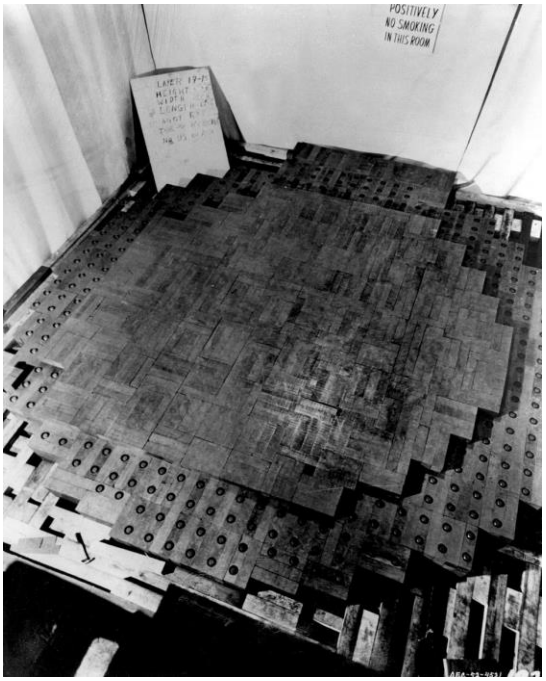

Figure 1.1: An image of the Chicago Pile 1 midway through construction [20].

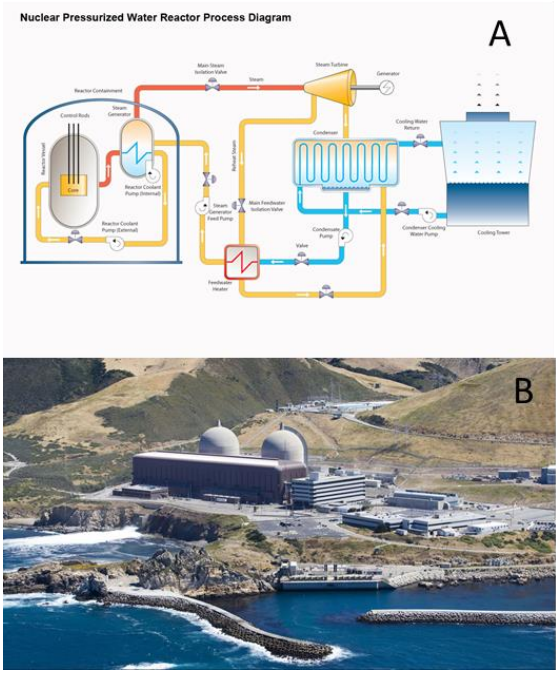

Figure 1.2: A) A cartoon of a Generation II nuclear power plant for energy production [21]. B) The Diablo Canyon power plant in California which is a generation II reactor design [22].

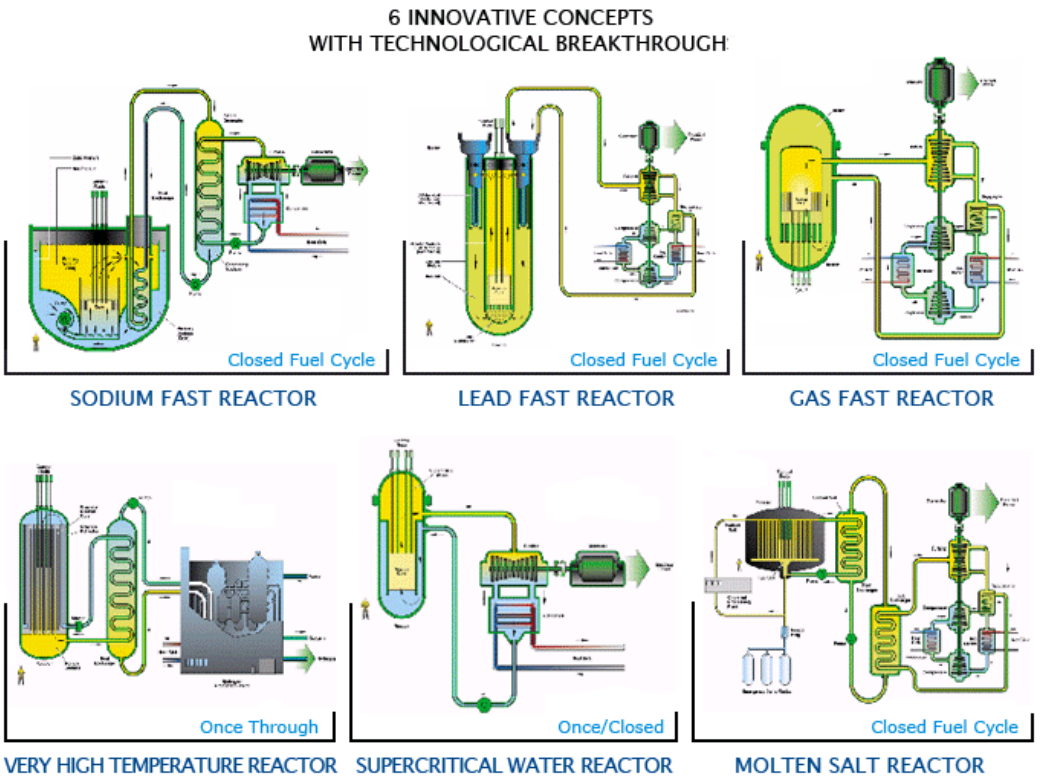

Figure 1.3: Six examples of possible generation IV nuclear reactors that are under research and development [23].

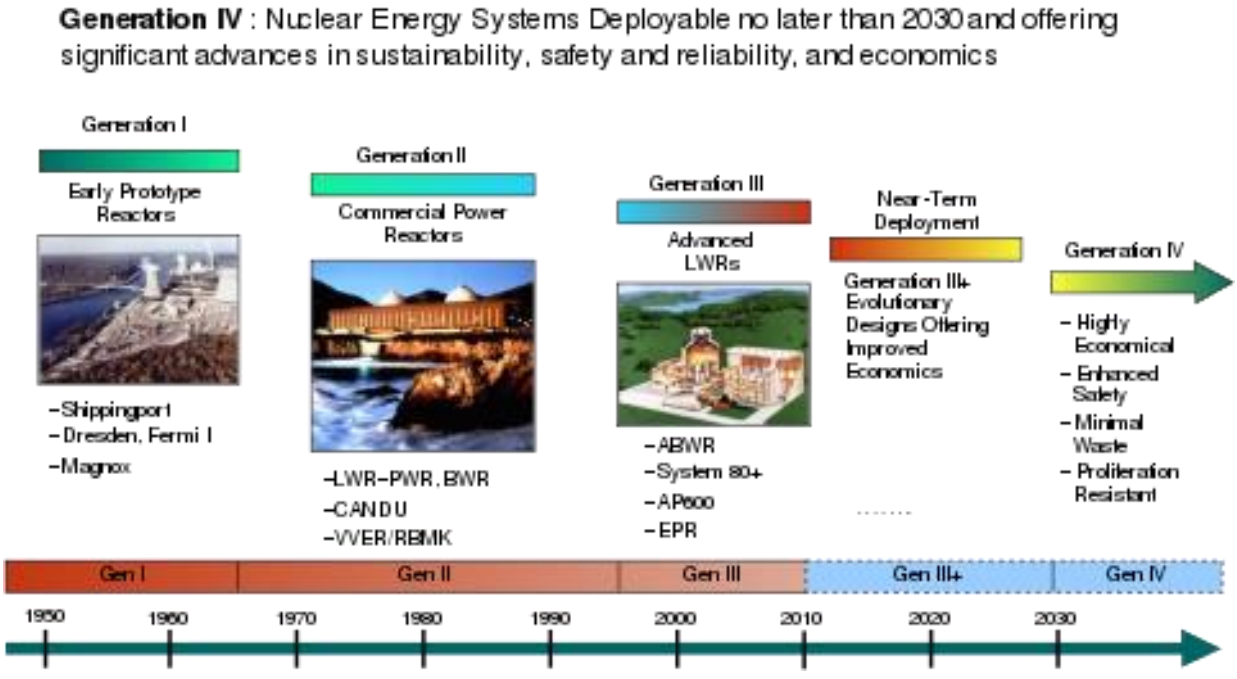

Figure 1.4: The evolution and future predictions of nuclear reactors [24].

1.2 Uranium Dioxide (UO_2) Background

The Manufacturing and Enriching Process for UO_2

The average concentration of uranium in the ground is around 2.5 ppm and it is known to be in over 200 mineral forms [25]. The uranium in the earth's crust is made up of 3 isotopes which are U-238 (99.3 %), U-235 (0.7%) and U-234 (0.006 %) [25]. The first step in manufacturing UO_2 for use in nuclear reactors is mining the uranium-containing ores. This is normally only economical when there is a relatively high level present. The highest grade ores contain 17-18% (200,000 ppm) which are found in only two deposits in Canada. The typical high-grade ore contains around 2% uranium (20,000 ppm), whereas low-grade ore contains 0.1% uranium (1000 ppm) [25]. The ore is processed by crushing and grinding it in order to release the uranium mineral particles [25]. The uranium is then captured in solution, often sulfuric acid. This captured uranium is then extracted from the acid to produce a solid oxide (U_3O_8) which is called yellow cake [25]. The yellow cake is subsequently sent to fuel manufacturers. Most reactors operating today require the fuel to be enriched to up to 5% U-235 as compared with the natural enrichment of U-235 of 0.7 %. There are some reactors that can operate on U-235 concentration in natural uranium. The two most common enrichment processes are gaseous diffusion and gas centrifuge enrichment [25]. In both processes the solid U_3O_8 (yellow cake) needs to first be converted into uranium hexafluoride UF_6. The gaseous diffusion process relies on the slightly different diffusion rates of U-235 and U-238 through a porous membrane to create a stream of gas that is richer in one isotope than the other. A schematic of the gaseous diffusion enrichment process is shown in Figure 1.5. The gas centrifuge enrichment exploits the rather small difference in mass between the two uranium isotopes to enrich the fuel. A schematic of a gas centrifuge can be seen in Figure 1.6. The gas centrifuge method is the preferred method of enrichment because it is quicker and less energy-intensive than the gaseous diffusion process [25]. Once the enrichment to the desired level has been completed the UF_6 is converted to UO_2. After this the UO_2 is then pressed into pellets that are sintered at high temperature to create the fuel pellets that are used in nuclear reactors. The rods are then used in the nuclear reactor until they have been exhausted and removed from the reactor and become spent fuel. The spent fuel rods are then moved to spent fuel pool where they will spend 2-4 years before moving to dry cask storage.

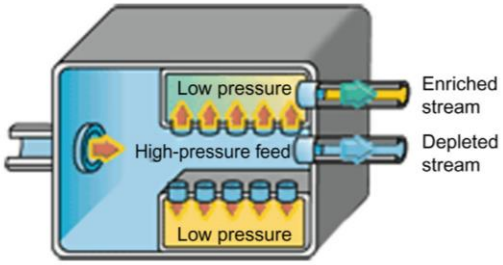

Figure 1.5: A schematic of the gaseous diffusion process [25]. Gaseous diffusion is based on Graham's law, which states that the rate of effusion of a gas is inversely proportional to the square root of it's molecular mass [26].

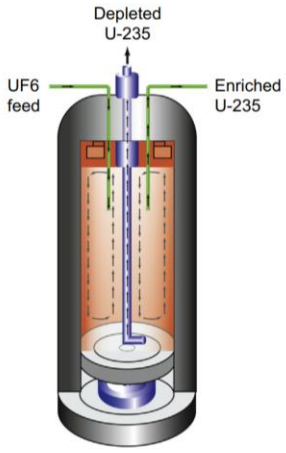

Figure 1.6: A schematic of a centrifuge for enrichment of uranium [25]. The centrifuge uses the force results from the centripetal acceleration to separate materials according to their mass. The denser molecules move towards the wall and the lighter ones remain close to the center.

Sintering

Consolidation of powders at $T > 0.5T_m$ by diffusional mass transport leading to the formation of a dense body is called sintering. Sintering involves the preparation of a powder blend (powder + binder or sinter additive) followed by compaction and consolidation at high temperature. This process takes a sample from a porous state to a state of dense material and it must involve the process of neck formation and growth [27]. The process of sintering can broadly be classified into two categories: 1) Liquid phase sintering and 2) Solid-state sintering (SSS). This section will focus on SSS as this process used to manufacture UO_2 for both commercial reactors and laboratory experimental settings. In SSS the liquid phase does no form and the entirety of the solid-solid and solid-vapor interfacial areas are replaced by only solid-solid interfacial areas. In SSS the sintering process is purely by diffusional processes inducing the neck growth [27]. The thermodynamic driving force for sintering is the reduction of surface energy of the system by solid-solid and solid-vapor interfacial areas being replaced by only solid-solid interracial areas. In SSS there are three distinguishable stages which can be identified as: 1) initial stage, characterized by neck formation at the interparticle region; 2) intermediate stage, characterized by neck growth leading to interconnected pore channel formation and dynamic removal of pores, leading to breakdown of continuous pore channel; and 3) final stage, characterized by achieving nearly theoretical density with isolated pores [27]. A cartoon of particles necking and reduction of pores can be seen in Figure 1.7. An illustration of the relative density at the different stages can be seen in Figure 1.8. During the initial stage of sintering, vapor phase transport of atoms by surface diffusion takes place. The bulk of the sintering takes place during the intermediate stage. Therefore there is a great deal of attention paid to developing an understanding of how neck sizes increase with time in this stage. The neck size is controlled by grain boundary diffusion and lattice diffusion [27]. The optimization of sintering temperature and time is important during the final stage to avoid grain and pore growth. Both grain and pore growth are simultaneously possible from a kinetics point of view during the final stage [27].

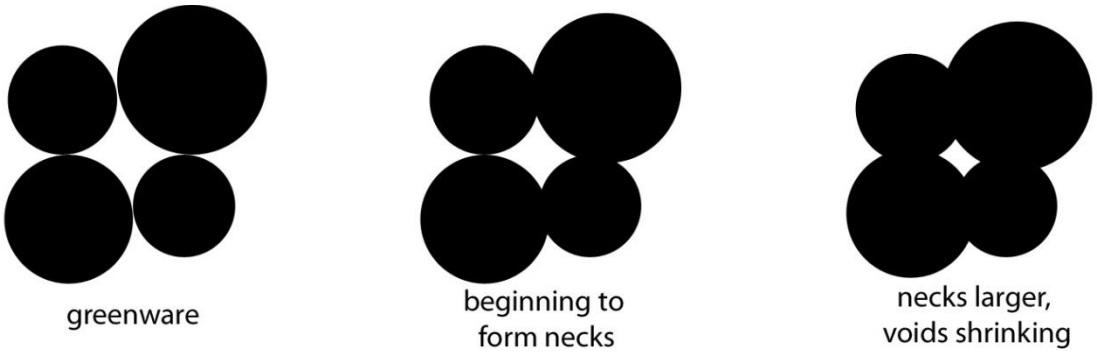

Figure 1.7: A diagram of the sintering process and the reduction of porosity and the increase in density. In addition, the trapping of internal porosity [28].

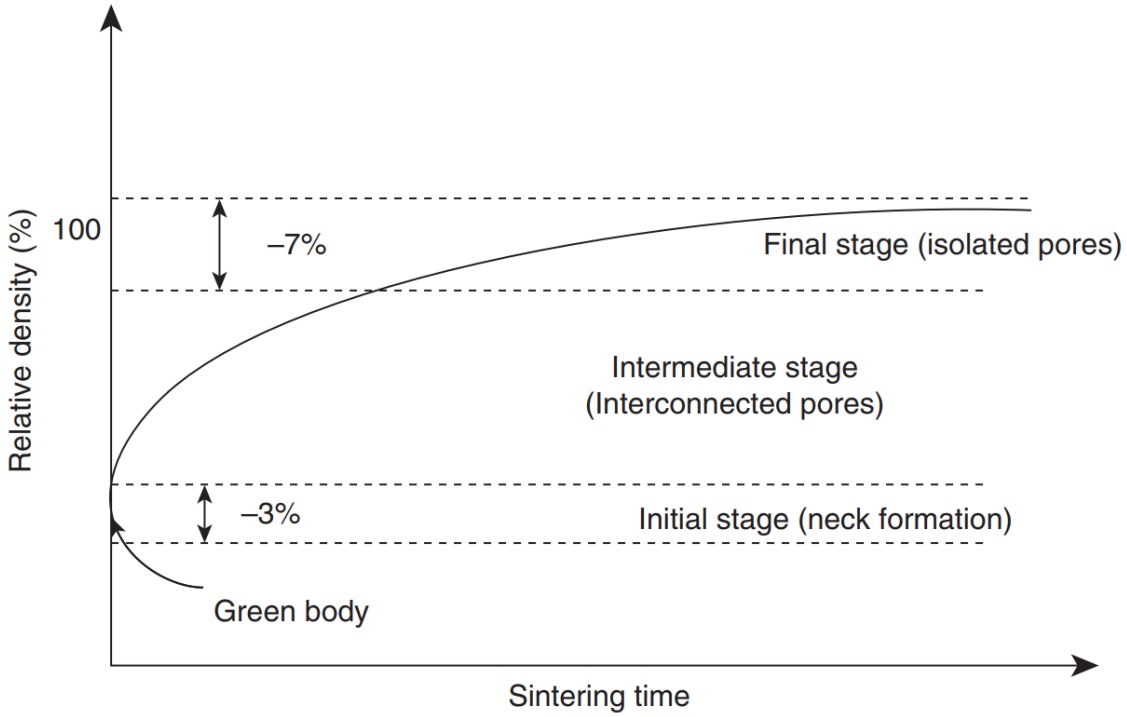

Figure 1.8: A generic plot showing the relative density during the different stages of sintering [27].

Spark Plasma Sintering

The spark plasma sintering (SPS) process utilizes pulsed high DC current along with uniaxial pressure to consolidate powders [29]. A schematic of the process is shown in Figure 1.9. In the SPS process the powders sinter under the simultaneous influence of a current and pressure [29]. SPS has been shown to have achieved cleaner grain boundaries [30], improved bonding [31], improved thermoelectric properties [32] and reduced impurity segregation at grain boundaries [30]. In a typical SPS system powders are placed in a die (usually graphite) and heating is applied by passing a current (usually pulsed direct current (DC)) through the die and the sample (if

conducting) while a pressure is applied to the powder [29]. The characteristics of SPS are a high heat rate, the application of pressure and the effect of current. The heat rate in SPS can be as high as 1000 ºC/min which is achieve by the heating process of the die and sample described previously. High heating rates have been shown to enhance densification by by-passing the non-densifying mechanism of surface diffusion and by creating an additional driving force due to large thermal gradients [33]. The goal with high heating rates is to suppress particle coarsening and enhance particle sintering. Powders that are sintered under an applied pressure achieve higher densification at the same temperature [33]. The major difference between convention hot-pressing sintering and SPS is the heating method of the sample and die. In hot-pressing the sample and die are usually heated by radiation from a furnace while in contrast the SPS method heats the sample and die by Joule heating from a current passing thorough them. While the pulsing DC current is providing the heating, it is also believed that the current has another role which is that of creating plasma. This plasma is believed to cause a cleansing effect on the surface of the particles leading to sintering enhancement [34-36]. This effect however is not of universal agreement and doubted by others [37-39]. In addition, the pulsed current has an influence on the mass transport during the sintering by the electron wind effect (electromigration) [40], by an increase in point defects [41] or decrease in the activation energy of the migration of the defects [42]. SPS has been used in the nuclear community to manufacture UO_2 composite materials to try increase the thermal conductivity of the pellet [43, 44], fuel for deep space mission [45], reduced sintering time for UO_2 [46] and produce accident tolerant UO_2 [47]. In this work 3 samples were manufactured by SPS to study the effect of grain size on the hardness and elastic modulus over temperature.

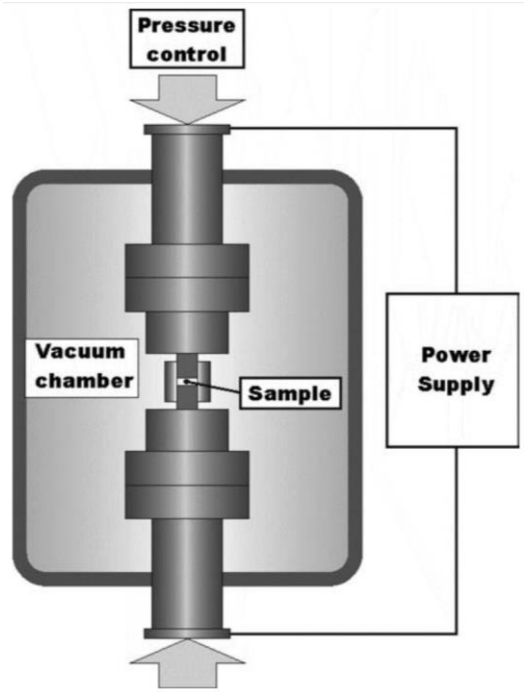

Figure 1.9: Schematic of SPS [29].

Crystal Structural and Physical Properties of UO_2

UO_2 has an isostructural with fluorite (CaF_2) where each U is surrounded by 8 O nearest neighbors in a cubic arrangement [48]. The melting temperature of UO_2 is 3270 K [49]. The density of UO_2 is 10.97 g/cm^3 and it has a lattice constant of a = 547.1 pm [50].

There are variety of different materials that could be used for fuel in nuclear reactors such UC, UN, U_2Si_3, U-10Mo, and other ceramic and metallic forms. However, UO_2 has been chosen as the fuel for commercial nuclear reactors for the following reasons: 1) high melting point, 2) chemical stability in water cooled reactors, 3) compatibility with cladding, 4) excellent irradiation stability and 5) ease of fabrication [51].

Operating Environment

There are many challenges with the extreme environment that nuclear fuel operates in during its lifetime in a reactor. The uranium atoms undergo fission to produce a large number of elements in the fuel and energy. The stereotypical bimodal fission mass production plot can be seen in Figure 1.10. The fission products can be grouped into 5 group depending on how they interact with the UO_2 fuel. The 5 groups are: 1) Elemental gases (Kr, Xe, Cs, Rb, Te), 2) metallic inclusion/precipitates (Mo and the noble metals), 3) Oxide precipitates or secondary oxides (Ba, Zr, and others), 4) dissolved in the fuel matrix (Mo, Zr, and rare earth elements), and 5) Alkali Metals (Cs) [51].

In addition UO_2 pellets operate at high temperature with center of the pellet being ~1200 ºC and the rim of the pellet being around ~500-800 ºC [51, 52]. The two sources of energy in the pellets are the local temperature and the energy that comes from fission events. Although the pellet rim has a lower temperature it has a high power generation from neutrons easily entering the fuel and causing fission events. In addition, due to the self-shielding effect of the U-238 isotope there is a depression in the neutron flux towards the center of the pellet. Furthermore, due to neutron capture in uranium, plutonium gets produced in the fuel periphery in greater amounts than the center of the pellet. The Pu-239 is also a fissle isotope which increases the power produced in the pellet periphery [52]. An image of the power and temperature distributions in a typical light water fuel pellet is shown in Figure 1.11. In addition, to increasing the power production in the periphery of the pellet the plutonium causes the “rim structure” or “high burnup structure” after a sufficient burn up in the pellet [52-55]. The large amount of damage and accumulation of defects in this region leads to the instability of the crystalline structure of the fuel, initiating a restructuring of the material. The high burnup structure region is characterized by appearance of densely packed very tiny (~1 micron) pores and nanocrystalline structure with grains on the order of 100 to 500 nm in size. Images of the high burn up structure can be seen in Figure 1.12.

Due to the fact that small scale mechanical testing samples small volumes different regions of the fuel pellet can be investigated using this method to see the changes from one region to another. This is unique for evaluating the mechanical properties of spent fuel as it difficult to measure and usually produce overall values that average of the different regions of the pellet. The ability to

evaluate these regions separately would allow for improved models that can account for the properties in the different regions.

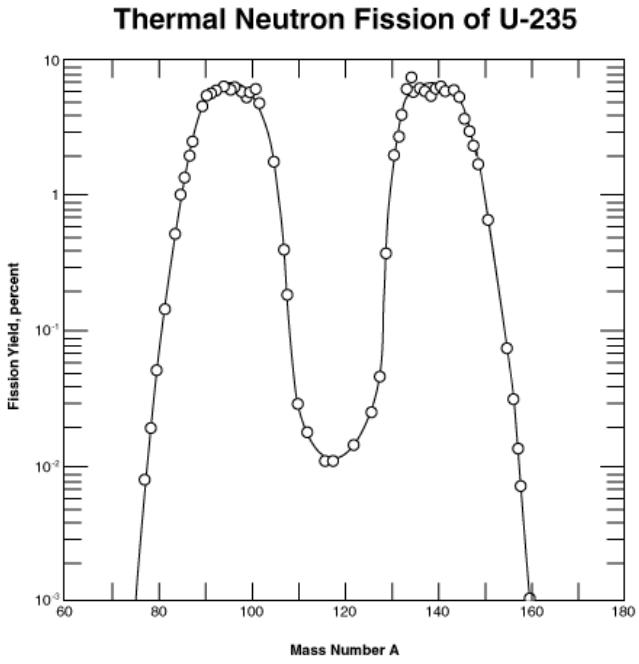

Figure 1.10: The double hump distribution for the thermal fission of U-235[56].

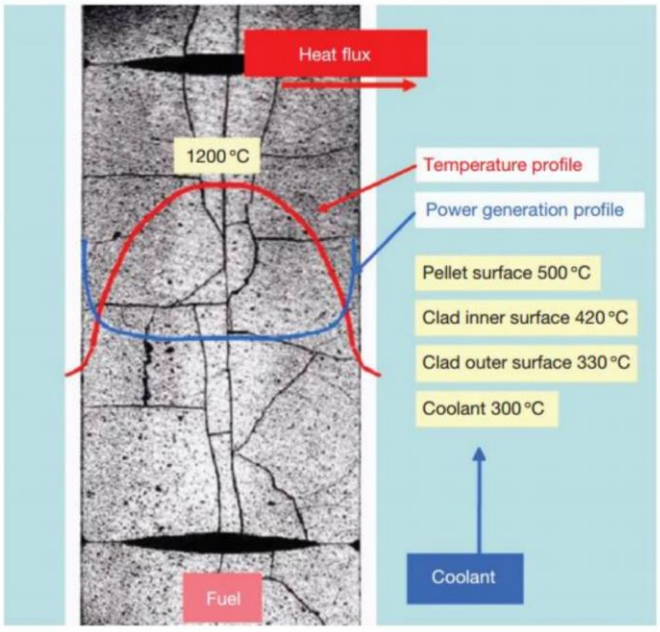

Figure 1.11: The power and temperature distributions in a typical light water fuel pellet [52].

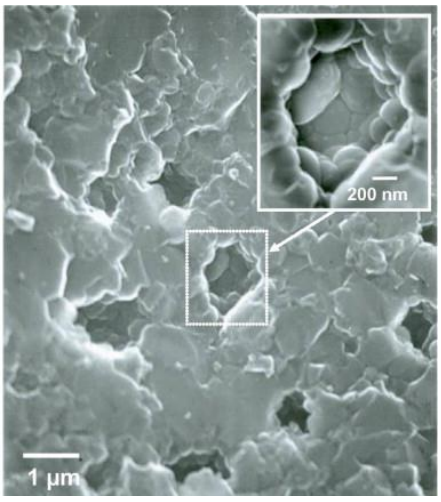

Figure 1.12: The high burnup structure in UO_2 in light water reactor [54].

Pellet Clad Interactions

During the lifetime of the UO_2 pellet in a nuclear reactor it comes into contact with the cladding material and experiences pellet clad mechanical interactions and pellet clad chemical interactions [51]. This happens from two different process taking place. The first process is the swelling of the fuel in the nuclear reactor. The swelling of the fuel happens from a variety of different process such as fission gas bubble formation in fuel, irradiation damage, and increase in temperature [51]. During the fission process, 1 uranium atom will split into 2 (possibly 3) atoms of different elements which will increase the volume of the fuel. In addition, some of the fission atoms are gaseous and will from bubbles in the material that will cause the fuel to swell. Just as in other materials the irradiation damage in the fuel from both heavy ions and neutrons will cause swelling in the fuel. Lastly, the temperature increase in the fuel during operation will increase the volume of the fuel from thermal expansion. The second process that cause the cladding to come into contact with the fuel is creep down of the cladding material onto the fuel [51,57]. The pressure of the coolant on the outside of the fuel rod is greater than the pressure inside the fuel rod during operation which will cause cladding to creep down onto the fuel. After creep down has taken place the resulting structure fuel clad structure is called bamboo structure in the nuclear fuels community because the cladding rod now resemble like stalks of bamboo. Images of the bamboo structure of the cladding can be seen in Figure 1.13. The contact of the cladding and the fuel causes the pellet clad mechanical interactions and pellet clad chemical interactions. The pellet clad chemical interaction can cause corrosion assisted stress cracking in the cladding. In addition, the elastic modulus anisotropy in UO_2 can also assist in the cracking of the clad which will be discussed in the next section.

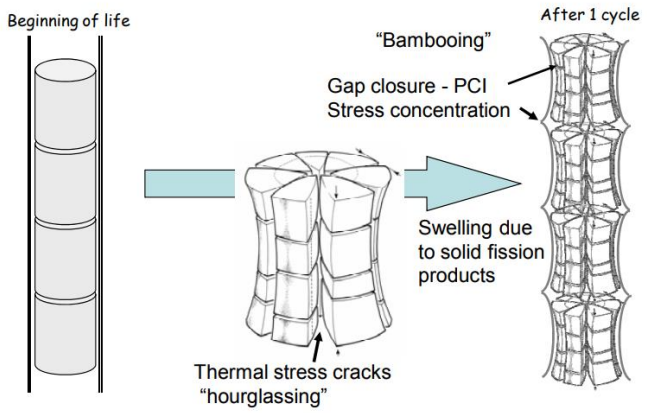

Figure 1.13: Bambooing of the cladding material in a light water reactor [57].

UO_2 Elastic Properties

UO_2 elastic properties are anisotropic which means that the physical and mechanical properties differ with orientation. The Zener ratio which is show as equation 1 can be used as a measure of anisotropy of elastic behavior for cubic crystals.

$$Z = \frac{2C_{44}}{C_{11}-C_{12}} \qquad \text{Eq. 1}$$

Where C11, C12, C44 are the independent single-crystal elastic constants of a cubic symmetry crystal. The elastic constants for UO_2 are shown in Table 1.1 from [58]. The elastic constant C11 is the modulus for axial compression. The elastic constant C12 is the modulus for dilation on compression and elastic constant C44 is the shear modulus. The elastic constants for a cubic crystals can reduced to these three independent elastic constants. When these elastic constants are used the Zener ratio it is calculated to be 0.441 which is smaller than unity illustrating that UO_2 has some elastic anisotropy. The theoretically values for the elastic modulus can be calculate using the following equation

$$\frac{1}{E} = s_{11} - 2\left(s_{11} - s_{12} - \frac{1}{2}s_{44}\right)(l_1^2 l_2^2 + l_2^2 l_3^2 + l_3^2 l_1^2) \qquad \text{Eq. 2}$$

Using the elastic constants in Table 1.1. The equation connects the reciprocal of the elastic modulus in the direction of the unit vector l_i with elastic compliance constants s_{ij}, for a cubic structure. The relative elastic modulus for UO_2 for different orientation is plotting in Figure 1.14. The maximum value of the elastic modulus for UO_2 is along the <100> with a value of 333.8 GPa while the minimum is along <111> with a value of 163.5 GPa. There is a need to measure the elastic properties of UO_2 at the subgrain level to assist with predictive modeling efforts of UO_2 because of this elastic anisotropy which has effects in the pellet clad mechanical interactions.

Table 1.1: The elastic constants of UO_2 [58].

Elastic Constant (10^{12} dyn/cm^2)	Value
C_{11}	3.893
C_{12}	1.187
C_{44}	0.597

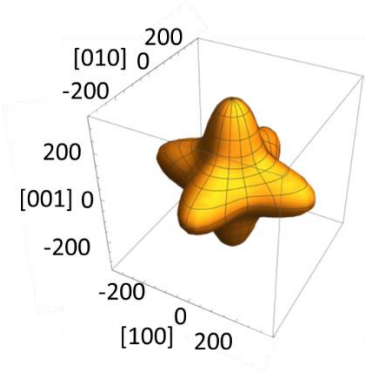

Figure 1.14: The elastic modulus value in different orientations of the crystal [59].

UO_2 Creep

The creep of UO_2 is also important property to understand for the PCMI during the lifetime of the fuel in the reactor. It is important because it is a mechanism to relieve stress when the pellet and clad contact each other. In addition, understanding the failure mechanisms of the fuel is important for modeling a reactivity initiated accident. An investigation into these mechanical properties would be beneficial because recent creep data on UO_2 suggests that the creep mechanism in UO_2 changes below temperatures of 1100 ºC from grain boundary sliding and dislocation creep to a peierls driven mechanism [60]. The peierls stress is the force need to move a dislocation within a plane of atoms in a unit cell. The dislocation motion in grains during these creep experiments cause sub-grain structures to form in the UO_2 grains. These sub-grain structures appear more readily during high stress and high strain creep tests and form new low angle grain boundaries in the UO_2 [60, 61].

Formation of Gas Bubbles in Materials

In nuclear fuel gas atoms from form two sources. The first being the alpha decay of the uranium atoms producing helium atoms in the UO_2. The second being the gas fission atoms that produced from the fissioning of the uranium atoms during energy production. Helium is insoluble in most

materials [62, 63] including UO_2 [64, 65]. The helium bubble formation is controlled by the change in Gibbs free energy. There is a decrease in the Gibbs free energy with the volumetric change from the formation of the bubbles. Then there is an increase in the Gibbs free because of the energy needed to create the free surfaces in the bubble. The volumetric contribution from the Gibbs free energy is to r^3 while the contribution from the free surface energy is to the r^2 so there will be a critical radius at which a bubble will be stable. Bubbles that are below this critical radius are unstable and can dissolve again. The bubbles with a radius above the critical size will be stable and continue growth. The bubbles in the material will continue to grow since the r^3 volumetric term dominates and the growth of the bubbles will continue to decrease the Gibbs free energy as showing Figure 1.15. The helium bubble nucleation theory decreased here is based on the theory of homogenous nucleation of the bubbles.

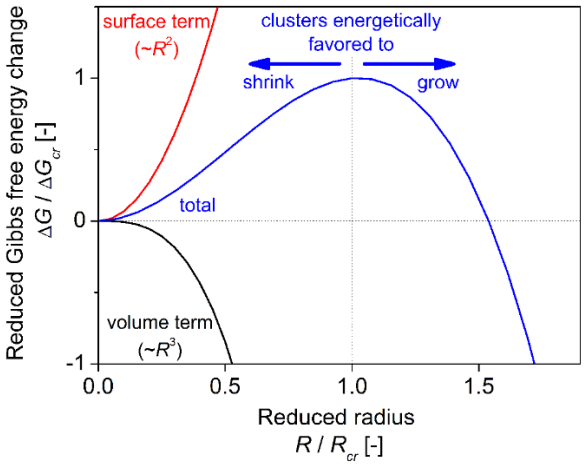

Figure 1.15: A plot showing the reduction in gibbs free energy for the volume term, surface term, and total. In addition, it illustrating that there is a critical radius at which the bubble is stable and will continue to grow [66].

Deformation Mechanisms of Ceramics

Ceramics are covalently or ionically bonded and need to remain charge neutral. These phenomenon make dislocation motion difficult because of the high strength of these bonds and charge distributions in the crystal structure [67]. The high stress required for dislocation motion is why most ceramic failures occur by the extension of flaws already present in the material. As such this why most ceramics fail in a brittle manner. This brittle behavior is determined by a competition between the creation/movement of dislocations and stress concentrations at microstructure defects. If the applied stress first reaches the yield stress for dislocation motion then plastic deformation will occur. If the local stress first reaches the critical fracture stress at a microstructural defect (pore, crack, or inclusion) in the material then brittle fracture will occur.

Plastic deformation in ceramics will not occur unless: 1) Electrostatic balance is retained 2) Structural geometry is not altered, 3) cation-anion ratio is maintained, and 4) five independent slip systems are present in the crystal structure [67]. UO_2 is a ceramic that has five slip systems at

higher temperature (> 500 ºC) and it would be expected to start to exhibit plasticity at these high temperatures [68].

Ceramics usually have a large lattice resistance and high theoretical strengths. Because of these high strengths and large lattice resistance, ceramics usually have low fracture toughness (amount of energy absorbed during fracture). Ceramics always have a reduced strength compared to their theoretical strength because they do contain flaws like pores or initial micro cracks. The sources of flaws can be the manufacturing process, thermal stress during cooling or thermal loading, corrosion at the surface and during mechanical loading. The flaws in the materials act as stress concentrators and reduce the mechanical properties of the material. The equation for the stress concentration at the tip of an elliptical crack in a non- ductile material is show in equation 3 with an example that shows how even small flaws in the material can have large consequences.

$$\frac{\sigma_m}{\sigma_s} = 2\left(\frac{c}{\rho}\right)^{\frac{1}{2}} \qquad \text{Eq. 3}$$

Where σ_m is the maximum stress at the crack tip, σ_s is applied stress, 2c is the crack length and ρ is the radius of the crack tip. An example stress concentration factor increase can be seen with the following example with Si_3N_4. If $\rho = a_0 \sim 2$ A = $2x10^{-8}$ m and c = 170 µm = $170x10^{-6}$. The stress concentration factor would be ~184 which demonstrates that even small flaws can cause large problems.

A benefit of small scale mechanical testing with ceramics is that a limited volume of materials is being test which can minimize the porosity in the sampled volume. In addition, due to small size and ability to pick the manufacturing location with the SEM/FIB the testing specimens can be manufactured to minimize porosity in the fracture surface and microcantilever. This allows the ability to measure the properties of the full dense material without defects in the testing volume.

1.3 Mechanical Property Testing Technique Background

Motivation for Small Scale Mechanical Testing

Small scale mechanical testing (SSMT) can offer many advantages in the nuclear materials community by reducing the amount of radioactive material need for testing, allowing the use of ions to simulate neutron damage in materials and the testing of individually materials features such as grain boundaries [69]. SSMT encompasses a variety of techniques such as nanoidentation, microcompression, microbending (cantilever and 3 pt) and microtensile testing. SSMT can reduce the amount of radioactive material need to perform mechanical testing which would reduce the dose to workers and could allow testing to be performed outside of hot cells and gloveboxes which would greatly reduce costs. In addition, since only a small amount of material is need for the testing, it would allow more tests to be performed on a sample which would increase the statics and information gathered form the sample. In addition, it would allow testing at different conditions (temperature, environment, strain rate) to be performed on the same sample. So for instances if a tensile bar was irradiated in nuclear reactor and tested it would only provide one data point where SSMT would allow the ability to perform the tensile testing over a temperature range

greatly increasing the information gained from that sample and therefore increase the data output on a limited amount of volume available. The use of SSMT would also be following in the principle of working with radioactive material and ALARA (As Low As Reasonably Achievable) with reducing the amount of radioactive material needed and the dose to the worker.

Neutron irradiations are costly and time consuming compared to ion beam irradiations. The nuclear materials community has been looking into ion beam irradiations as a way to simulate neutron irradiation in materials [70, 71]. However, a main challenge with ion beam irradiations is that the ions only penetrate a maximum of 10s of microns into the material without activating the sample. This prevents macro scale testing of the material after irradiation and requires the use of SSMT to evaluate the change in the mechanical proprieties because of irradiation damage. It has been observed that SSMT can observe the same changes in irradiated materials as observed at the macroscale with an increase in hardness and yield strength and a reduction in elongation [72]. SSMT is therefore, a valuable process for the evaluating different materials after irradiation. Since SSMT samples a small volume of material it allows the ability to measure individual features of sample such as grain boundaries and thin films on materials [73, 74].

Part of the motivation for exploring SSMT on heavy metal oxides (UO_2) is that it allows the ability to sample single crystal properties on real life materials and obtain a fundamental understanding of the materials without the influence of grain boundaries. Further it has to be highlighted that this type of work has never been done before and is a development process to hopefully have the ability to test neutron irradiation and spent fuel in the future. Part of this work will be to evaluate if the values collected on micron size samples can be related back to macro scale values of ceramics. In addition, it would part of this work is to evaluate the possibility of using SSMT on heavy metal (actinide) oxides. If this initial testing on fresh fuel is successful it would allow for the ability to apply these techniques to neutron irradiated fuel or spent fuel in the future to evaluate their mechanical properties for modeling efforts of fuel during its lifetime in a nuclear reactor as well as dry cast storage. The ability to greatly reduce the amount of material needed could remove the hot cells normally need for the testing of neutron irradiated fuel. In addition since a small volume of material is sampled during the test it would allow for the ability to measure the changes of the mechanical properties of fuel pellet along the radius of the fuel pellets due to its heterogeneous microstructure after it lifetime in a reactor [75, 76]. Nuclear fuel undergoes a variety of microstructural changes while in service in a reactor, which is described in more depth in the nuclear fuels section of this dissertation. SSMT would allow the ability to measure any difference in the mechanical properties because of the changes in the microstructure.

Nanoindentation

Nanoindentation is a mechanical testing technique to measure the hardness and elastic modulus of a material. Nanoindentation has gained in popularity in the past decades because of the simple sample preparation and automation of the instruments. All that is need for nanoindentation is a flat polished defect free surface which can have some difficulties [77] in obtaining but compared to other macro scale techniques such as tensile or compression testing this geometry is straight forward [78]. Nanoindentation instruments continuously measure the load and displacement data

of the indenter tip into the sample material and therefore are also referred to as instrumented indentation. The continuous measurement of the load and displacement with load cells and displacement sensor allows the mechanical properties to be directly extracted from the load–displacement curves without additional characterization of the residual impression [78, 79]. The procedure for extracting these mechanical properties from the load-displacement curves was developed by Oliver and Pharr [79]. The Oliver and Pharr method requires the calibration of both the tip area and frame compliance of the instrument to obtain accurate results. The standard tip used in nanoindentation is a Berkovich geometry. The function for the tip area is calculated by indenting into a known material (usually fused silica) at a variety of loads and then fitting this data so that the area corresponds to the correct value for the reduced modulus of the material. The reduced modulus is combination of indenter material modulus and sample material modulus. The elastic modulus of the sample being tested can be calculated from the reduced modulus with a producer being described later in this section. The produced for calculated the tip area is commonly known as the diamond area function for the indenter and it is a function that converts contact depth to contact area for the hardness calculation. The frame compliance calibration is measured by performing several high load indents into fused silica, tungsten, or steel to measure how much the nanoindentation instrument compress during an indent. The frame compliance is usually given in units of nm/mN. This is important because the slope of the unloading curve is how the reduced modulus is calculated which can be greatly affect by even small changes in the frame compliance of the instrument. Also calculating the frame compliance allows it to be removed from the reduced modulus calculation. In nanoindentation the reduced modulus is evaluated instead of the elastic modulus. The reduced modulus is a system measurement that is a combination of the elastic modulus of the material being tested and the elastic modulus of the material in the indenter tip. The reduced modulus is related to the elastic modulus on the sample by equation 4:

$$\frac{1}{E_r} = \frac{(1-\nu_i^2)}{E_i} + \frac{(1-\nu_s^2)}{E_s} \qquad \text{Eq. 4}$$

Where E_r is the measured reduced elastic modulus, ν_i is the Poisson's ratio for the indenter material, E_i is the elastic modulus for the indenter material, ν_s is the Poisson's ratio for the sample material, E_s is the elastic modulus for the sample material.

The hardness in nanoindentation is calculated with equation 5:

$$H = \frac{P_{max}}{A_r} \qquad \text{Eq. 5}$$

Where H is the hardness, P_{max} is the maximum load, and A_r is the area of the indent.

The reduced modulus is calculated with equation 6.

$$E_r = \frac{1}{\beta}\frac{\sqrt{\pi}}{2}\frac{S}{\sqrt{A_p(h_c)}} \qquad \text{Eq. 6}$$

Where E_r is the reduced modulus, β is geometrical constant, S is the stiffness of the contact or the slope of the curve upon unloading, $A_p(h_c)$ is the projected area of the indentation at the contact

depth h_c. In addition, Figure 1.16 shows a diagram of indent into a material illustrating physical what all of the different variable are.

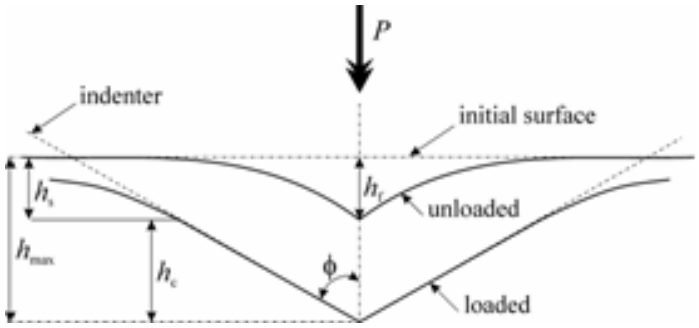

Figure 1.16: A diagram of indent into the material illustrating the contact depth, max depth and the deformation of the material [79].

High Temperature Nanoindentation

In addition to performing nanoindentation at room temperature, nanoindentation instruments now have the ability to perform nanoindentation at elevated temperature (up to 800 ºC) in reducing, inert or vacuum environments [80, 81]. The ability to test materials at temperature allows for the measuring of the mechanical properties at the material's operating temperature. A challenge with high temperature nanoindentation, however; is to have isothermal contact between the indenter tip and the sample material to prevent large thermal drifts. The thermocouples for both the indenter tip and sample are usually not located at the surface of either. The thermocouples therefore do not measure the temperature of the surface of the sample or tip. There will always be a thermal gradient between what the thermocouple controlling the heater is reading and what the sample surface temperature is in reality. The indenter tip and sample need to have an isothermal contact in order to prevent large thermal drifts that would negativity affect the indent and make the data analysis difficult or impossible. An example of what even a few degrees difference in temperature can cause on the loading-unloading curve can be seen in Figure 1.17. In this figure it can be observed that when the tip is warmer than the sample surface heat follows out of the tip and the tip shirks in size which causes a large positive thermal drift. When the tip is colder than the sample surface then heat follows into the tip which causes the tip to increase in size which induces a large negative thermal drift. When the sample and the tip make an isothermal contact the thermal drift is minimal and does not negativity impact the results of the indent. In addition, to the thermal drift there are other concerns about tip-sample interactions, tip-environmental interactions and sample-environmental interactions when performing high temperature indentation. Most nanoindentation tips are manufactured out of diamond due to its high hardness to prevent the blunting of the tip during use. However, diamond is made up of carbon atoms which start to react with air around 400-500 ºC and form CO and CO_2 which severally degrades the nanoindentation tip [82]. The oxidation of a diamond tip can be seen in Figure 1.18. This is the reason that most high temperature tips are manufactured out of cubic boron nitride (cBN) or sapphire. In addition to the tip oxidizing, the sample and the tip can have chemical interactions at elevated temperatures that would not be present at room temperature. An example of this is indenting ferrous materials with a diamond tip.

The carbon in the tip can diffuse into the ferrous material at elevated temperature causing the formation of carbides in the material that can affect the mechanical properties being measured. In addition the large diffusion of carbon out of the tip would cause the tip geometry to change rapidly affects the measurements. Lastly, there is sample-environmental interactions which is mostly oxidation of the sample surface or bulk. This oxidation of the sample fundamentally changes what material is being measured by the instrument due to the shallow depth of the indents.

In this work both an ex-situ inert/reducing environment nanoindenter and an in-situ vacuum nanoindenter were used. While both have the challenges discussed previously in this section the in-situ SEM vacuum nanoindenter has some additional challenges that will be discussed in the following paragraph. An issue with vacuum nanoindenters is mechanical noise which can be caused by the pumps need in order to achieve vacuum and the water cooling for the indenters. The mechanical vibration from the vacuum pumps can usually be mitigated by passive damping of the pumps and situating the pumps away from the instrument. If the indenter is design to be used with an SEM these issues many already be taken care of with isolation tables for the SEM. However, there is the additional challenge of the feed through wires causing mechanical vibrations in the instrument [77]. The thermal management of the nanoindenter will be more challenging in a vacuum system than an inert/reducing environmental system because there is no atmosphere for convection as a means of equilibrating temperature [77]. Also if the system is in a SEM there can be challenges with materials radiating infrared light and thermionic electrons at temperatures > 525 ^{o}C [77]. These thermion electrons can greatly reduce the image contrast because they would overwhelm the signal from the secondary electrons. In order to avoid this loss of contrast a larger spot sizes and high accelerating voltages is recommended. Lastly, in a SEM there will need to be a clear line of sight between the pole piece and the region of interest which will require careful design of experiments depending on the desired information to be obtained.

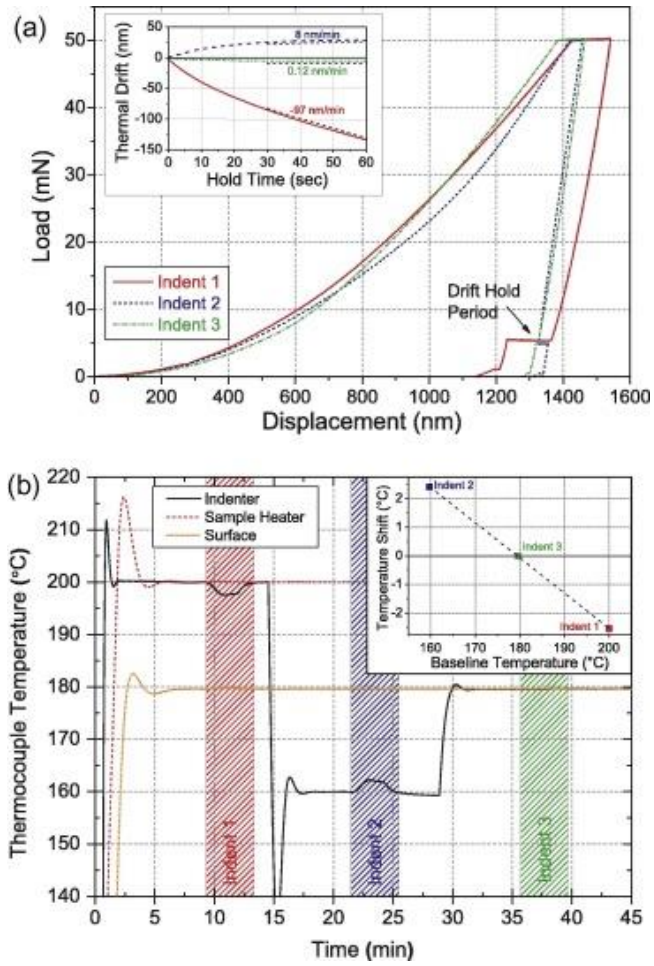

Figure 1.17: Indenter-sample temperature matching procedures using (A) thermal displacement drift and (B) indenter temperature shift magnitudes to determine the isothermal contact temperature [77].

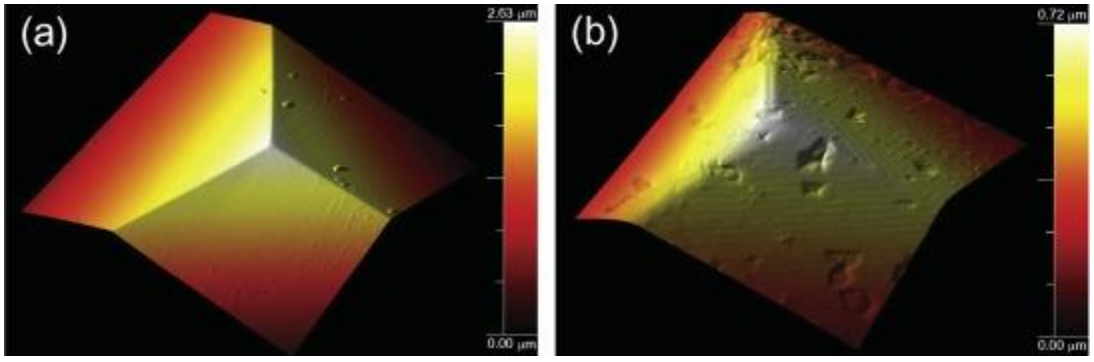

Figure 1.18: Indenter tips after usage in high temperature conditions: (a) AFM scan of a diamond Berkovich indenter undamaged after long term usage at temperatures < 400 °C [82], (b) AFM scan of a diamond Berkovich indenter after 90 min at 900 °C in commercial purity argon [82].

Nanoindentation Creep

Creep is the permanent/plastic deformation of a material at an applied stresses still below the yield stress of the material over an extended length of time [83]. In addition to the applied stress, the operation temperature of the material has an effect on the severity of the creep deformation and deformation rate in the material [83]. The rate of deformation is therefore, a function of the materials properties, exposure time, exposure temperature, and the applied load on the material. Creep deformation becomes a concern when a material is operated under high stress and/or high temperature for extended periods of time. Creep is a deformation mechanism and therefore may constitute a failure mode in a part of a piece of equipment. During the deformation the strain accumulates as a result of long-term stress, therefore creep is a "time-dependent" deformation mechanism. Creep is experimental measured for different alloys usually in a uniaxial fashion over extend periods of time. The creep is important in pellet clad mechanical interactions as described in the fuel section earlier as the creep of the UO_2 is a way of relieving the stress in the cladding when the pellet and clad come into contact.

Nanoindentation can be used to study the localized nanoindentation creep of the sample in a similar way to impression creep test [84]. In addition, nanoindentation creep is a useful tool for investigating the creep behavior of materials due to its fast testing process and limited sample size requirements [85]. However, there are several experimental and modeling challenges that pose obstacles to direct comparisons of indentation and uniaxial creep results and stress exponents [85, 86]. The literature however, has shown that the activation energy and stress exponents calculated from nanoindentation creep match well with uniaxial creep test results [85-89].

The stress exponent of the material is calculated from the slope of ln (strain rate) and ln (stress or hardness) curve. This comes from the power-law creep equation for conventional steady-state creep which shown below in equation 7.

$$\dot{\varepsilon} = A\sigma^n \qquad \text{Eq. 7}$$

Where n is the uniaxial stress exponent and A is the uniaxial pre-exponential term, $\dot{\varepsilon}$ is the steady state strain rate, and σ is the stress for a uniaxial creep test.

The strain rate for a nanoindentation creep experiment can be calculated with the following equation shown below in equation 8.

$$\dot{\varepsilon}_i = \left(\frac{1}{h}\right)\left(\frac{dh}{dt}\right) \qquad \text{Eq. 8}$$

Where h is the depth of the indent and dh/dt is the strain rate in the steady state section or linear portion of the nanoindentation creep curve. This is also called the second stage creep for the nanoindentation creep. At low stresses n is equal to one which indicates pure diffusion creep and at higher stresses n is greater than one indicating power law creep with mechanisms other than pure diffusion (e.g. grain boundary sliding, dislocation climb).

Nanoindentation Fracture Toughness

The fracture toughness of a material is the property that describes its ability to resist fracture or crack propagation. In linear-elastic fracture toughness measurements there is the stress intensity factor (K) which is when a thin crack in the material begins to grow. K is usually denoted with subscripts that indicate the type of fracture mode such as K_{Ic} and is usually denoted in units of MPa $m^{1/2}$. The subscript I in the notation denotes mode I cracking which is crack opening under normal tensile stress applied perpendicular to the crack. The modes of fracture that can also be denoted are mode II (shear) and mode III (tear). The c in the notation stands for critical. The fracture toughness of the UO_2 fuel is important for modeling efforts to understanding the evolution of the fuel during it life in a reactor. In addition the fracture thoughness of fuel is important to understand because it increase surfaces that radioactive fission gas can be released from.

Indentation fracture testing has gained in popularity due to the easy of sample preparation and testing [90-94]. The main indenters used for indentation fracture testing are pyramidal; however, spherical indenters can also be used [95]. In this research only a Berkoivch indenter was used which is a pyramidal indenter so the challenges and producers for pyramidal indentation fracture toughness will be discussed. The crack types for pyramidal indents usually includes one or several of the following types, (1) median crack, which resides below the indentation site, initiates at the elastic/plastic boundary, extends upward and downward and finally forms into a penny-like crack face; (2) radial crack, which resides near the sample surface and emanates radially from the indentation corner, (3) lateral crack which resides below the indentation site and extends nearly parallel to the sample surface. Examples of this crack types from a pyramidal indenter can be seen in Figure 1.19.

The sharp tips and edges of pyramidal indenters are prone to create easily measured radial cracks traces on the surface of the specimen. However, the singularity of the stress field under the indenter tip and edges makes it difficult to analytically solve the contact/fracture problems and has resulted in indentation fracture toughness methods being developed semi-empirically or empirically [95].

When the radial crack are well-developed (c >> a) (see Figure 1.20) a simplified relationship between the fracture toughness and crack length can be obtain [96].

$$\frac{K_{IC}\Phi}{HV\sqrt{a}}\left(\frac{1}{\Phi}\frac{HV}{E}\right)^{2/5} \propto \left(\frac{c}{a}\right)^{-3/2} \quad \text{Eq. 9}$$

Where c is the radial crack size, a is the half diagonal of the indent, constraint factor $\Phi \sim 3$, HV is the Vickers hardness and E is the elastic modulus of the specimen. With some math as shown in [49,50] the above equation becomes the following

$$K_{IC} = \delta\left(\frac{E}{H}\right)^{1/2}\frac{F_m}{c^{3/2}} \quad \text{Eq. 10}$$

Where F_m is the maximum indentation load and δ is a material-independent constant. For a Berkovich tip the value for δ is 0.016 [97, 98].

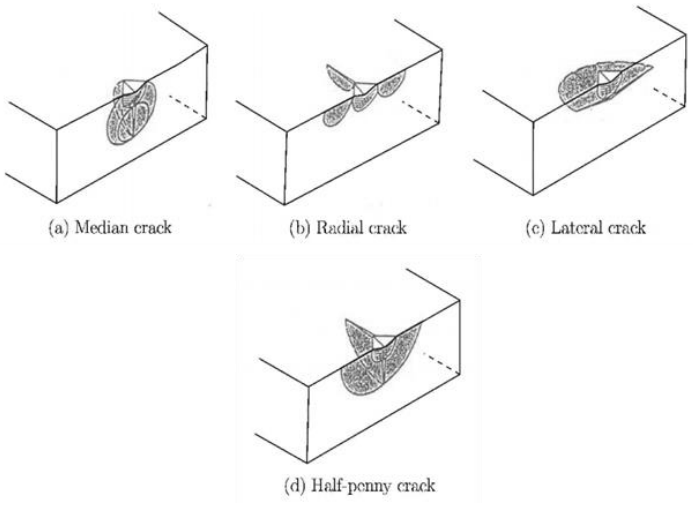

Figure 1.19: Different crack types under pyramidal indents [73].

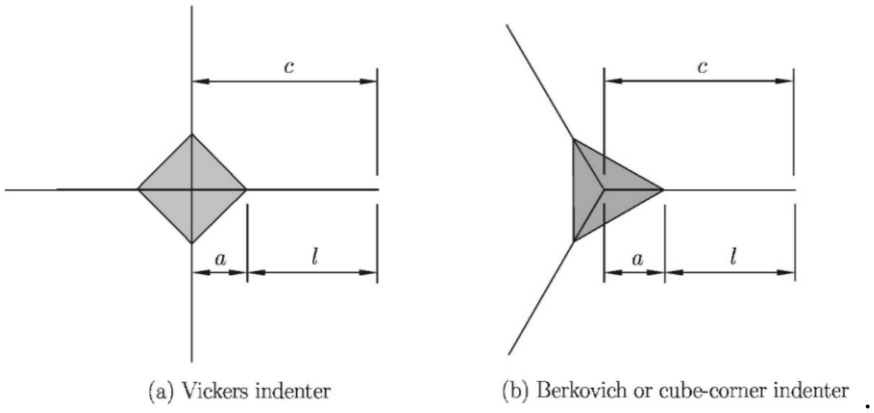

Figure 1.20: Representations of the different cracks from a Vickers and Berkovich indenter [95].

Microcantilevers

While nanoindentation described above provides very useful information about a materials performance at ambient and non-ambient temperature determining failure points is difficult when comparing to macroscopic data. Therefore uniaxial mechanical tests like microcompression or microtension were developed. Of course in inherent brittle materials like ceramics those are challenging tests and an analogy to the macroscopic three point ben test needed to be developed. Originally S.G. Roberts and Mia developed a cantilever type tests to quantify the mechanical properties of materials [99]. This technique is now widely deployed on ceramics, hard film coatings, tungsten, etc.. The technique is featured in Figure 1.21 below where a cartoon illustrating the geometry is shown.

The free body diagram of a cantilever beam with a load at the end is as follows:

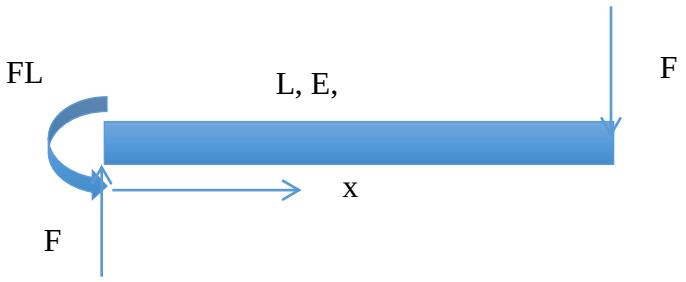

Figure 1.21: Cantilever mechanics cartoon as it applies on the equations 11-16 below.

There is a bending moment at x=0 equal to FL. Hence, the equation for the bending moment as a function of x, for x measured from the clamp, which is what will be used in these calculations, is:

M(x)=FL-Fx Eq. 11

Therefore, the differential equation for the deflection v(x) of the beam is

$$EIv''(x) = FL - Fx$$ Eq. 12

Integrating once one obtains:

$$EIv'(x) = FLx - \frac{Fx^2}{2} + C1$$ Eq. 13

The slope is zero at x=0, therefore:

If x=0 v'=0→C1=0 => $EIv'(x) = FLx - \frac{Fx^2}{2}$ Eq. 14

Integrating one more time:

$$EIv(x) = \frac{FLx^2}{2} - \frac{Fx^3}{6} + C2$$ Eq. 15

The deflection is zero at x=0, therefore

If x=0 v=0, => C2=0

$$EIv(x) = \frac{FLx^2}{2} - \frac{Fx^3}{6}$$ Eq. 16

A well-known result is that the deflection of a cantilever beam at the point of application of the load is $FL^3/(3EI)$. This is what one obtains from evaluating the equation given above at x=L.

In addition, the ratio of the length to height of the microcantilever needs to be a minimum of 5-6 in order to reduce the effects of the substrate to insignificant amounts [99]. If the microcantilevers are too short then the effects of the substrate material reduce the calculated elastic modulus value for the microcantilever. The need to maintain this ratio is because the linear elastic fracture mechanics assumes a clamped end and slender beams. If the microcantilevers become too short the beams move farther away from these assumptions and there is a large contribution from the substrate which affects the calculated value of the cantilever.

1.4 Material Characterization Technique Background

Electron Backscatter Diffraction

Electron backscatter diffraction (EBSD) is a powerful technique that allows for the measuring of crystallographic orientation, misorientations, texture, grain size and boundary types, and phases on the marco to nanometer scale in crystalline materials. In this work EBSD was used on the different samples of UO_2 to measure the orientations of the grains for use in evaluating the results of the microcantilevers. The technique involves arranging a flat, highly polished sample at a shallow angle to an incident electron beam (usually a SEM). When this incident electron beam interacts with the crystal lattice of the material low energy loss backscattered electrons are channeled and are subject to path differences that lead to constructive and destructive interference [100]. A phosphor screen is placed close to the sample to detect the diffracted electrons which make light when interacting with the screen that that is recoded by a light sensitive detector. The diffraction pattern that is formed is called a Kikuchi pattern which is made of Kikuchi lines which was first observed by Shoji Nishikawa and Seishi Kikuchi [100]. The widths of these Kikuchi lines are dictated by Bragg's law and specimen-to-phosphor screen distances. Computer software can then index these Kikuchi patterns to evaluate the orientation of the crystal and phase of the material. A diagram for the experimental set up can be seen in Figure 1.22A. In Figure 1.22B an example of the electron interaction and resulting Kikuchi pattern is shown.

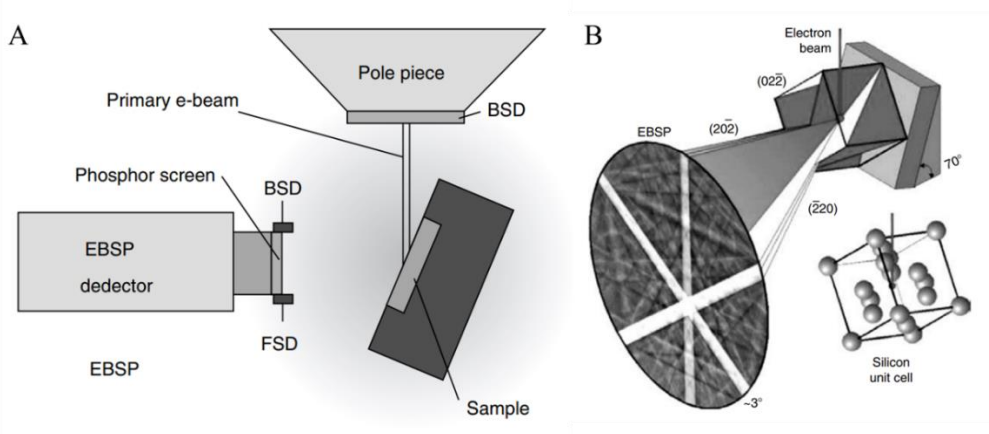

Figure 1.22: A) A schematic of EBSD measurements being performed [100].B) A cartoon of crystal producing a kikuchi pattern that is being index to evaluate the orientation of the crystal [100].

Transmission Electron Microscopy

All of the transmission electron microscopy (TEM) work was completed on a JEOL 3010 LaB_6 TEM operated at 300 kV at the National Center for Electron Microscopy (NCEM). The TEM was used to watch the in-situ microcantilever bending experiments. These experiments were used to evaluate dislocation motion in the microcantilever. In addition, the TEM was used to evaluate the helium bubble formation from implanted helium in UO_2.

The dislocation is not directly observed in the TEM, it is the strain field around the dislocation. The contrast of dislocation depends on several parameters: 1) The diffraction conditions. Is the Bragg condition fulfilled for the reciprocal lattices vectors g, 2) The excitation error, 3) the magnitude of the scalar product between the lattice vector g and the Burgers vector, 4) the imaging mode (bright field or dark field). The elastic scatter of electrons in the material cause a diffraction pattern to from.

When the sample is in focus in a TEM the helium bubbles will be invisible. It is only when the TEM is under focused or over focused do the Fresnel fringes appear around the bubbles allowing us to observe them. Fresnel fringes come from the phase interference of the electron waves in the TEM. This technique will be used to observe the helium bubbles implanted into the UO_2 for the in-situ mechanical testing. In this work the effect of helium bubbles on the deformation of the UO_2 was evaluated because of the formation of fission gas bubbles during operation.

Scanning Electron Microscopy

A scanning electron microscopy (SEM) was used in this research to image the samples and perform the EBSD. The instrument was FEI Quanta 3D FEG dual beam (SEM/FIB) located at the University of California, Berkeley. A field emission gun (FEG) SEM uses an extremely sharp tungsten tip to produce the electron beam in the instrument. FEG SEM is use because FEG are capable of producing high electron brightness and small spot sizes even at low accelerating potentials [101]. The images taken in the SEM used the secondary electrons.

Focused Ion Beam Microscopy

A focused ion beam (FIB) was used in this work to mill the microcantilevers and TEM foils which is explained in the experimental section. A FIB uses a liquid metal ion source (LMIS) with gallium as the liquid metal [102]. In a gallium LMIS a tungsten needle is places in contact with the gallium which is heated and wets the tungsten needle. The liquid gallium flows to the tip of the needle where a high electric field causes ionization and field emission of the gallium atoms [102]. The gallium atoms are then used to finely sputter the material which allows for the milling of different geometry into a material.

Helium Ion Microscopy

A helium ion microscope was used to implant the TEM foils with helium to form the bubbles to evaluate the effect of the deformation on the UO_2. The helium ion microscope used a Zeiss ORION nanofab instrument. The implantation parameters will be explained in the experimental section. A

helium ion microscope uses a gas field ionization source to produce the beam of helium ions that is used to image and implant into the sample [103-105].

Chapter 2

Experimental

2.1 Grain Growth Experiments

The polycrystalline samples for this work were provided by Los Alamos National Laboratory (LANL). The specimens first went to our collaborators at Arizona State University (ASU) where heat treatments on the specimens to increase in the grain size were performed. The average grain size of a UO_2 pellet is 5-10 μm [51]. This grain size is smaller than the initial chosen size for the microcantilevers which was chosen to be between 15-30 μm long. ASU preformed heat treatments on the specimens in order to grow the grains larger than 30 μm to allow for entire micorcantilevers to be manufactured in a single grain. ASU attempted 4 heat treatments of the sample in order to increase the grain size. The first heat treatment was performed at a sample temperature of 1130 ºC at a pO_2 (partial oxygen pressure) of approximately $7x10^{-7}$ atm in a vertical furnace. The heat treatment was conducted for 5 hours. This initial heat treatment instead of growing the grains actually decreased the number of large grains in the specimen and actually homogenized the grain size in the specimen. The second heat treatment was performed at sample temperature of 1200 ºC with a pO_2 of approximately 10^{-4} atm. This second heat treatment lasted 48 hours. The results of this second heat treatment were again not satisfactory as the average grain size in the sample decreased. The result of this heat treatment indicated that the conditions used were too close to the boundary the UO_{2+x} one-phase region and the UO_{2+x}/U_3O_8 two-phase region as shown in Figure 2.1 [35]. The third heat treatment was performed at 1215 ºC with a mixture of ultra-high purity argon (Ar) and Ar-100 ppm O_2 lasting for a total of 113 hours. This third heat treatment did produce an increase in grain size from 10 μm to 13 μm [35]; however, this is still not sufficiently large to manufacture a single cantilever in a single grain. The fourth heat treatment was performed at 1460 ºC with a mixture of Ar-5% H_2 and Ar-100 ppm O_2 for 76 hours. The average grain size increase from 13 μm to 25 μm during this heat treatment which delivered sufficiently large grains. In addition, analysis showed that the specimen had a relative density of 95 % [35].

After the initial testing with the polycrystalline samples it was chosen to proceed with a single crystal specimen of UO_2 in order to negate any grain boundary or otherwise defect based complications. LANL provided a (111) single crystal flake for this work. Our collaborators polished the specimen to a mirror finish and so that the (111) orientation was orthogonal to the polished surface. The single crystal had a lower porosity and allowed the ability to manufacture microcantilevers on a corner of the sample for in-situ SEM testing at both room and elevated temperature.

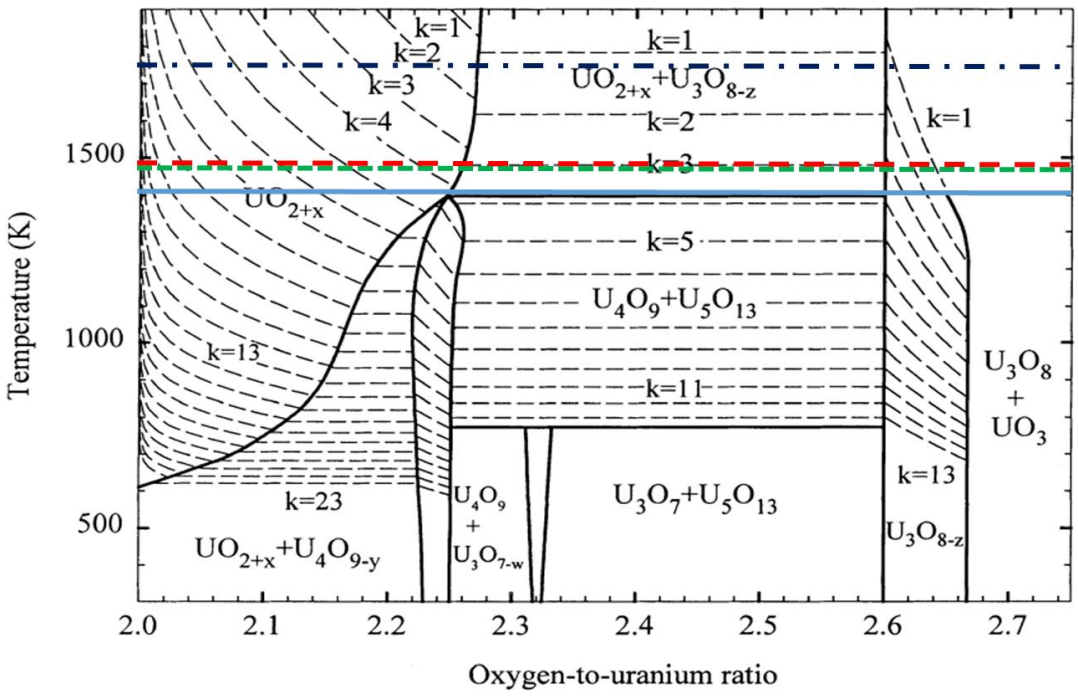

Figure 2.1: The phase diagram of the U-O system with oxygen pressure isobars superimposed. The isobars are indicated by the index k in $p = 10^{-k}$ where p is in atm [106]. In the figure the solid blue line is the first heat treatment, the green small dashed line is the second heat treatment, the red larger dashed line is the third heat treatment and the dark blue alternating dashed line is the fourth heat treatment.

2.2 Polycrystalline MicroCantilever Fabrication

After the completion of the heat treatments and polishing by the ASU collaborators the polycrystalline specimen was shipped to University of California, Berkeley (UCB). At UCB the samples were mounted onto standard scanning electron microscopy stubs with silver paste. After mounting, the samples were loaded into a FEI Quanta 3D FEG Dual Beam (SEM/FIB) instrument to before electron backscatter diffraction (EBSD) and manufacture the microcantilevers. The EBSD was use to evaluate the orthogonal orientation of the grains the cantilevers were being manufactured in and to evaluate the orientation along the length of microcantilever as that is direction that it was loaded in. The microcantilevers were manufactured with a focused ion beam (FIB) utilizing the following process. Firstly, 15-30 nA beam current with the regular cross section pattern was used to mill three trenches into the sample. The regular cross section pattern was used because it greatly reduces the milling time by milling a staircase-shaped pattern which reduces the amount of material that needs to be milled. The 3 trenches formed a U-shaped trench that defined the rough geometry of the beam. The beam was next cleaned with 1-3 nA current which was used to accurately define the beam geometry and size. Next the beam was tilted 45° along the length axis and the beam was undercut from both sides to free it form the substrate material. This produced the "*upside down house*" shape as seen in [107]. After the microcantilever was free from the substrate material it was cleaned again with a current of 0.5-1 nA to remove the re-deposition

form all of the sides of the microcantilever. A diagram of the milling process can be seen in Figure 2.2. The manufacturing of the UO_2 microcantilevers at different stages can be seen in Figure 2.3. The "*upside down house*" shape microcantilevers had the advantage of being able to be placed anywhere in the polycrystalline material which allowed use to place them in the larger grains in the material.

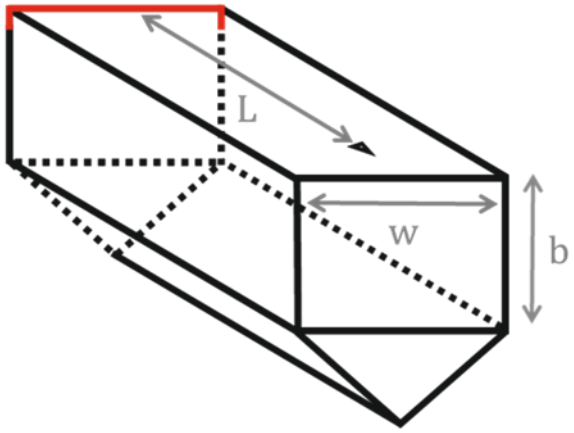

Figure 2.2: A diagram of the geometry of the microcantilever used for the ex-situ testing in the MicroMaterials indenter at both room and elevated temperature.

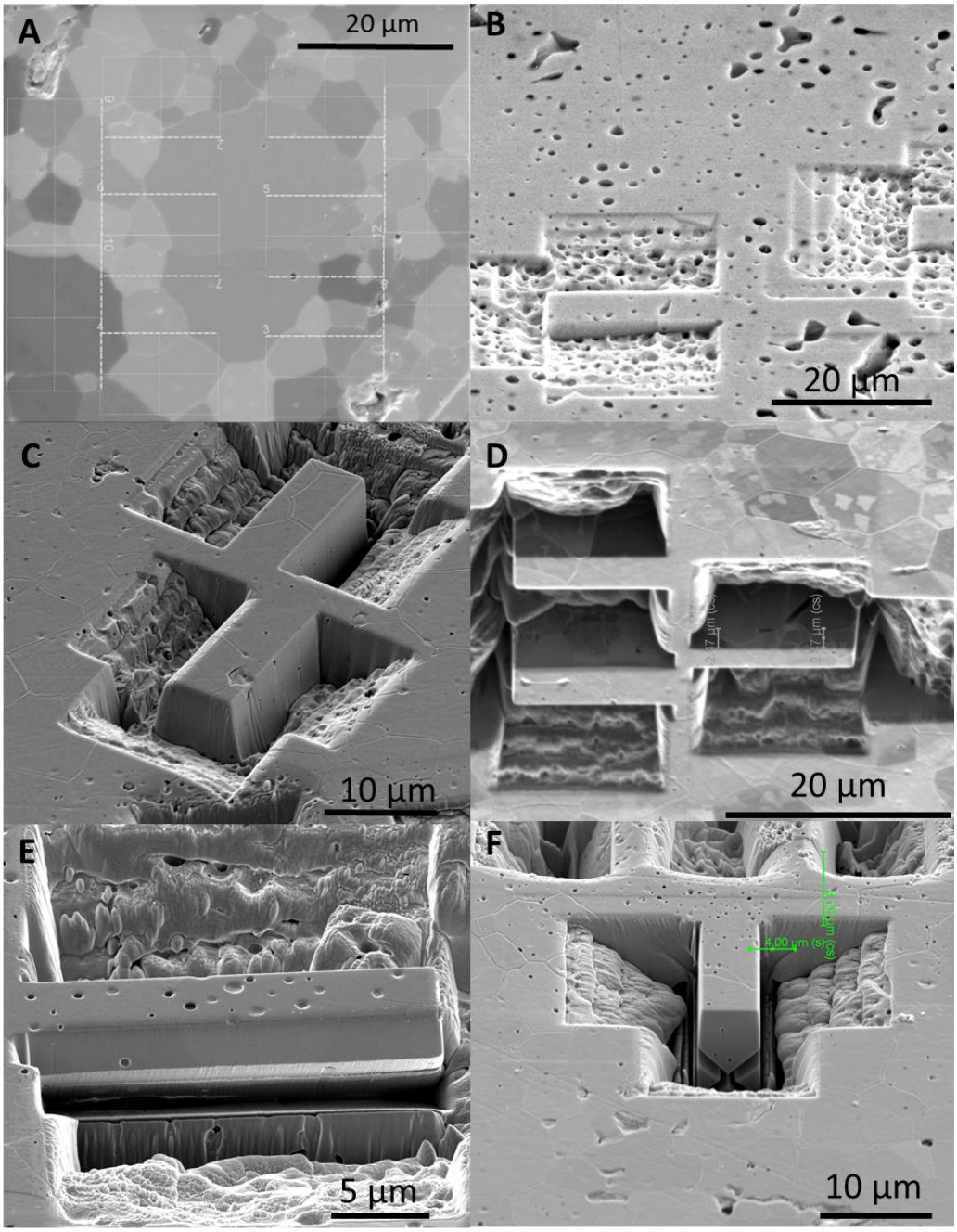

Figure 2.3: A) A FIB image of the grains of UO_2. The patterns that will define the shape of the microcantilever can be seen in the image. B) Microcantilevers starting to be trenched in UO_2. C) The close microcantilever after trenching with the curved egdes due to overshoot on the FIB. The far microcantilever has been cleaned and is ready for under cutting to free the microcantilever from the substrate. D) Looking at microcantilever long its length at 7 º tilt in the FIB. The measurements for the placement of the undercut can be seen in the image. E) An image of the length of the microcantilever undercut and freed from the substrate material. F) An image of a finished microcantilever ready for testing.

2.3 In-situ Single Crystal Microcanitlever Fabrication

The single crystal sample allowed the manufacturing of microcantilevers on the corner of the sample. The ability to manufacture the microcantilevers on the corner of the sample allows for in-situ SEM mechanical testing. The manufacturing of the microcantilevers on the corner of the sample also allows the ability of a rectangular geometry as compared to the "*upside down house*" geometry used in the polycrystalline samples. This rectangular geometry makes the calculations easier but has the disadvantage that the samples have to be manufactured on the corner of a sample. The manufacturing process for the in-situ micorcanitlevers is as follows: The single crystal of UO_2 was first mounted on appropriate sample mount. The two picoindenters used for the in-situ testing had different ways of mounting the sample which is explained in the in-situ microcantilever testing portion of this chapter. For the room temperature testing, the sample was mounted on a standard SEM stub and for the elevated temperature testing the sample was mount on a thin steel piece which then was mounted onto a SEM stub using carbon tape and a minimal amount of silver paste. When the samples were load into the SEM/FIB dual beam instrument they were loaded on a 45º mount with the corner that was intended for the cantilevers facing up. Since the instrument used in this research is a FEI Quanta system the angle the stage has to be tilted to be perpendicular to the FIB beam is 52º. The sample is already on a 45º mount so the stage would only have to be tilted an additional 7º to have the surface of the sample perpendicular to the FIB beam. In this configuration the top and one side of the sample is available to be mill perpendicular. The ability to mill perpendicular into the side of the top corner allows to undercut the microcantilever to have the rectangular geometry. The two sides are accessible my rotating the stage 180º. An illustration of this can be seen in Figure 2.4. The rough milling was performed with 15 nA. In the rough milling stage the geometry, length of the cantilever and orientation are defined. In this case the regular cross section pattern was only used on two sides (the side farthest from the edge of the sample and the front of the microcantilever). The side closest to the edge used a rectangle pattern to insure that the sides of the microcantilever were parallel. After the rough cutting was complete the microcantilever was cleaned up with a current of 3 nA. After this step the sample was rotated 180º and 3 nA was used to undercut the microcantilever and free it from the substrate material. After this all of the sides and the undercut were cleaned with a 0.5-1 nA current to remove any reposition and make the cantilever have precise size and dimensions. The microcantilever with the square geometry which manufactured so that their length was at least 5 times greater than their height ($\frac{L}{H} \geq 5$). When this criteria is meet the effects of the substrate material are negligibly and the assumptions of the slender beam equation are more closely meet. Examples of these rectangular microcantilevers can be seen in figure 2.5.

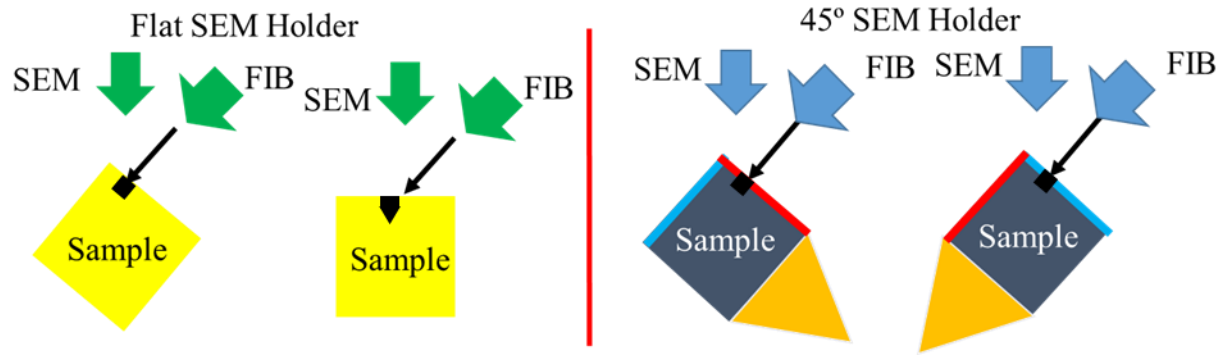

Figure 2.4: An illustration of how mounting the sample on a 45 º mount allows for milling into two different faces of the sample at an edge as compared with a flat SEM mount which only allows milling perpendicular to one face. The black shapes in the samples shows the mills for the microcantilever geometry that happens at each orientation.

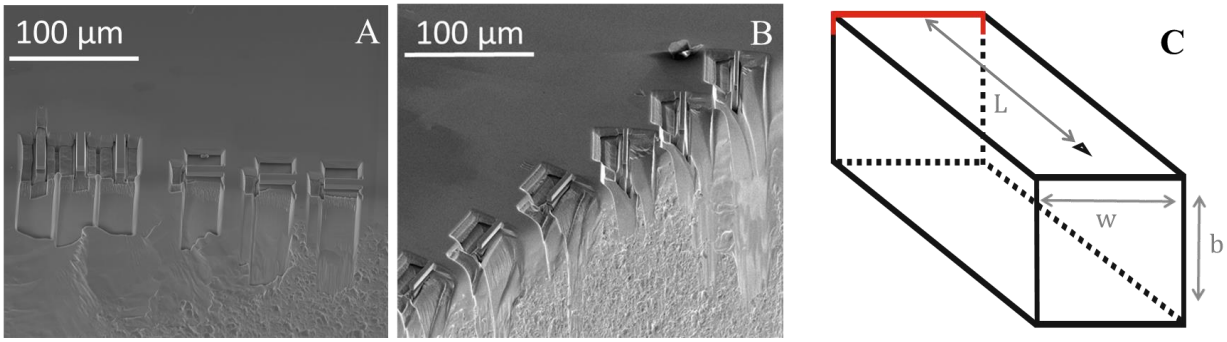

Figure 2.5: Image of microcantilevers manufactured on the corner of the sample to have a rectangular geometry. A) One set of microcantilever mill parallel with the edge and second set milled perpendicular to the edge. B) Two sets of microcantilevers milled at different orientations to the edge of the sample. C) A cartoon of the rectangular geometry showing the different dimensions used in the calculations.

2.4 Ex-situ and In-situ Microcantilever Testing

The first testing of the polycrystalline microcantilevers was performed ex-situ on a MicroMaterials Platform 3 nanoindenter. The instrument is located at the UCB and has both a Plexiglas chamber for environmental control and piezo stage for imaging the topography of the sample surface. An image of the instrument can be seen in Figure 2.6. In addition, the instrument can independently heat the tip and sample stage up to 750 ºC to allow isothermal contact between the tip and sample to minimize the thermal drift during testing. This ability allows for the testing of the microcantilevers at temperature to evaluate if any ductility in the UO_2 is present during testing. The piezo stage was used to accurately place the indenter tip into the microcantilever during testing. In addition, the nanoindenter has an attached optical microscope for accurate placement of the indenter tip as well.

The testing producer for the microcantilevers was as follows. The calibrations on the MicroMaterials indenter are completed. This includes the cross hair calibration and the sample stage calibration. These calibrations encode where the indenter tip is compared to the cross hairs on the optically microscope. These calibrations are important because they allow the accurate placement of the of indenter tip over the microcantilever for scanning and testing. Next, the sample is load into the indenter and the microcantilevers for testing are located in the optical microscope and moved into focus. Then a topography scan is performed using the piezo stage. This allows for precise placement of the indenter tip on the microcantilever using the scan. This is because the scan can be used for placing indents on the material. An example of a scan with loading location being selected can be seen in Figure 2.7. After, a displacement controlled indent is programed into the instrument with a loading rate of 10 nm/s. The displacement control feature is used to cause a plateau in load to occur when the microcantilever fractures. This plateau occurs because in displacement control the indenter is running a feedback loop to keep the indenter moving 10 nm/s into the material. The indenter runs this feedback loop because its hardware is load controlled but adjusting the load 1000s of times a second to maintain a constant displacement rate. When the mircocantilever fractures the indenter would jump several 100s of nm up to few micron in depth and the indenter would not have to increase the load to reach it depth targets in the feedback loop. An example of load versus displacement curve can be seen in figure 2.8. Before and after fracturing a UO_2 microcantilever an optical image is taken with the attached microscope.

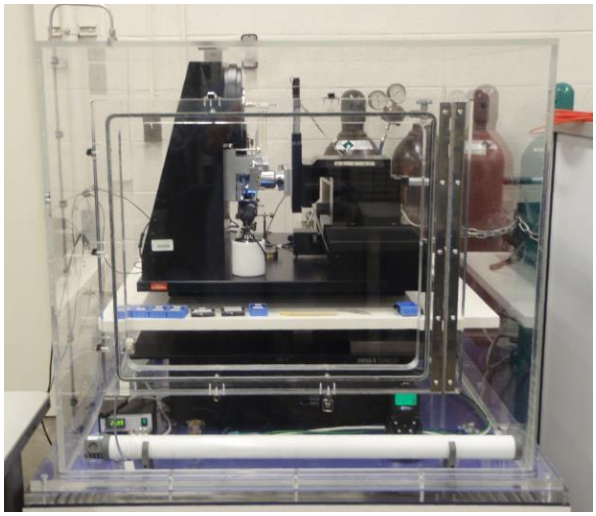

Figure 2.6: An image of the MicroMaterials nanotest system. In the image the Plexiglas™ environmental chamber surrounding the indenter can be observed.

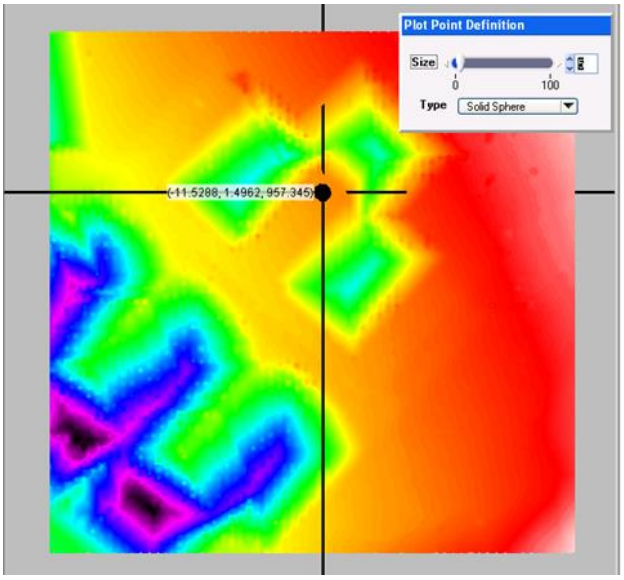

Figure 2.7: A scan of a microcantilever with the ex-situ MicroMaterails indenter. The black dot at the end of the microcantilever is the location being selected for the loading of the microcantilever.

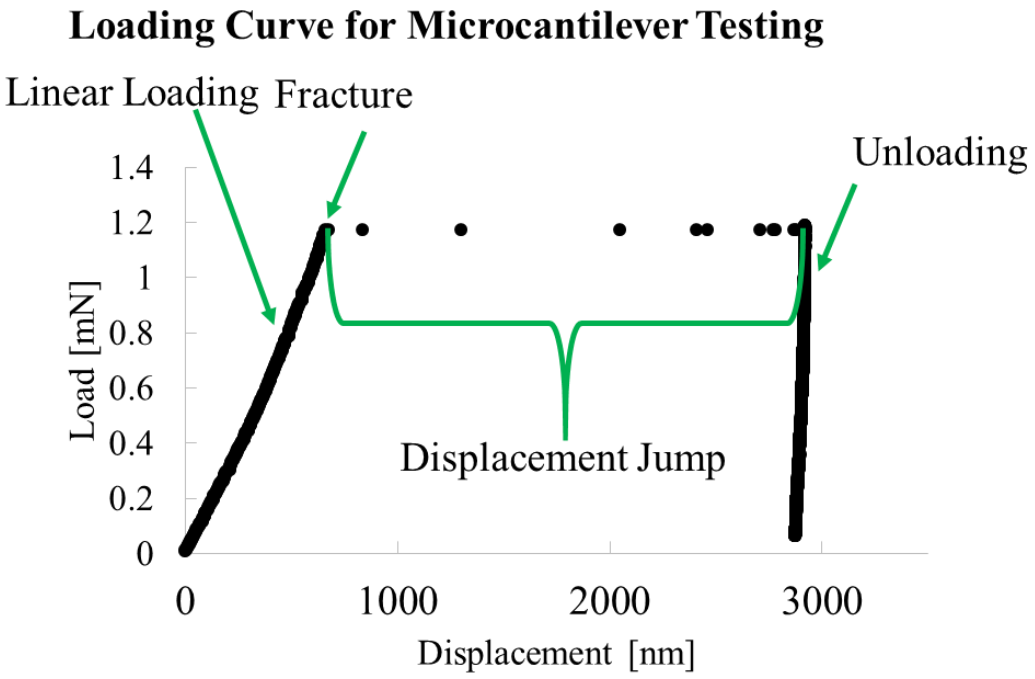

Figure 2.8: An example of a load versus displacement curve from the MicroMaterials indenter for ex-situ microcantilever testing. The curve is label to show the different step of the testing process.

2.5 High Temperature Testing using the MicroMaterials Indenter

The high temperature testing procedure is similar to the room temperature testing procedure; however, with addition mounting, temperature thermalization producers and environmental control. The UO_2 sample with the microcantilever is first mounted to hot stage for the indenter using Omega 700 cement. The cement needs 24 hours at room temperature to cure before testing and heating. After the cement has cured the initial testing procedure of locating the microcantilevers is the as the room temperature testing procedure. Everything is the same until the scanning of the microcantilever with the piezo stage. Before the scanning with the piezo stage both the sample and tip were heated to the desired testing temperature. The heating process for the specimens is as follows. The locations of the microcantilevers to be tested at temperature are found with the optical microscope at room temperature. The relative locations between the microcantilevers are recorded in a laboratory log book for later referencing. These locations are recorded because once the sample is heated up to temperature, the optical microscope cannot be used during the testing as it might melt or distort the glass in lens. After, the locations have been recorded, the first microcantilever for testing was placed in front of the tip approximately 200-300 µm away from the tip to allow for the thermal expansion of the sample and tip. At this point the Plexiglas environmental chamber is purged with Ultra High Purity (UHP) Ar gas to displace the air out of the chamber. The purging with UHP Ar gas was done overnight at 10 liters/min and would reduce the oxygen content in the chamber to on the order 10^{-4} oxygen partial pressure. This is too high of an oxygen content to prevent the oxidation of UO_2 to U_3O_8 at the testing temperatures. In order to have a reducing environment in the chamber an Ar + 5%H_2 was used. The reducing

environment is needed because the UO_2 will further oxidize to U_3O_8 at these temperatures in air or high purity Ar. The oxygen concentration in the chamber was measured using a modified Bosch™ oxygen sensor. A stand was placed inside of the Plexiglas chamber to hold the oxygen sensor at the same height as the sample in the chamber. The oxygen sensor was used to evaluate the oxygen as the high purity Ar was feed into the chamber. This was to confirm that the high purity Ar was displacing the air in the chamber. Once the Ar + 5% H_2 was feed into the chamber the oxygen sensor no longer worked. It is believed the oxygen stopped functioning because of the H_2 in the chamber. The gases were switched at the start of the heating process for the tip and sample of UO_2. After the switching of the gases, the desired testing temperature for the tip and sample where entered into the MicroMaterials software. The tip and sample were both heated at 1.6 ºC/min to the desired temperature in the Ar + 5%H_2 environment. At this heating rate it takes approximately 1 hour for every 100 ºC of heating and the system required 1 additional hour for thermal stabilization. After the thermal stabilization period was complete the sample is moved into contact with the tip at an extremely low load and then moved a slight distance (20-30 µm) away from the UO_2 sample surface where a test indenter could be performed to evaluate the difference in temperature between the tip surface and the sample surface. The evaluation of the difference in the temperature between the tip and sample is performed by examining the thermal drift of the test indent. The temperature of the tip and the sample were deemed the same when the thermal drift of the indent was less than ±0.1 nm/s. The thermal drift of an indent is calculated by holding at 10 % of the max load of the indent for 60 seconds. Only the last 60% of the data collected during this hold period is used to calculate the drift. The reason for using only the last 60% is to remove any artifacts from elastic or plastic behavior of the sample at the beginning of the hold period. If the drift was larger than +0.1 nm/s this meant that the sample surface was colder than the tip surface and during the drift hold period the tip was shirking in size and moving in a positive direction. In order to remedy this the temperature of the sample would be raised to meet the temperature of the surface of the tip. If the drift was larger than -0.1 nm/s the opposite process would take place to lower the sample surface temperature to the tip surface temperature. After calibration process was performed to ensure an isothermal contact the sample would be move so that microcantilever was back under the tip and the piezo stage would be used to run a topography scan to locate the precise location of the microcantilever. After the scan, the loading location would be chosen in the same way as the described in the room temperature testing procedure above. The peizo scanning would be repeated for each microcantilever that was tested at that temperature. If a microcantilevers were to be tested at addition temperatures the thermal drift check (isothermal contact calibration) would be completed at each new temperature to ensure isothermal contact. After all of the temperature testing was competed the tip and specimen would be cooled down to room temperature in the reducing environment of Ar+5%H_2. The UO_2 specimen would be removed from the micromaterials hot stage so that optically and SEM microscopy could be perform on the microcantilevres.

2.6 In-Situ SEM Testing of Microcantilevers

For the in-situ testing of the UO_2 microcantilevers a Hysitron PicoIndenter (PI)-85 and PI-88 systems were used. The PI-85 system was used for initial room temperature testing and the PI-88 system was used for the elevated temperature testing. The following is the testing producer for the PI-85 room temperature testing. The UO_2 sample with microcantilever specimens is mounted on a SEM stub which is load into the sample stage holder of the PI-85 system which can be seen in Figure 2.9. The set screw that holds the SEM stub should be tighten "two-finger tight" as to avoid breaking the piezo electrics that drive the sample stage. After a UO_2 sample is mounted in the PI-85 sample stage, a 1 μm flat punch tip is mounted on the transducer of the PI-85 system. The surface of the UO_2 sample is manually placed as closes as possible to the tip and the set screw to hold the PI-85 sample stage is tighten. The alignment of the sample and tip is checked and then PI-85 system is loaded into the SEM/FIB dual beam instrument and all of the appropriate cables are attached to manipulate the stage and transducer. The cables are in feed-though located on the SEM chamber. The PI-85 system after it has been load in the SEM/FIB, the stage is tilted to 10-15º which allows the tip to be seen in both the SEM and FIB views. The tip is raise to the 10 mm working distance of the instrument because it only moves 5 μm which is the maximum distance of the transducer. The transducer calibrations are performed on the transducer of the PI-85 system when the sample is more than 5 μm away to ensure that the tip will not crash into the sample. After the tip is at the 10 mm working distance the microcantilever specimens are advanced with the PI-85 sample stage to the location of the tip. Having the ability to see the tip in both the SEM and FIB views allows for better and easier alignment of the tip and microcantilever. An example, of microcantilever ready for testing can be seen in Figure 2.10. The microcantilever tested in-situ were also tested in displacement control at 10 nm/s loading rate. The Hysitron is running a different feedback loop to control the tip so instead plateau at the brittle fractures we have load drops when there is a large sudden displacement move. A load drop is present in the Hysitron load versus displacement curve, which can be seen in Figure 2.11, because the instrument reduces the load to keep that steady rate of 10 nm/s. After the fracture of the microcantilever the test is stop and the tip is retracted. The after images of the test are taken and the next specimen is moved into alignment for testing.

The elevated temperature in-situ SEM microcantilever testing was performed with a Hysitron PI-88 system. An image of the Hysitron PI-88 system can be seen in Figure 2.12. The Hysitron PI-88 system also independently heats the tip and sample stage to allow for fine tuning of the temperature to have an isothermal contact similar to the MicroMaterials ex-situ indenter. The alignment producer is similar to PI-85 but due to the increased size and addition conditions to the way the PI-88 is loaded it is not possible to view the tip in both beams even with tilting. The alignment is performed by ensuring that the tip and the microcantilever were both in focus in the SEM view at the same time. This is roughly aligns the tip and microcantilever specimen in the same plane. Then the quick approach feature in the Hysitron software is used to bring the microcanitlever and tip into contact or see if there was a miss alignment. The quick approach feature advances the sample stage of the PI-88 at predefined step (50 nm in this case) until the transducer feels a predefined threshold load (30 μN in this case) at which point the sample stage stops advancing and retracts

200 nm back from the sample surface. After the alignment at room temperature the UO_2 sample was retracted 200 µm and the sample and tip were heated. The sample and tip are heated at 20 ºC/minute with 10 minute hold time at the desired temperature for stabilization. The microcantilever was then realigned at temperature and tested. All of the testing at elevated temperature was performed in displacement control and with a loading rate of 10 nm/s until failure of the microcantilever at which point the test was stopped.

Examining the UO_2 phase diagram as seen in Figure 2.1 and the temperature range that the microcantilevers are being tested in (RT-600 ºC) it can be observed that at an extremely low oxygen content is a needed to prevent the additional oxidation of UO_2. The vacuum in the SEM is approximately 10^{-6} torr (1.3E-9 atm) which is not a high enough vacuum to prevent the oxidation of UO_2 to U_3O_8. In order to prevent the oxidation of the UO_2 samples the low vacuum configuration on the Quanta 3D FEG instrument was used. The low vacuum configuration allows for the operation of the SEM/FIB instrument at a vacuum but with purging and feeding of auxiliary gas. The operation vacuum in low vacuum mode is between 0.1-2 torr. The auxiliary gas used was N+5%H_2 mixture to form a reducing environment in the SEM/FIB chamber. The pressure in the chamber during normal operation was 0.4 torr and the chamber was purged 20 times between 0.4-1.49 torr at the beginning of heating or whenever the temperature was increased during testing. The reason for using a N+5%H_2 mixture instead Ar+5%H_2 mixture is that Ar is heavy than air and the microscope pumps have been calibrated for pumping air. If there was sustained use of the Ar gas the pumps on the microscope could overheat and get damaged.

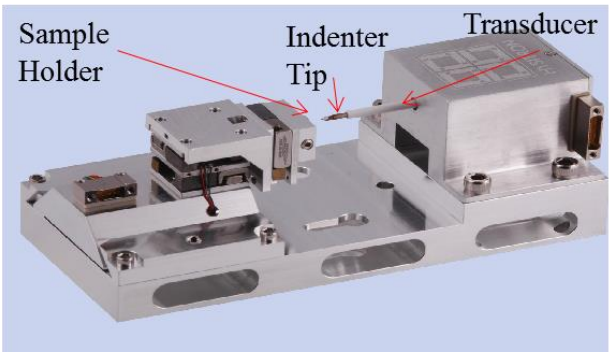

Figure 2.9: An image of the Hysitron PI-85 picoindenter. The sample holder, indenter tip and transducer are labeled on the image [108].

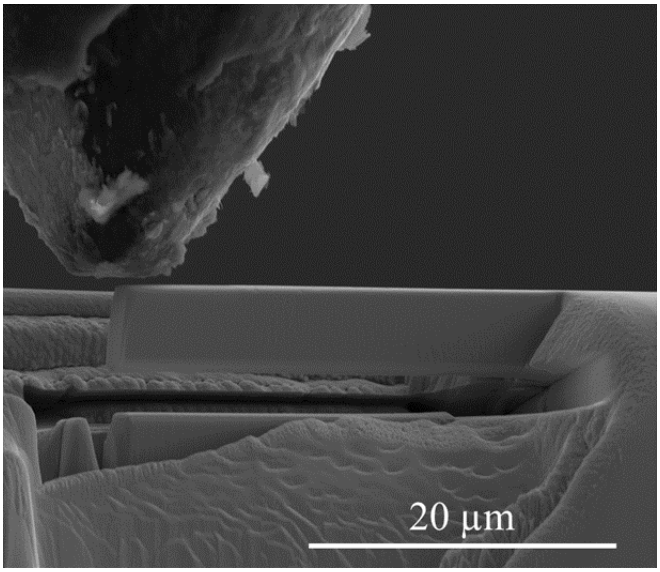

Figure 2.10: An image of rectangular microcantilever ready for testing in-situ in the SEM with the PI-85 system.

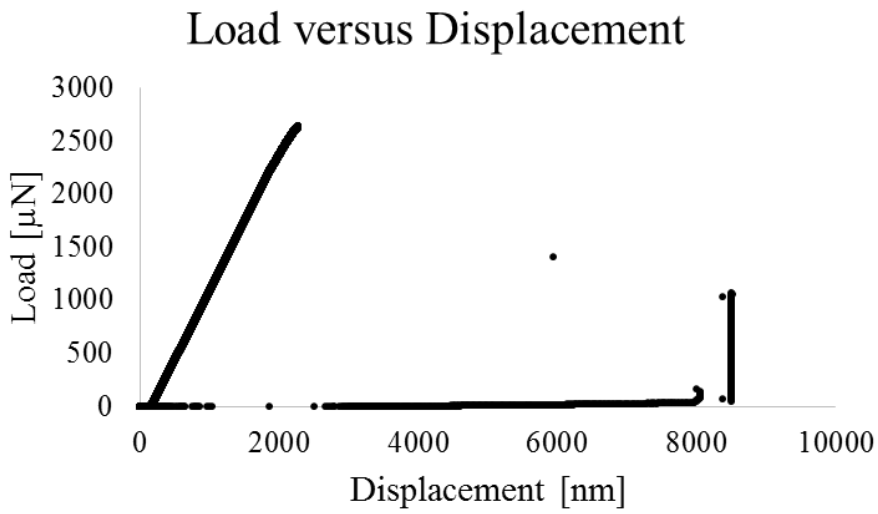

Figure 2.11: A load versus displacement curve from an in-situ SEM test of a rectangular microcantilever.

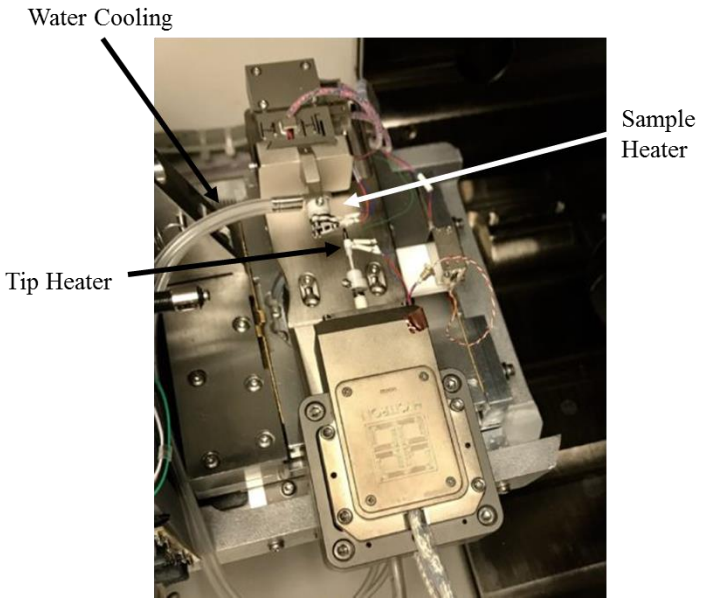

Figure 2.12: An image of the Hysitron PI-88 system on the SEM stage. The PI-88 allows testing at temperatures up to 800 ºC in the SEM. The sample heater and tip heater as well as the water cooling have been labeled in the image.

2.7 Nanoindentation

Nanoindentation and nanoindentation creep studies were performed on polycrystalline UO_2 and pre-strain polycrystalline UO_2. Nanoindentation and nanoindentation fracture toughness studies were performed on 3 spark plasma sintered (SPS) samples with different grain sizes. The polycrystalline UO_2 samples were the same samples that was used for the microcantilever experiments that are described above. The pre-strain UO_2 was polycrystalline sample was first loaded at 1200 ºC at 180 MPa for 6 hours with a total strain of ~0.6% prior to the nanoindentation experiments. The SPS samples were manufactured at Rensselear Polytechnic Institute (RPI). The 3 UO_2 samples from RPI that were sent to UC Berkeley for nanoindentation testing were nanocrystalline (125 nm), 2 µm grain size sample, and 10 µm grain size sample. The nanoindentation of all of the samples was performed on the MicroMaterials indenter located at UC Berkeley. The chamber purging process as described above was used for the nanoindentation at high temperature. The polycrystalline and pre-strained UO_2 samples were tested at room temperature, 100 ºC, 300 ºC, and 500 ºC. The SPS samples from RPI were tested at room temperature, 300 ºC, and 600 ºC. The nanoindentation was performed in load control with a loading to the maximum load in approximately 20 seconds and unloading in approximately 10 seconds. The maximum load for each temperature was varied to achieve approximately the same depth for the indent for each temperature tested. In addition, the indenter was test on fused silica to produce an area function for the tip for the calculations of hardness and elastic modulus before and after the high temperature testing. The frame compliance of the nanoindenter was also calibrated prior to the indentation.

Nanoindentation Creep

Nanoindentation creep studies were also performed on the polycrystalline un-strained/fresh UO_2 and pre-strained UO_2 at 300 ºC and 500 ºC. In a nanoindentation creep test the maximum load is held at for an extended time during which the change in displacement is measured. In this study the maximum load was held for 300 seconds.

2.8 In-situ Transmission Electron Microscopy

In addition, to the in-situ SEM microcantilever in-situ TEM microcantilevers were manufactured to observe possible dislocation motion during testing. The in-situ TEM microcantilevers would allow for observing possible deformation mechanism during the loading of the microcantilever that could not be observed with the in-situ SEM microcantilevers. The microcantilevers were tested with a Hysitron PI-95 system in a JEOL 3010 microscope at the national center for electron microcopy (NCEM). An image of the Hysitron PI-95 system can be seen in Figure 2.13. The microcantilevers were produced using conventional TEM FIB liftout process. However, a key difference is that no protective Pt coating was place before the trenching as this would affect the results of the microcantilever test to be performed later. In addition, the in-situ TEM microcantilever specimens where manufactured from the corner of the sample which allowed for milling the bottom of the foil to be milled flat to have a flush mounting with the prepared Omniprobe grid. The manufacturing process for the in-situ TEM microcantilevers is as follows. The rough trenching was completed with 15 nA current and using the regular cross section patterns in the FEI software. This left an approximately 5-6 µm wide foil which was approximately 20 µm long and ~10 µm deep. The foil was then cleaned with 3-5 nA current until it was ~1-2 µm wide. At this point it was rotated 180º and undercut with a flat bottom with a current of 1-3 nA. This is possible as the foil was mounted on a 45 º holder and made at the corner of the sample. At this point the Omniprobe half gird was prepared for the mounting of the microcanitlever foil. This preparation involved cutting the top 1-3 µm of a post on the omniprobe half grid to manufacture a flat surface to mount the microcantilever foil on which was also possible because it was mounted in 45º holder as well. The microcantilever foil was then liftouted with a Pt gas injection system and an Omniprobe needle. The microcantilever foil is then mounted to the top of the post and welded down with the Pt. Once the microcantilever foil is welded to the top of the Omniprobe half gird post it removed from the instrument and mounted in a 45º holder. Having the microcantilever foil specimen on the 45º mount allows for same abilities as described in the in-situ SEM microcantilevers. The desired height and length of the in-situ TEM microcantilever is measured on the foil and then the FIB is used to mill the material away to allow for the deflection of the cantilever during testing. Once that material is remove the high stress region of the microcantilever is thinned to electron transparency. Only the area around the high stress region is thinned to prevent bending or curing of the microcantilever during the thinning process. It is possible to have foil start to bend if too large of an area is thinned which makes it more difficult to test and would cause a complex stress that would no longer be a cantilever test. In addition, having a larger cross section at the end of the microcantilever to hit in the TEM makes the testing simpler while this part of the sample does not contribute to the deformation regardless and therefore simplifies the procedure while not altering the data.

The in-situ TEM testing was performed at room temperature with a Hysitron PI-95 system. The Hysitron PI-95 system requires the use of a unique holder for the in-situ testing. In order to avoid problems with mounting and alignment later in the testing process the sample is mounted onto an Omniprobe half gird that is already mounted on a PI-95 specimen holder. This prevents issues later in the process with alignment during testing. The PI-95 system used for these experiments is the version compatible with the JEOL microscopes. This is beneficial because the tips are interchangeable between the JEOL version of PI-95 and the SEM based PI-85/88 systems. During the initial testing period two different tips were investigated. The first being a standard Berkovich tip and the second being a 1 μm flat punch. Both tips were successful in testing the TEM microcantilevers however most of the testing utilized the 1 μm tip as the Berkovich tip had a tendency to slip off during testing. The mounting and testing producer for the PI-95 system was as follows. The appropriate tip was careful attached to the Hysitron PI-95 system. The sample mount was then attached to the PI-95 system and the tip was roughly aligned by eye with hand dials on the system. The PI-95 instrument was then load into the microscope and the normal start up producer for the microscope was followed. After which both the tip and microcantilever specimen were located in the microscope and the tip was brought within 10 μm but no closer than 5 μm of the microcantilever for the calibrations of the transducer of the PI-95 system. In the PI-95 system the sample is fixed and the tip is moved to the sample which is the opposite of the PI-85/88 systems. As a quick rough alignment of the tip and sample the x/y wobble on the microscope was used to verify that the tip and sample were in the same plane. After the calibrations were complete the tip was fully retracted in the software and manually brought within 2 μm of the microcantilever specimen with the hand dials. The Hysitron software was then used to bring the tip to almost touching the microcantilever specimen at which point the automatic approach option was used to verify that the tip and specimen were in the same plane. The alignment of tip and specimen was completed both visual, by looking at the live image capture from the TEM's CCD and load and quick approach information from the Hysitron. After it was confirm that tip was aligned with microcantilever the following process was used to improve the alignment of the tip and microcanitlever. It would be confirmed that the microcantilever and tip came into contact both visually and by the load information on the software. The tip would then be retracted a few hundred nanometers and moved or up a few hundred nanometer and then automatic approach would be used again to see if contact is made again. If contact was made again then the same process would be used going in the same direction (up or down) until contact was not made. The tip would then be returned to the starting position and the other direction would be investigated this gave the ability to find the center of the microcantilever. The recipe for loading the microcantilever would improve the test as the tip was less likely to slip off during testing or have an uneven load that could cause a twisted in the microcantilever testing. An image of the in-situ TEM microcantilever ready for testing can be seen in Figure 2.14. After the center of the microcantilever was found it would be loaded in displacement control at 7 nm/s until failure. The microcantilever was mostly viewed in bright field mode during the testing. After testing the microcantilever would be investigated using a variety of TEM techniques but was limited as the PI-95 system only has one axis of tilt.

In addition to in-situ microcantilevers testing, in-situ TEM nanoindentation was performed on the samples to try and obverse dislocation motion and deformation mechanisms of the UO_2. The sample preparation is similar to what is described in the in-situ TEM microcantilever testing above expect that instead of milling a microcantilever shape two areas were thinned for in-situ TEM nanoindentation. In Figure 2.15 a finish sample ready for in-situ nanoindentation can be seen.

Figure 2.13: An image of the Hysitron PI-95 system for in-situ mechanical testing [109].

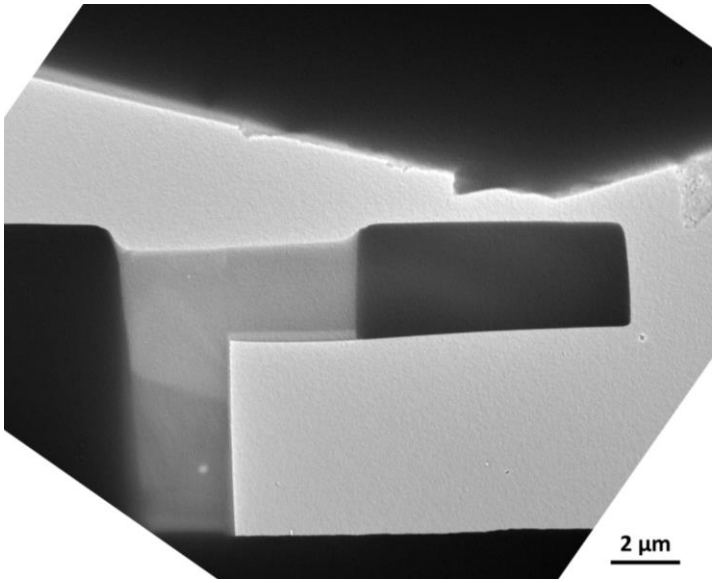

Figure 2.14: An image of in-situ TEM microcantilever being aligned for testing in the TEM with a diamond berkovich tip.

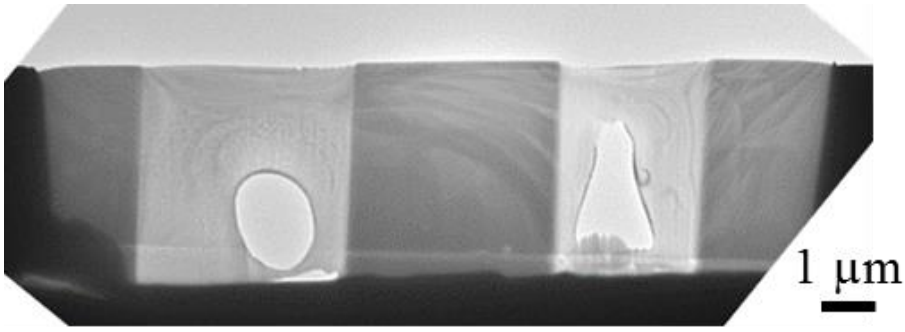

Figure 2.15: A TEM image of thinned locations ready for indentation in-situ in the TEM.

Helium Implantation of In-situ TEM Microcantilevers

In addition to performing in-situ TEM microcantilevers of single grains, the ORION nanofab at UC Berkeley was used to implant different doses of helium into manufacture microcantilevers prior to in-situ testing to investigate the effects of helium bubble formation on the deformation of the UO_2. An image of the Zeiss ORION nanofab instrument can be seen in Figure 2.16. The Zeiss can image with a Helium, Neon or Gallium beam. The Helium and Neon have gas field ionization source to from the beams which can be operated between 0-120 pA depending on the tip shape and stability. The same beams that are used for imaging can also be used for implanted ion species into the material. For this experiments the helium beam was used to image and implant helium into the thinned high stress regions of the TEM UO_2 microcantilevers. The helium was implanted perpendicular to the thinned region. The helium implantation energy was 25 keV which would penetrate approximately 133±54 nm using the SRIM software (quick calculation K-P) at a current of ~20 pA to doses of 1E17 ions/cm^2 and 1E18 ions/cm^2. An image of the helium ion distrubition from SRIM can be seen in Figure 2.17. After this the testing producer is the same as described in the in-situ TEM microcantilever cantilever section of this report. The only difference was that under and over focused images were taken to view the bubbles in the TEM but using the Fresnel contrast of the technique. A TEM micrograph of a microcantilever with helium bubbles can be seen in Figure 2.18.

Figure 2.16: An image of the Zeiss ORION nanofab. The Zeiss ORION nanofab can be used to image conductive and non-conductive samples with helium or neon ions. In addition, it can also implant helium into the material as well [110].

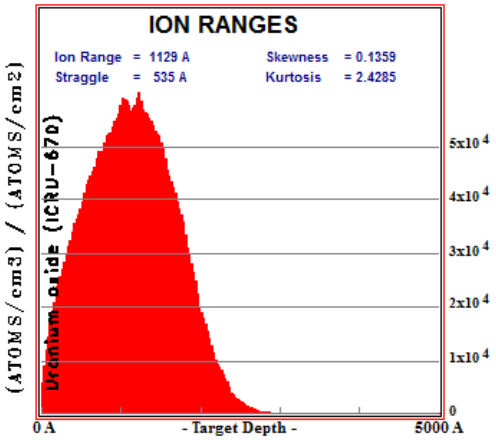

Figure 2.17: A plot from SRIM showing the depth of the helium ions with 25 keV would travel in UO_2.

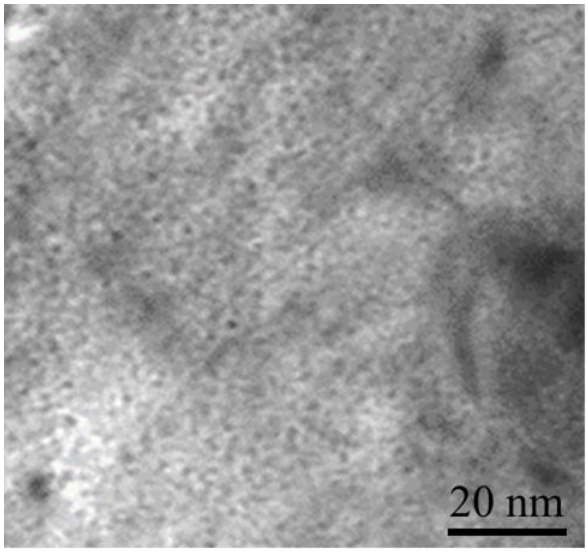

Figure 2.18: A bright field TEM image of a helium implanted UO_2 foil to a dose of 1E18 ions/cm^2. The defocus in is image is +500nm. The bubbles are the black spheres seen in the image.

Chapter 3

Results

3.1 Overview

This chapter is to provide all of the results that have been obtained during the work for this thesis. It will be divided into several sections as follow: ex-situ microcantilevers, in-situ SEM microcantilevers, nanoindenation, and in-situ TEM microcantilevers and indentation.

3.2 MicroCantilevers

Ex-Situ Microcantilevers

The ex-situ microcantilever were tested both at room temperature and elevated temperature in a MicroMaterials nanoindentation system. The system has Plexiglas chamber for environmental control to prevent the oxidation of UO_2. Prior to testing the orientations of the grains in the microcantilever was measured using EBSD.

Micro Structure Characterization of Ex-Situ Microcantilevers

In Figure 3.1 an example of an EBSD scan on the ex-situ room temperature microcantilevers can be seen. It can be observed that the microcantilevers contain a mulitple grains along the length of the microcantilever. In addition, it can be observed that the microcantilevers have a large amount of porosity that will have an effect on the results and calculations of the mechanical properties of the microcantilevers discussed in this section.

There were several microcantilevers made for the ex-situ elevated temperature testing however do to challenges with testing there was only one successful test at 300 ºC and one at 500 ºC. The EBSD of the successful microcantilevers can be seen in Figure 3.2 and 3.3.

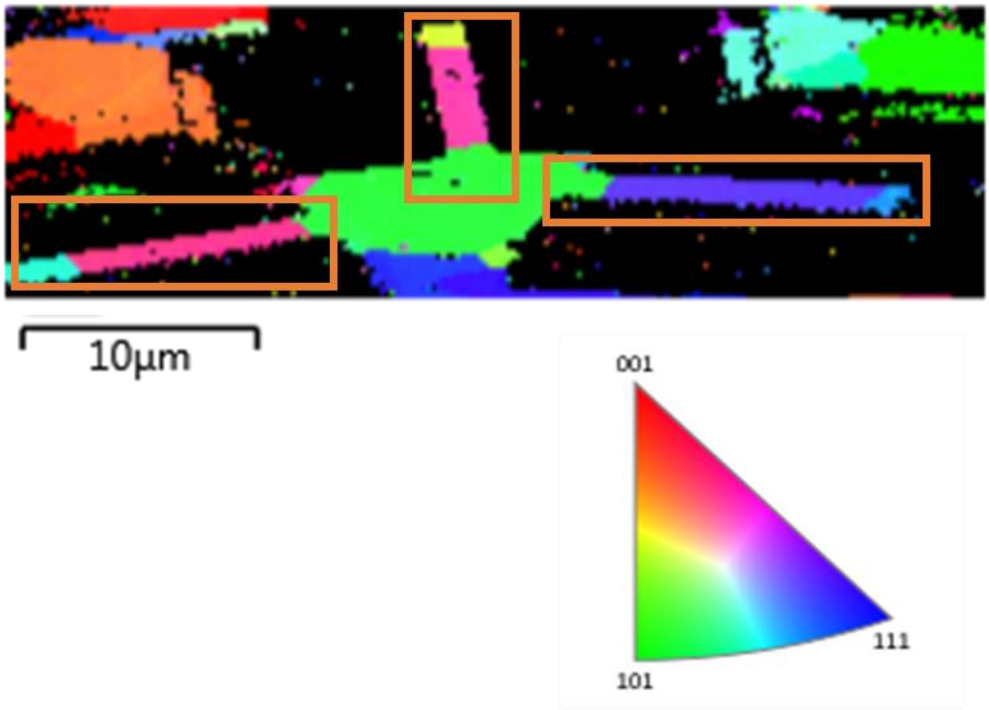

Figure 3.1: An inverse pole figure in the z (surface orthogonal) direction of ex-situ tested microcantilevers in the MicroMaterials indenter. The microcantilevers are surround by the brown boxes.

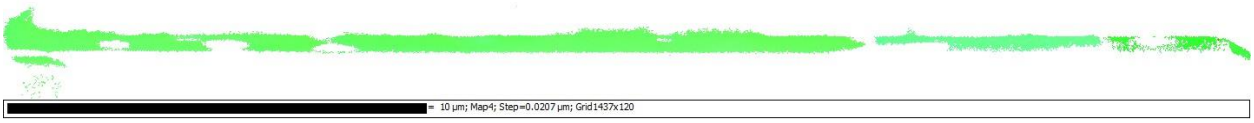

Figure 3.2: The Euler map of from the tango software of the ex-situ microcantilever that was successful test at 300ºC in the MicroMaterials indenter.

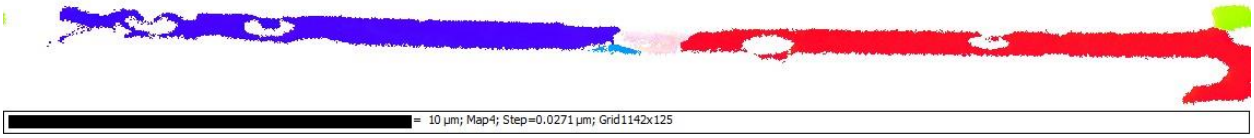

Figure 3.3: The Euler map of from the tango software of the ex-situ microcantilever that was successful test at 500ºC in the MicroMaterials indenter.

Test analysis and conversion to stress strain data.

As stated early there were more cantilevers manufactured than successfully tested due to challenges which will be address later in this section.

An example stress vs strain curve for the room temperature ex-situ tests can be seen in Figure 3.4. There were 11 successful ex-situ microcantilever tests at room temperature. The stress versus strain curves were calculated with the following equations.

$$E = \frac{PL^3}{3I\delta} \quad \text{Eq. 17}$$

Where E is the elastic modulus, P is the load from the indenter, L is the length between the fracture surface and the loading location, I is the moment of inertia, and δ is displacement at loading location which also comes from the indenter.

$$\sigma_C = \frac{PLy}{I} \quad \text{Eq. 18}$$

Where σ_C is the fracture stress, P is load from the indenter, L is the length between the fracture surface and the loading location, y is distance from the center of the moment of inertia (neutral fiber) to the upper surface, and I is the moment of inertia.

$$y = \frac{\frac{wb^2}{2}+\frac{w^2}{4}\left(\frac{w}{6}+b\right)}{wb+\frac{w^2}{4}} \quad \text{Eq. 19}$$

Where y is the distance from the center of the moment of inertia (neutral fiber) to the upper surface, w is the width of the microcantilever cantilever, b is the is the height of the square potion of the microcantilever. A cartoon of the "*upside down house*" design can be seen in Figure 2.2 which shows the w and b dimensions.

$$I = \frac{wb^3}{12} + \left(y - \frac{b}{2}\right)^2 wb + \frac{w^4}{288} + \left(\frac{w}{6} + b - y\right)^2 \frac{w^2}{4} \quad \text{Eq. 20}$$

Where I is the moment of inertia, w is the width of the microcantilever cantilever, b is the is the height of the square potion of the microcantilever as shown in Figure 3.5.

$$\varepsilon = \frac{\sigma_C}{E} \quad \text{Eq. 21}$$

Where ε is the strain, σ_C is the fracture stress, and E is the elastic modulus.

Figure 3.5 illustrate how this equations are combined together to produce the stress versus strain curves for the ex-situ and in-situ microcantilevers. The stress versus displacement and the elastic modulus versus displacement are both plotted. The large values at the beginning of the elastic modulus versus displacement plot are an artifact from the indenter tip both displacing the microcantilever and indenting into the microcantilever surface. The value for the elastic modulus calculated for the room temperature microcanitlevers is 83±53 GPa and the fracture stress was calculated at 518±200 MPa. The results for the individual ex-situ polycrystalline microcantilevers tested at room temperature can be seen in Table 3.1.

In Figure 3.6 is the stress versus strain curve for the successful 300 ºC ex-situ microcantilever test. It can be observed that there was no plastic deformation in the microcantilever at 300 ºC with the loading potion of the stress versus strain curve being completely linear. In addition, the elastic modulus calculated from Eqn. 3.1 is 186 GPa for the microcantilever right before the fracture of the microcantilever can be seen on the chart and matches well with the bulk values of UO_2 from modeling and macroscale testing [111]. The fracture stress calculated for the 300 ºC ex-situ microcanitlever is 2205 MPa.

In Figure 3.7 is the stress versus strain curve from the successful 500 ºC ex-situ microcantilever test. There is a deviation from the linear loading which could be plasticity in the microcantilever or possibly thermal drift during the test. The elastic modulus is also seen on the plot and is calculated in the linear potion of the loading curve and matches well with literature values seen in [111]. The value for the elastic modulus calculated for the 500 ºC microcantilever is 169 GPa and the fracture stress is 2425 MPa.

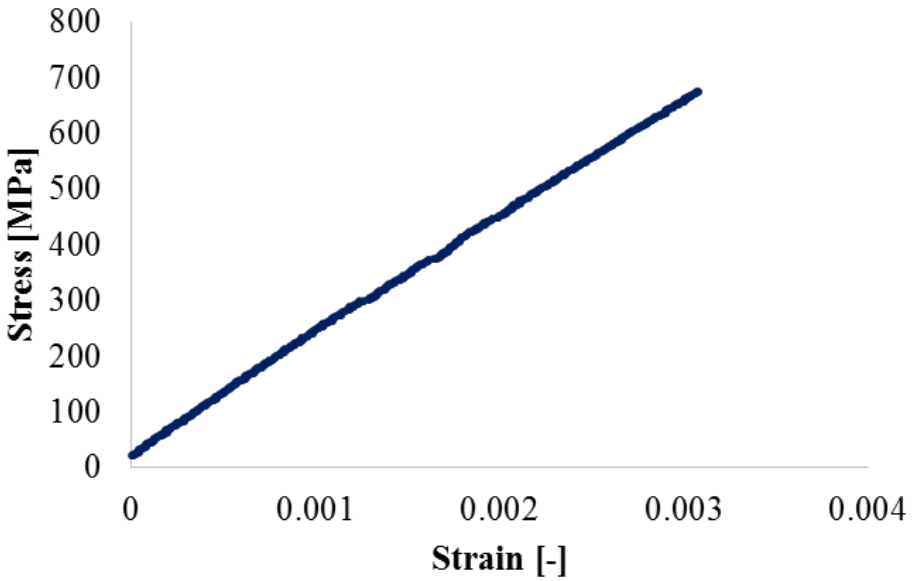

Figure 3.4: A stress versus strain curve for an ex-situ tested microcantilever in the MicroMaterials nanoindenter.

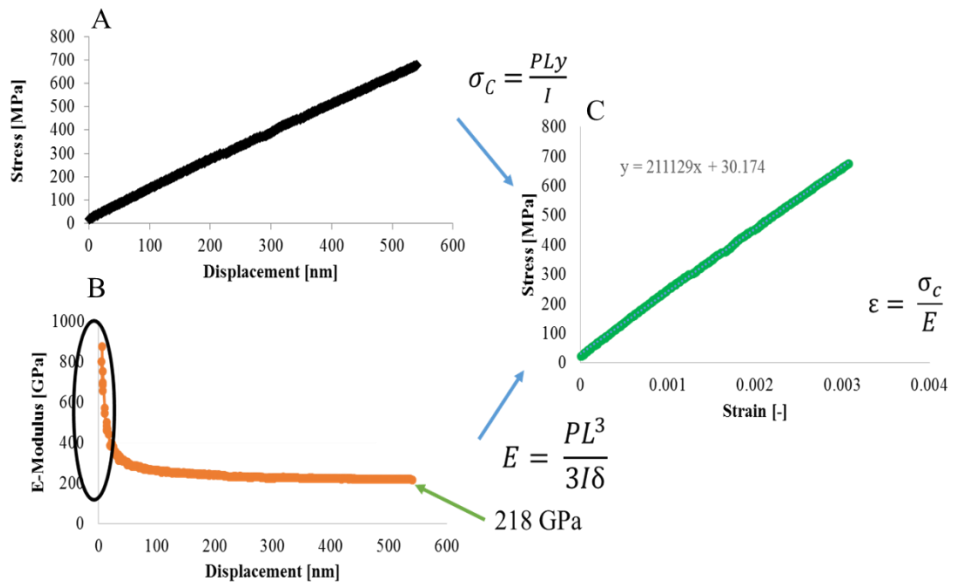

Figure 3.5: A visual representation of how the equations come together to produce the stress versus strain curves for the microcantilevers. A) The top left curve is the stress versus displacement curve. B) The bottom left curve is the elastic modulus versus displacement curve. The circle on the graph shows the high values of the elastic modulus that are calculated from the artifact of the indenter tip both penetrating into the material and bending the microcantilever. C) The right curve is the stress versus strain curve for the microcantilever.

Table 3.1: The results for the individual polycrystalline microcantilevers tested ex-situ at room temperature

Microcantilever #	Fracture Stress [MPa]	Elastic Modulus [Gpa]
1	388	82
2	863	64
3	714	86
4	347	84
5	236	31
6	217	28
7	499	84
8	675	218
9	762	116
10	352	54
11	644	67

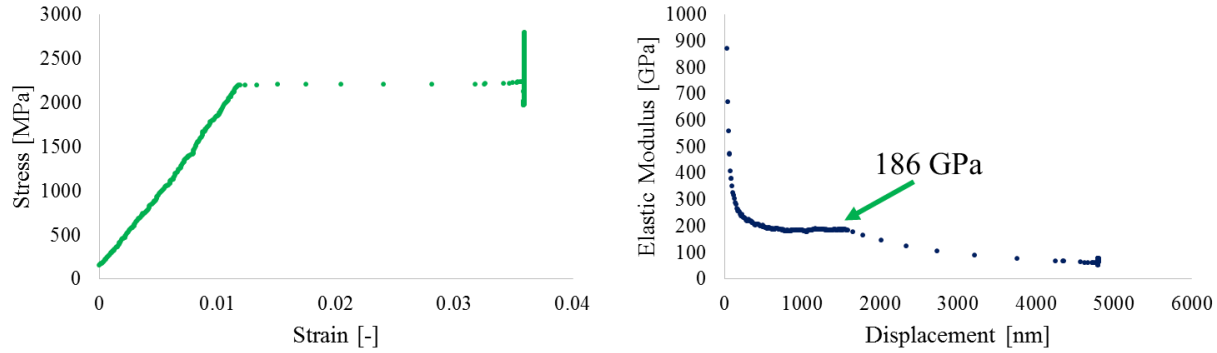

Figure 3.6: The stress versus strain curve on the left and on the right is the elastic modulus versus displacement curve for the successful tested ex-situ microcantilever at 300 ºC in the MicroMaterials indenter. It can be seen in the stress versus strain curve that the loading is linear elastic. In the elastic modulus versus displacement plot the modulus as fracture is 186 GPa.

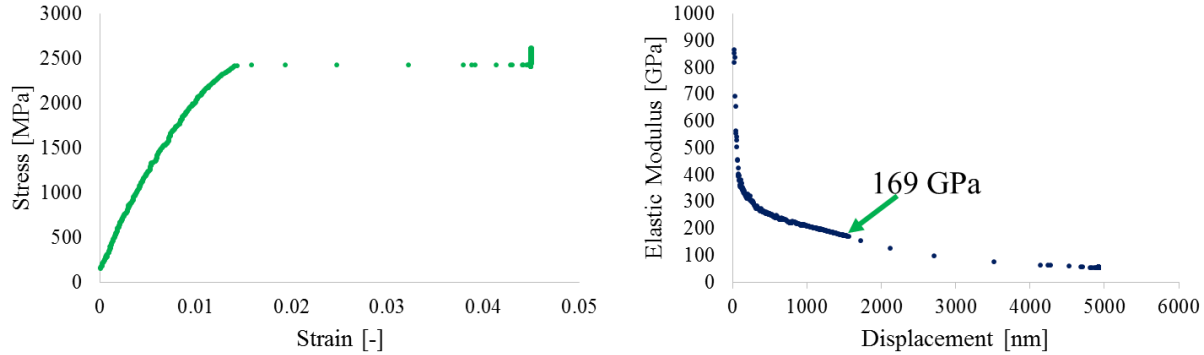

Figure 3.7: The stress versus strain curve on the left and on the right is the elastic modulus versus displacement curve for the successful tested ex-situ microcantilever at 500 ºC in the MicroMaterials indenter. It can be seen in the stress versus strain curve that the loading is not linear elastic. This could possibly be thermal drift or plasticity in the UO_2. In the elastic modulus versus displacement plot the modulus as fracture is 169 GPa.

Challenges of Room Temperature and Elevated Temperature Ex-situ MicroCantilever Testing

There were a few challenges in the testing of the ex-situ polycrystalline microcantilevers. Firstly, the porosity in the microcantilevers caused challenges in testing because it reduced the surface area in the fracture surface which made it difficult to calculate the elastic modulus and fracture stress. These reductions in fracture surface area are difficult to account for in the calculations so the original measured dimensions measured before fracture are used instead which greatly increases the spread in the results. Also, the pores caused the microcantilevers to not fracture at their intended fracture locations which caused difficulty in the measurements because the Lenght/Hieght (L/H) ratios and intended grain fraction of the microcanitlevers are not meet. The microcantilevers are supposed to have an L/H ratio of 5 in order to avoid subtract effects in the calculations [99, 112]. If the microcantilevers were not fracturing at their intended locations they would be no longer maintaining the correct length/height ratio. Also, these equations are assuming that the one end of the microcantilever is clamped which is not necessary the case if the microcantilever is breaking in the length of the microcantilever. In addition, modeling done by the ASU collaborators shows that results of the microcantilevers are most affected by the 1/3 of the microcantilever closest to the clamped end. So if microcanitlever had the closest 1/3 to the clamped end in one grain and the microcantilever fractured in a different location it can make the results difficult to interpret because it would be combining multiple grains together. An example of how the combination of elastic properties of different grains effect the calculation of the overall elastic properties can be seen in Figure 3.8. It can been observed in the results that all of the challenges greatly increase the spread with the fracture stress being 518 ± 200 MPa which is 38.6 % for a single standard deviation and for the elastic modulus it is 83 ± 54 GPa which is 65 % for a single standard deviation. This are quite large standard deviations for experimental data and make interpreting the data difficult. If the microcantilevers are separated into two groups one titled “Large pores” and the other titled “No or little pores” it can be seen that it helps reduced the data spread. The “large pores” group has a calculated fracture stress of 340 ± 140 MPa and an elastic modulus 60 ± 38 GPa. The “no to little pores” group has a calculated fracture 732 ± 105 MPa and an elastic modulus of 110 ± 62 GPa. Examples of these challenges can be seen in Figure 3.9.

Another, challenge is that as the microcantilever’s brittle fracture they can interact with other untested cantilevers as seen in Figure 3.9d. These large spreads in the data are a combination of the challenges discussed here and are the reason for moving to single crystal and in-situ mechanical testing.

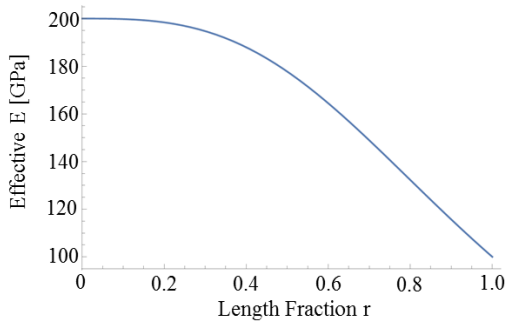

Figure 3.8: A model of microcantilever with two grains was produced. One grain had an elastic modulus of 200 GPa and other had an elastic modulus 100 GPa. The curve shows how the measured elastic modulus would change with different fraction of the 100 GPa grain. It shows that it would difficult to interpret data if the microcantilever didn't fracture in the indented location. This is because the elastic modulus measure would depend on the orientation tested in UO_2 because of the elastic anisotropy of the material.

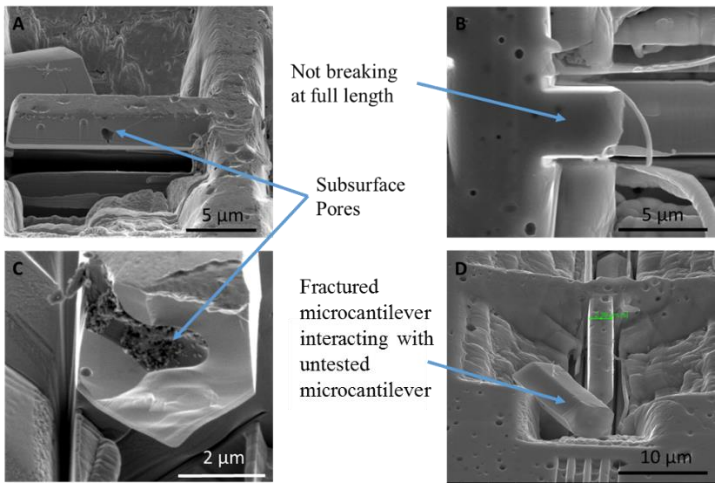

Figure 3.9: The images in this figure demonstrate some of the challenges faced when performing ex-situ microcantilever testing on polycrystalline samples. A) The image illustrates how subsurface pores can cause problems by making weak points in the microcantilever. B) The microcantilevers need to at intended fracture surface to minimize substrate effects in the calculations. If the microcantilevers break at their intended fracture surface that will meet the ratio of L/H > 5, however; if the microcantilever breaks in the middle then it will not necessary met this criteria. C) Additionally, pores take up part of the surface area in fracture surface making calculations difficult. D) Tested microcantilevers can interact with other microcantilevers which can cause problems with testing them.

In-Situ Mirocantilevers

In order to increase the yield of successfully tested microcantilevers the testing was moved from ex-situ testing in the MicroMaterials indenter to in-situ SEM testing with Hysitron PI-85 system. The ability to watch the test also increase the understanding of the data and allow for better calculations. In addition, to increase the understanding of the microstructure effects on the deformation of microcantilever EBSD was still performed on the microcantilevers before testing and a microcanitlever was not tested to fracture and sectioned. An EBSD scan was taken after each section to reproduce the whole volume.

3D EBSD Microcantilever

In order to evaluate how the microscturture (multiple grains) of the microcantilever was affecting the calculated and modeling results a microcantilever was loaded but not to failure at room temperature. So the loading of the microcantilever was only in the elastic regime. After the loading the microcantilever was then sectioned with FIB multiple times and EBSD is used to evaluate the microstructure after each sectioning. All of the EBSD scan were then used to produce a 3D model of the microcantilver that could be loaded in computer software that could be compared to the experimental results. This experiment was performed because the modeling was having a challenges matching the experimentally measured elastic modulus with the modeling elastic modulus as discussed here. The 3D EBSD allows the observation of how the grain structure and porosity changed throughout the entire microcantilever which gives a more complete model of the microcantilever. The stress versus strain curve for this microcantilever can be seen in Figure 3.10 (was not tested to failure). In Figure 3.11 the EBSD scans after each sectioning of microcantilever can be seen. The modeling results and comparison of the data can be seen in Bowen's master thesis [35]. The synopsis of the results show that the microstructure in the closest 1/3 of the microcantilever to the clamp had the largest impact of the results of the microcantilever modeling results which included both the porosity and grain orientation in the closest 1/3 of the microcanitlever.

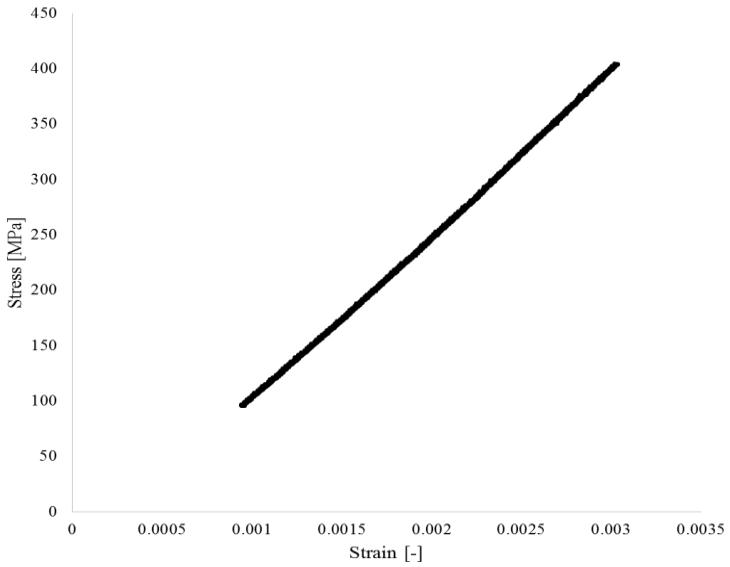

Figure 3.10: The stress versus strain curve for the 3D EBSD microcantilever. The 3D EBSD was performed to allow have a full view of the microstructural of the microcantilever. The microcantilever was not tested to failure at room temperature in the elastic regime.

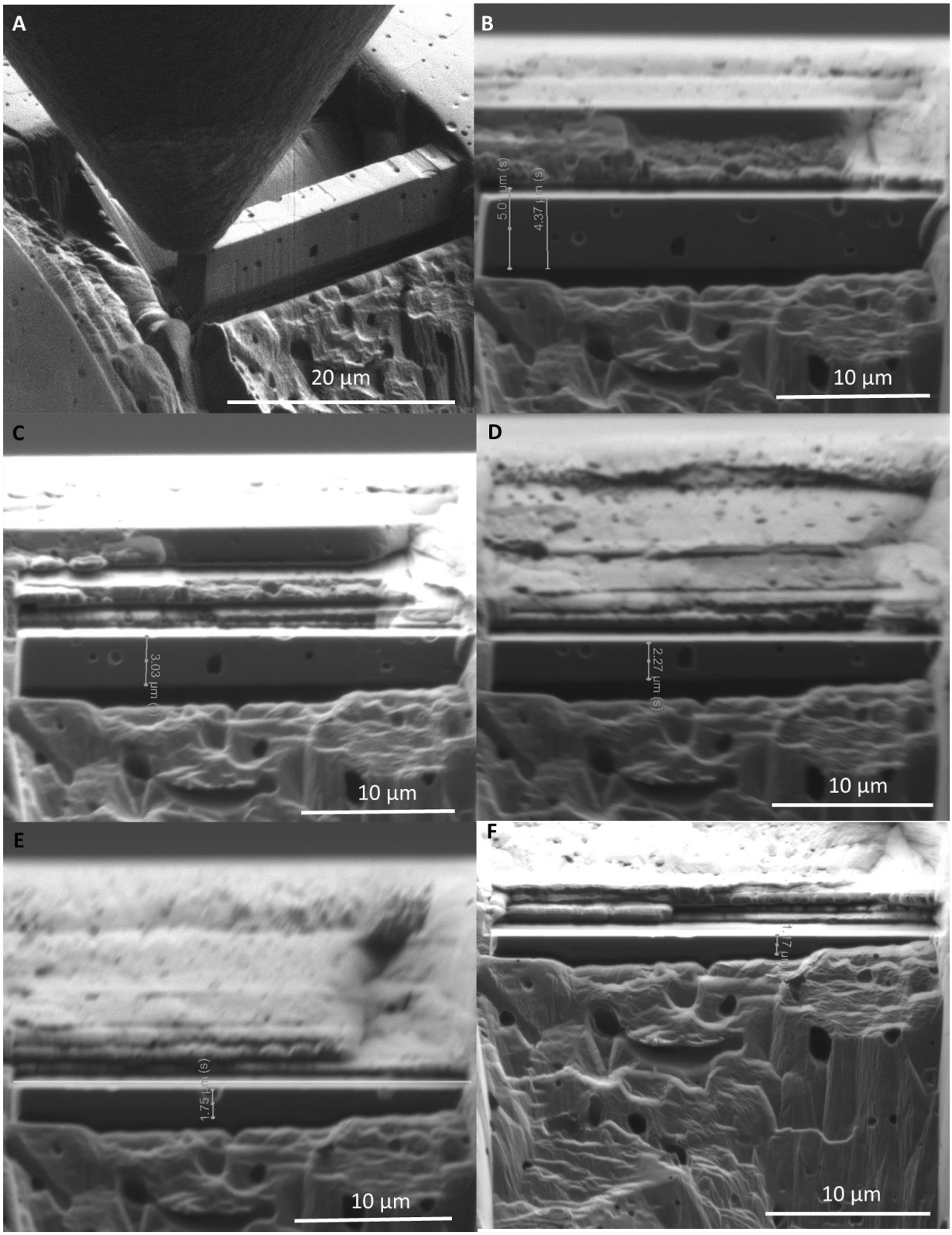
A
20 µm
B
5.0 µm (s)
4.37 µm (s)
10 µm
C
3.03 µm (s)
10 µm
D
2.27 µm (s)
10 µm
E
1.75 µm (s)
10 µm
F
1.7 µm (s)
10 µm

G

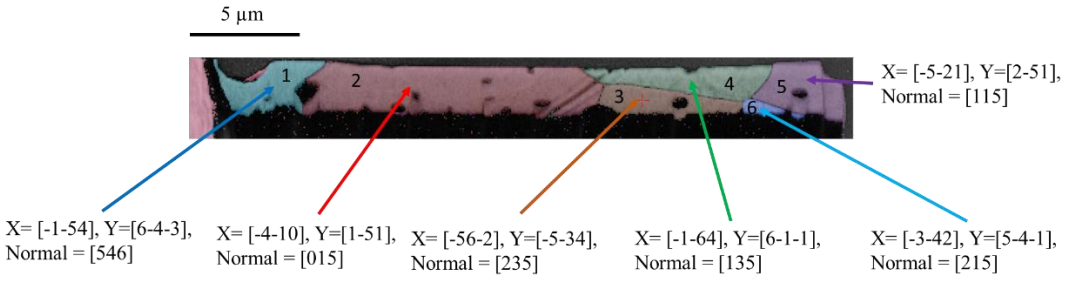
5 µm
1
2
3
4
5
6
X= [-5-21], Y=[2-51], Normal = [115]
X= [-1-54], Y=[6-4-3], Normal = [546]
X= [-4-10], Y=[1-51], Normal = [015]
X= [-56-2], Y=[-5-34], Normal = [235]
X= [-1-64], Y=[6-1-1], Normal = [135]
X= [-3-42], Y=[5-4-1], Normal = [215]

H

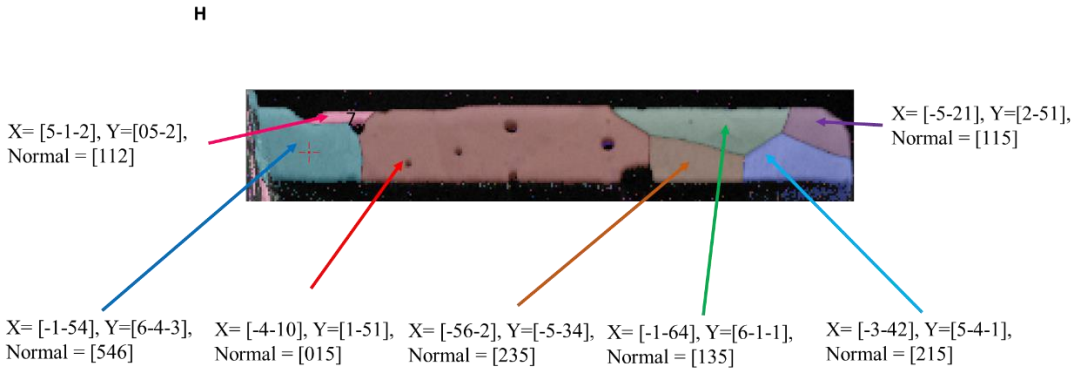
X= [5-1-2], Y=[05-2], Normal = [112]
X= [-5-21], Y=[2-51], Normal = [115]
X= [-1-54], Y=[6-4-3], Normal = [546]
X= [-4-10], Y=[1-51], Normal = [015]
X= [-56-2], Y=[-5-34], Normal = [235]
X= [-1-64], Y=[6-1-1], Normal = [135]
X= [-3-42], Y=[5-4-1], Normal = [215]

I

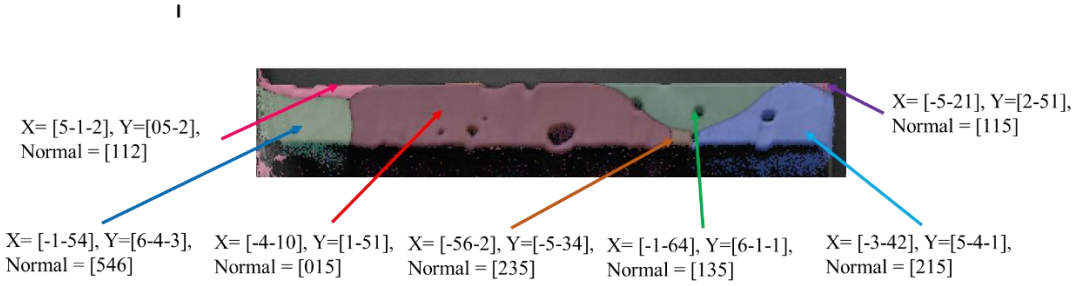
X= [5-1-2], Y=[05-2], Normal = [112]
X= [-5-21], Y=[2-51], Normal = [115]
X= [-1-54], Y=[6-4-3], Normal = [546]
X= [-4-10], Y=[1-51], Normal = [015]
X= [-56-2], Y=[-5-34], Normal = [235]
X= [-1-64], Y=[6-1-1], Normal = [135]
X= [-3-42], Y=[5-4-1], Normal = [215]

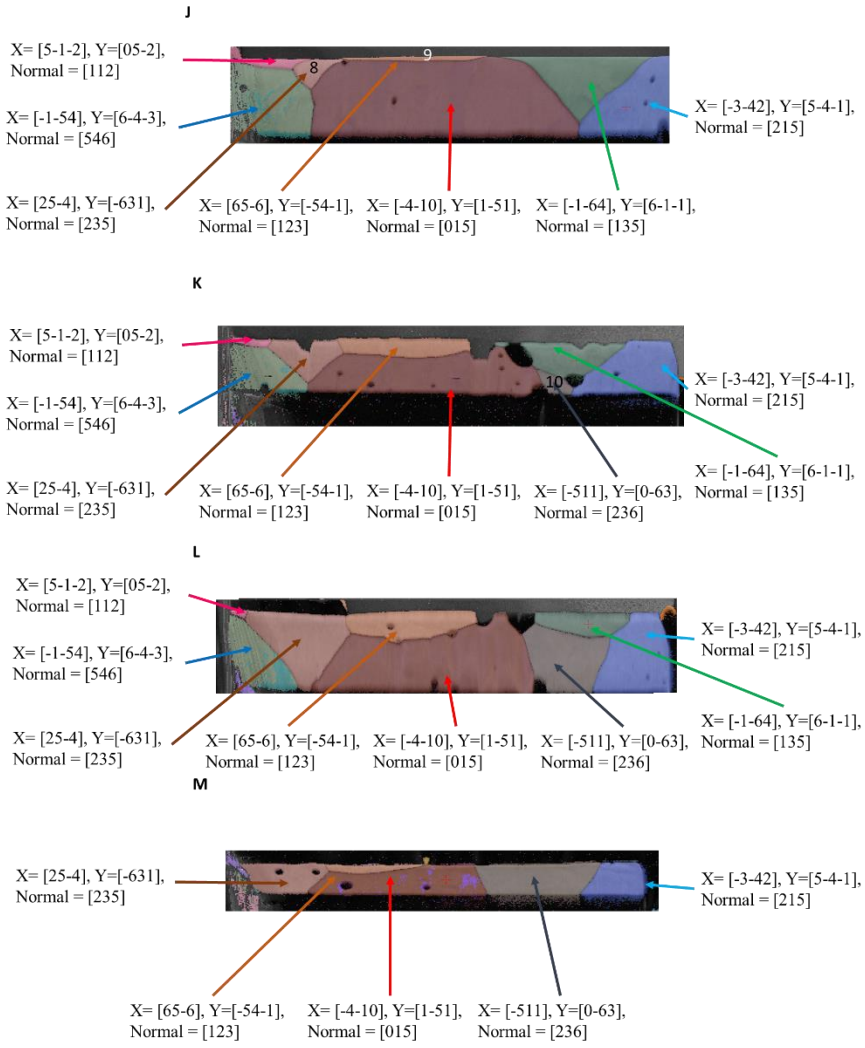

Figure 3.11: This figure shows the SEM images of the slices and the EBSD scan from the Tango software of the 3D microcantilever A) A FIB image of the microcantilever right after testing showing the top surface. The top surface corresponds to EBSD scan in G. B) The SEM image of the side of the microcantilever after the first slice of the microcantilever. This slice corresponds to the EBSD scan in H. C) The SEM image of the side of the microcantilever after the second slice of the microcantilever. This slice corresponds to the EBSD scan in I. D) The SEM image of the side of the microcantilever after the third slice of the microcantilever. This slice corresponds to the EBSD scan in J. E) The SEM image of the side of the microcantilever after the fourth slice of the microcantilever. This slice corresponds to the EBSD scan in K. F) The SEM image of the side of the microcantilever after the fifth slice of the microcantilever. This slice corresponds to the EBSD scan in L. G) The EBSD scan of the top surface of the microcantilever. H) The EBSD scan of the microcantilever after the first slice. I) The EBSD scan of the microcantilever after the second slice. J) The EBSD scan of the microcantilever after the third slice. K) The EBSD scan of the microcantilever after the fourth slice. L) The EBSD scan of the microcantilever after the fifth slice.

Single Crystal Results

To reduce some of the challenges of the polycrystalline material, a single (111) crystal of UO_2 was acquired from Los Alamos National Laboratory. The single crystal has little to zero porosity and the microcantilevers would be manufactured out of uniform material. It would also allow the ability to mill microcantilevers in predetermined orientations to study the elastic modulus along different orientations of UO_2. In addition, since the single crystal is uniform the microcantilevers could be manufactured on an edge or corner of sample which allows using the square geometry which is easier for the calculations. There were 4 sets of 3 microcantilevers milled in the UO_2. Each set had a different orientation which are labeled in the plot in Figure 3.12. In can be observed that each set's elastic modulus (slope of the stress vesus strain curve) is experimental reproducible. There is some spread in the fracture stress of the microcantilevers but the values are much higher than the porous polycrystalline values and the spread is much smaller than those tests as well. The percentage of standard deviation from the average value is smaller too. It should be noted that the green curves or the [16-6] group of microcantilevers did not fracture and can into contact with the substrate which is the cause for the large increase in the stress values observed in the plot. If that group [16-6] is removed from the results since they did not fracture and the other nine microcantilevers are examined, an average value of the elastic modulus is calculated at 176 ± 28 GPa which matches well with the theoretical value of 185-187 GPa [113]. In addition, 1 standard deviation is only 16 % instead of the 65 % as seen in the ex-situ polycrystalline material. This enforces the benefits of utilizing in-situ micromechanical testing as compared with ex-situ mechanical testing. The fracture stress for the microcantilevers that did fracture is large compared to other results from the literature [14-118] and the average value is 3256 ± 532 MPa. There is a large scatter in the values. However there was not enough tests performed to produce a weibull distribution for the data.

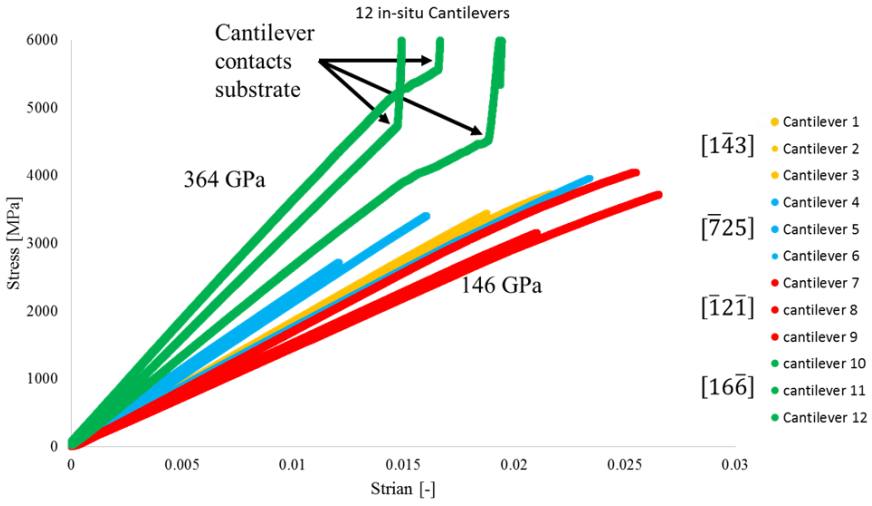

Figure 3.12: The stress versus strain curves for all of the in-situ room temperature tested single crystal rectangular microcantilevers.

In-situ High Temperature Single Crystal Results

The stress versus strain curves for the high temperature microcantilevers tested 570 ºC can be seen in Figure 3.13. There were 3 sets of 3 microcantilevers with each set being in a different orientation. The fracture surfaces of the 570 ºC microcantilevers can be seen in Figure 3.14. In addition, to the 570 ºC testing there were 2 microcantilevers tested at 300 ºC. The stress versus strain curves for those 2 microcantilevers can be seen in Figure 3.15. It is observed that the microcantilevers tested at 570 ºC did exhibit ductility during the testing while the 2 microcantilevers tested at 300 ºC are still completely linear elastically and then fail in a brittle manner. The average elastic modulus value calculated for the 570 ºC curves is 165 ± 24 GPa and for the 300 ºC curves is 164 ± 15 GPa. The decrease in the elastic modulus of the 300 ºC microcantilevers compared to the room temperature microcantilevers matches with the expected decrease from literature [107]. The elastic modulus for the 570 ºC does not match well with expected decrease in literature as compared with the room temperature microcantilevers. It can be seen from the stress versus strain curves that first of set of microcantilevers tested at 570 ºC higher elastic modulus which is increases the overall average. The average of the other 2 sets is 157 ± 6 GPa which better matches the expected values for the elastic modulus decrease [107]. The decrease in the spread for set 2 and 3 at 570 ºC could be contributed to an increase in the average H/L ratio and better testing practices. The H/L for sets 2 and 3 is in ~8-9 range while the first set is in ~6 range so that would greatly decrease the effects of the subtract. The microcantilever yield stress (using the .2 % offset method) for the 3 sets of microcantilevers tested at 570 ºC are as follows: 1586 ± 384 [-412 orientation], 783 ± 155 [1-21 orientation], 1579 ± 238 [-101 orientation]. The elongations for the fractured microcantilevers were 0.0153 ± 0.0068 [-412], 0.0124 ± .0063 [1-21], 0.0169 ± 0.0032 [-101]. In the [1-21] and [-101] only 2 of the 3 micorcantilever fractured when tested. The fracture stress for the 300 ºC microcantilevers is 2079 ± 288 MPa.

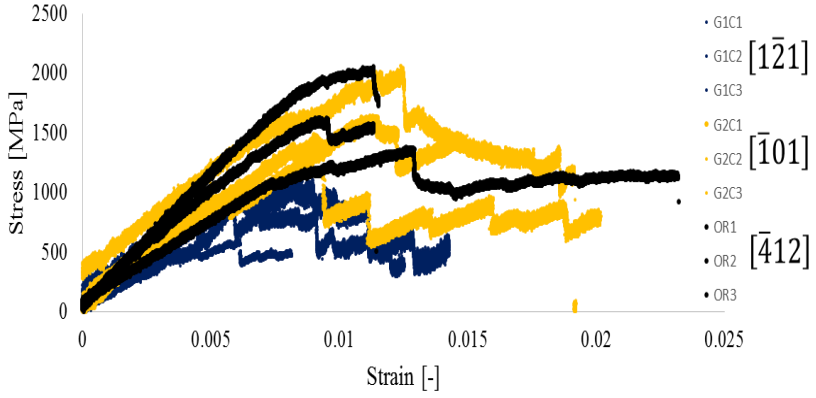

Figure 3.13: The 570 ºC curves for the single crystal microcantilevers.

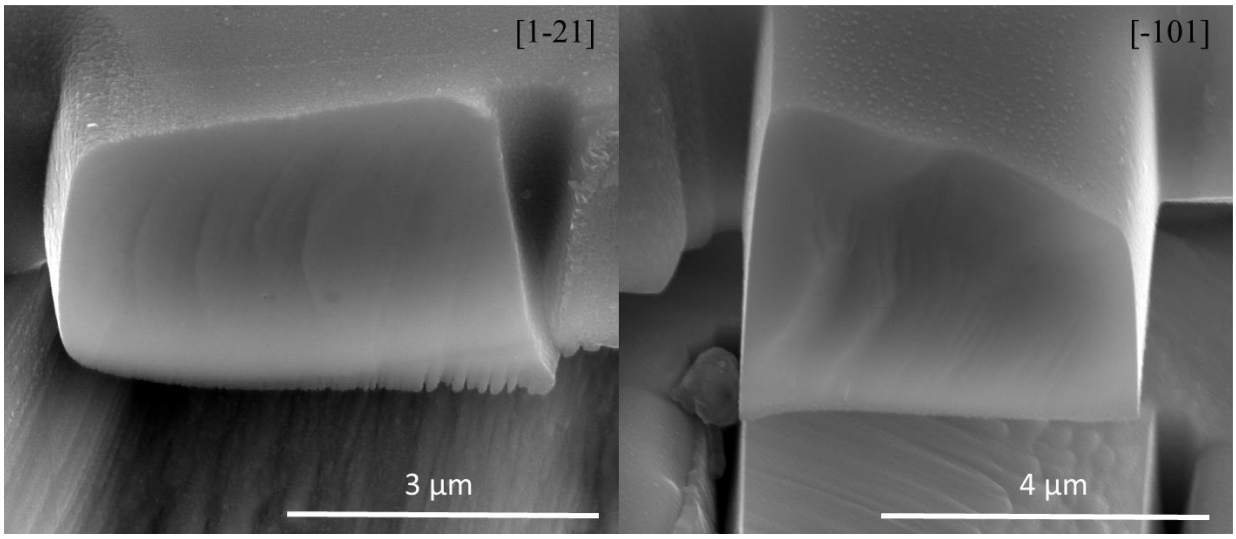

Figure 3.14: A few representative images of the fracture surface on the 570 ºC. The right image coming for the [1-21] set of the microcantilevers and the left image coming for the [-101] set of microcantilevers.

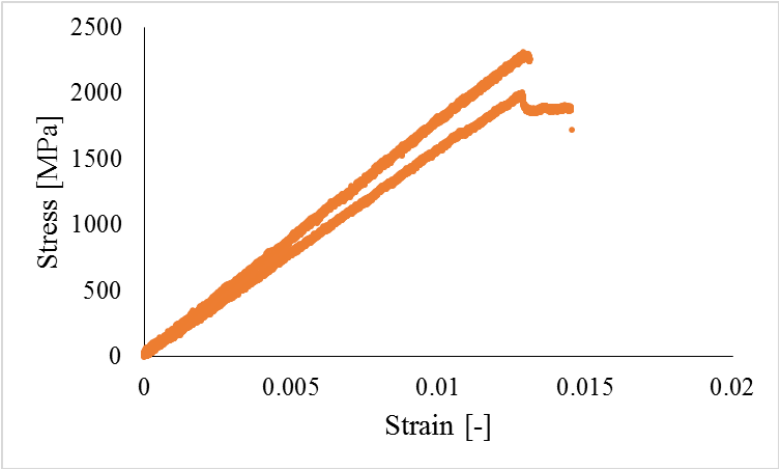

Figure 3.15: The stress versus strain curves for the microcantilevers tested at 300 ºC. The microcantilevers were in [-412] orientation. It can be seen that the loading was linear elastic which was also the case for the ex-situ microcantilever at 300 ºC.

3.3 Nanoindentation

Nanoindentation was performed on a variety of UO_2 samples to investigate the effects of grain size and defect density on the hardness and elastic modulus. In these studies both room temperature and elevated temperature nanoindentation was performed to evaluate the change in the mechanical properties as a function of temperature. Nanoindentation based techniques such as nanoindentation creep and nanoindentation fracture toughness were also used to increase the number of properties studied.

Polycrystalline Sample

The nanoindentation results for the polycrystalline sample can be seen in the plot in Figure 3.16. The values of the hardness, reduced modulus and elastic modulus at the tested temperatures are listed in table 3.2. The values measured for the elastic modulus match well with literature values with a value of 206 ± 7 GPa at room temperature to 175 ± 14 GPa at 500 ºC. The hardness is 10.75 ± 0.95 GPa at room temperature and decreases to 2.61 ± 0.23 GPa at 500 ºC. All of the indents went to approximately the same depth and were greater than 500 nm so there should be no size effects influencing the data. In Figure 3.17 there is a representative loading and unloading curves over the temperature range tested.

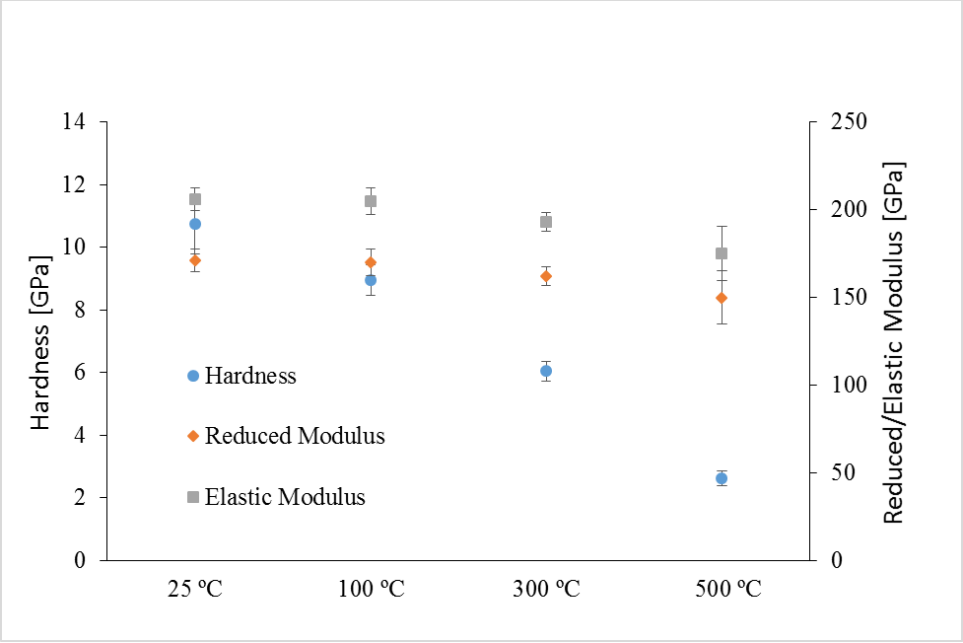

Figure 3.16: The nanoindentation results of the polycrystalline samples. All of the points represent the average of at least 10 indents. The blue circles are the hardness value over temperature. The reduced modulus and elastic modulus are both plotted. The elastic modulus is calculated from the reduced modulus from the equations given in the text.

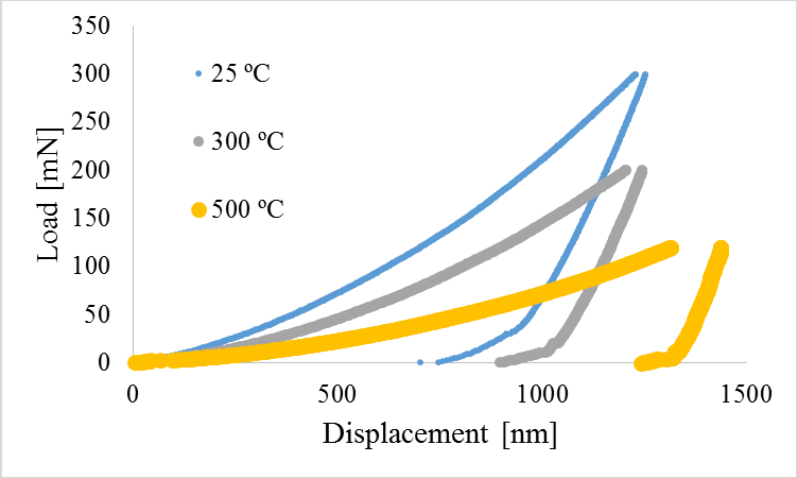

Figure 3.17: Representative loading curves for nanoindents performed in fresh polycrystalline UO_2 at different temperatures. The curve for 100 ºC is not shown as it reach a depth of only 500 nm. Since the indents are large there should be no size effects in affecting the results.

Table 3.2: The nanoindentation results of the fresh/unstrained polycrystalline UO_2 material

Temperature [ºC]	Hardness [GPa]	Reduced Modulus [GPa]	Elastic Modulus [GPa]
25	10.75 ± 0.95	171 ± 6	206 ± 7
100	8.96 ± 0.49	170 ± 8	205 ± 10
300	6.04 ± 0.31	162 ± 5	193 ± 6
500	2.61 ± 0.23	150 ± 15	175 ± 18

Spark Plasma Sintered RPI Samples

Rensselaer Polytechnic Institute (RPI) provided UC Berkeley with 3 samples with varying grain size which were nanocrystalline (125nm), 2 µm, and 10 µm. The nanoindentation results for the 3 different grain size materials can be seen in Table 3.3 and Figure 3.18. It can be seen that all 3 samples had approximately the same elastic modulus value over the tested temperature range which is consistent with literature values and the values measured on other UO_2 samples in this dissertation. The nanocrystalline had the highest hardness values which would be expected from the hall-petch relationship [119]. The nanocrystalline samples also maintains its higher hardness over the temperature range measured which be seen in Figure 3.18. The nanocrystalline sample had hardness of 12.47 ± 0.35 GPa at room temperature and 6.06 ± 0.79 GPa at 600 ºC. The hardness values for the 2 µm and 10 µm grain size samples were 7.72 ± 0.73 and 8.54 ± 0.72 respectively at room temperature. The values for 2 µm and 10 µm are in the range of other studies in the literature [120, 121]. The hardness values for the 2 µm and 10 µm were 1.74 ± 0.10 GPa and 1.77 ± 0.15 GPa at 600 ºC, respectively. The nanocrystalline material was more resistance to the increase in temperature losing approximately 50% of its room temperature value while the 2 µm and 10 µm lost 77% and 79% of their room temperature value, respectively. In addition to elevated

nanoindentation, nanoindentation fracture toughness measurements were performed on all three samples at room temperature. The values for the nanoindentation fracture toughness can be seen in Table 3.4. The 2 µm and 10 µm have a low fracture toughness that matches well with literature values [122-124]. In Table 3.3 the fracture toughness for the nanocrystalline size sample is not listed because it was not able to be accurately calculated due to the fact that the fracture mode does not allow the crack length to be measured. A representative image of the fracture toughness indent in nanocrystalline sample can be seen in Figure 3.19 illustrating that it did not meet the criteria for nanoindentation fracture toughness measurements.

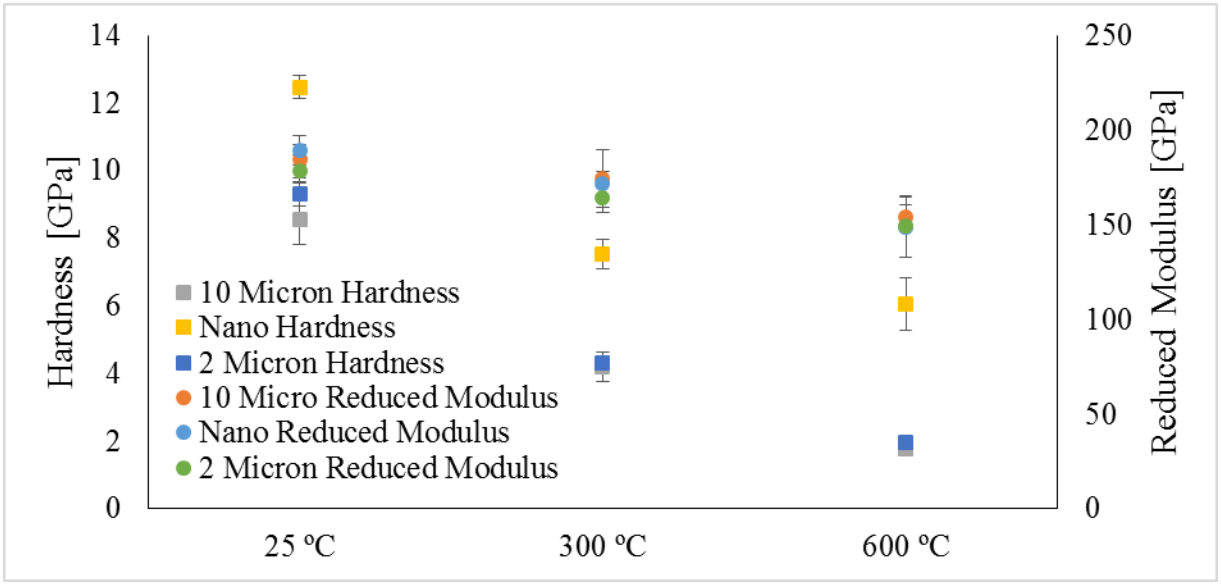

Figure 3.18: The results of the grain size effect study. There 3 samples in the study which were nano crystalline, 2 µm, and 10 µm grain size.

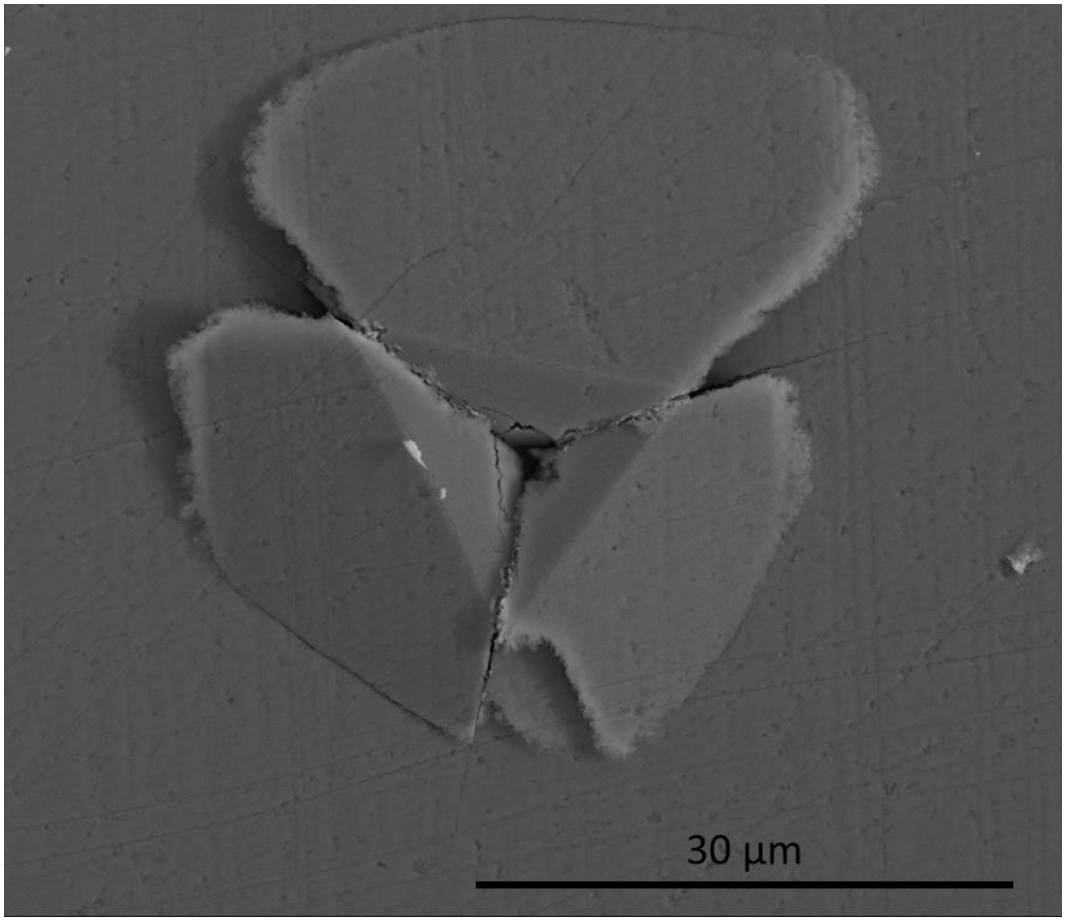

Figure 3.19: A SEM image of fracture toughness indent experiement showing the flaking that occurred on the nano crystalline sample instead of cracking.

Table 3.3 The nanoindentation results for the SPS samples from RPI

	Grain Size	25 ºC	300 ºC	600 ºC
Hardness [GPa]	nano	12.47 ± 0.35	7.54 ± 0.43	6.06 ± 0.79
	2 µm	9.30 ± 0.35	4.30 ± 0.21	1.98 ± 0.08
	10 µm	8.54 ± 0.72	4.22 ± 0.43	1.77 ± 0.15
Reduced modulus [GPa]	nano	189 ± 3	172 ± 7	149 ± 16
	2 µm	178 ± 3	165 ± 8	149 ± 15
	10 µm	185 ± 12	174 ± 15	154 ± 7

Table 3.4 The results of the nanoindentation fracture toughness on the SPS samples from RPI at room temperature (25 ºC)

Grain Size	Fracture Toughness [MPa $m^{1/2}$]
nano	n/a
2 µm	0.79 ± 0.12
10 µm	0.77 ± 0.16

Pre-Strained Sample

In order to evaluate the effects of an increased defect density on the deformation of UO_2 in our testing temperature range our collaborators at ASU pre-strained a polycrystalline sample at 1200 ºC at 180 MPa of stress until 0.6 % compressive deformation. The sample was then polished and sent UC Berkeley for elevated temperature nanoindentation and nanoindentation creep studies. The creep studies will be discussed in the next section of this dissertation. The results from the elevated nanoindentation studies from the sample can be seen in Figure 3.20 and Figure 3.21. In Figure 3.20 is the hardness and elastic modulus of the just the pre-strained material. The values for the hardness for the pre-strained material are 9.48 ± 0.10 GPa, 7.30 ± 0.50 GPa, 4.26 ± 0.10 GPa, 2.30 ± 0.10 GPa for room temperature, 100 ºC, 300 ºC, 500 ºC respectively. The elastic modulus values are 201 ± 4 GPa, 193 ± 6 GPa, 172 ± 4 GPa, 167 ± 6 GPa for room temperature, 100 ºC, 300 ºC, 500 ºC respectively. In Figure 3.21 is a comparison of the pre-strained and un-strained/fresh material. It can be observed from the plot in the Figure 3.21 that the pre-strained material has a lower hardness value at all of the temperatures tested. At the 500 ºC indents the values are much closer together. In addition, it can be seen that the elastic modulus for both samples are similar and decrease at similar rate over the temperature range tested. These values measured for the elastic modulus also agree with literature.

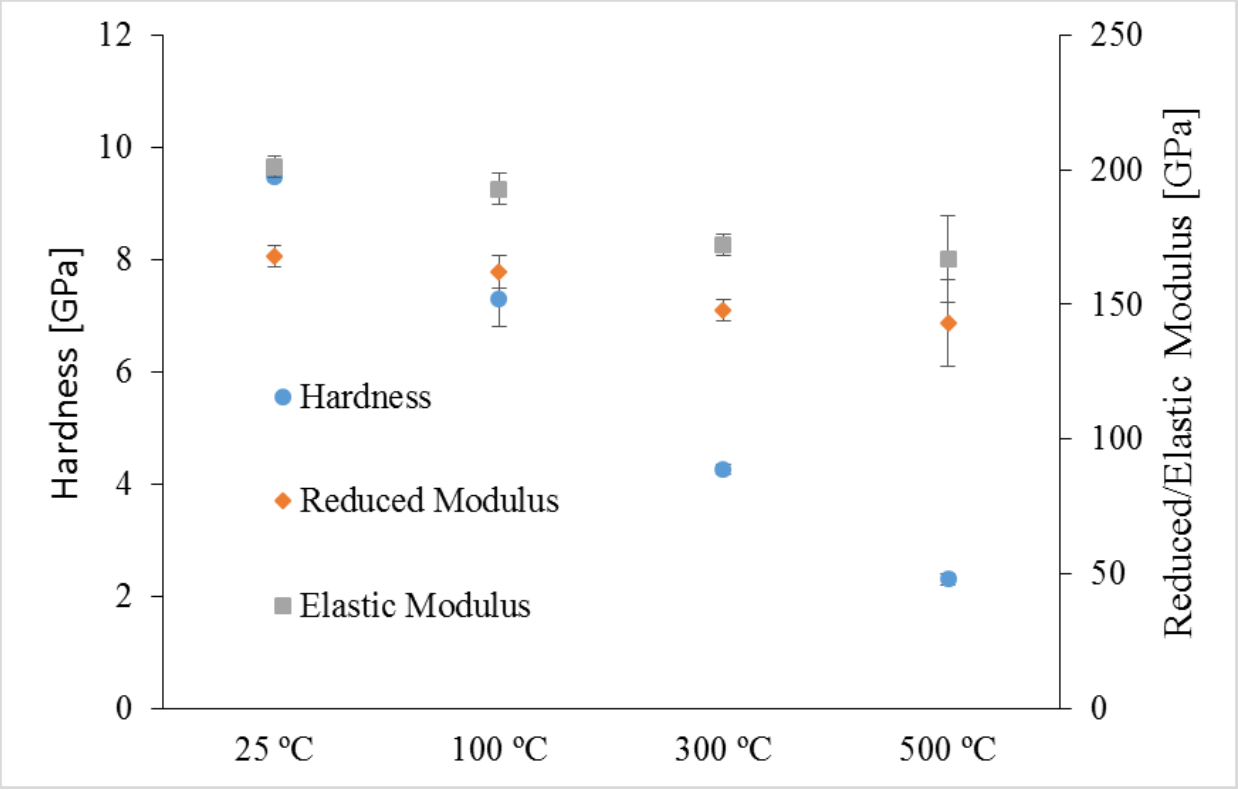

Figure 3.20: The nanoindentation results of the pre-strain samples. All of the points represent the average of at least 5 indents. The blue circles are the hardness value over temperature. The reduced modulus and elastic modulus are both plotted. The elastic modulus is calculated from the reduced modulus from the equations given in the text.

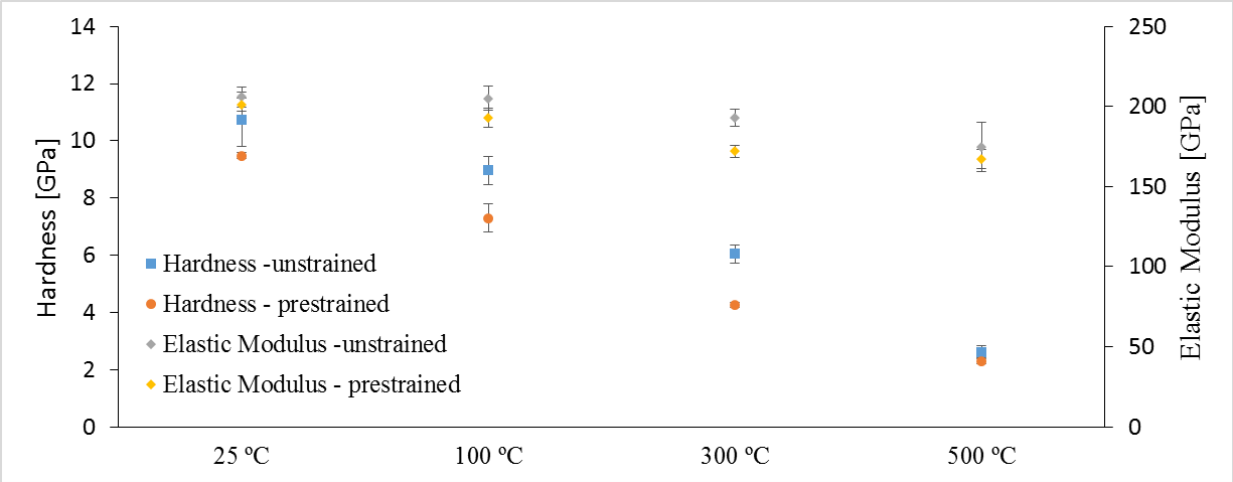

Figure 3.21: A comparison of the unstrained and prestrained hardness values. It can be seen that the prestrained material has a lower hardness values.

Nanoindentation Creep Results

In the nanoindentation creep experiments a load controlled indent is used to evaluate the creep in a sample. The indent is loaded up to a maximum load then held and the change in displacement is measured over a predetermined time. In these experiments the predetermined time was 300 seconds. Nanoindentation creep experiments were performed both on the un-strain/fresh and pre-strained sample to evaluate the effects of the deformation on the creep of the material. The creep experiments were performed at 300 ºC and 500 ºC on both the fresh/unstrained and prestrained material. The normalized curves for the nanoindentation creep experiments can be seen in Figure 3.22 for both testing temperatures. It can be observed that at 500 ºC the UO_2 material creep more in both cases as compared with the 300 ºC experiments. It can also be seen that the pre-strained material creeped more at both temperatures as compared with the un-strain/fresh material. The stress exponents for the 300 ºC and 500 ºC un-strained/fresh material are 17.9 ± 2.9 and 7.3 ± 1.0, respectively. The stress exponents for the 300 ºC and 500 ºC pre-strain material are 8.8 ± 0.2 and 4.7 ± 0.1, respectively. The nanoindentation creep exponents were calculated using the equations in the nanoindentation creep section in chapter 1. The exponent is calculated by plotting the Ln(strain rate) versus Ln(stress). In nanoindentation creep the stress is hardness as the hardness is a force over area calculation. The slope of the linear portion of the data is then calculated which gives the stress exponent. We can see the large decrease in the stress exponent with both temperature and pre-straining the material. The activation volumes calculated from the creep nanoindents are as follows: un-strained/fresh fuel are 1.90 b^3 and 2.68 b^3 for 300 ºC and 500 ºC respectively. The values for the pre-strained material are 1.47 b^3 and 1.68 b^3 for 300 ºC and 500 ºC respectively.

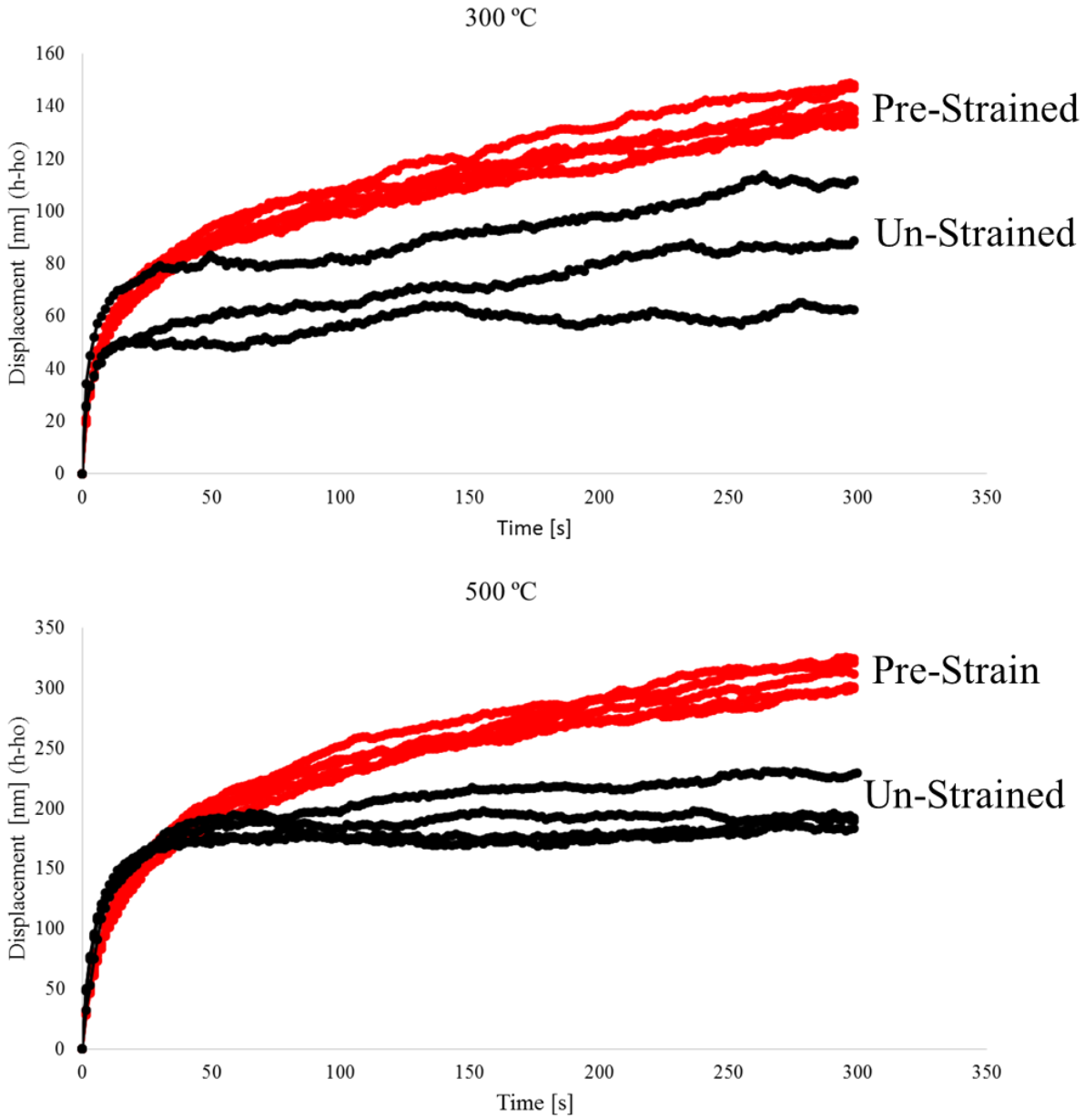

Figure 3.22: The creep curves of the unstrained (black) and prestrained (red) at the 2 temperatures 300 ºC and 500 ºC.

3.4 In-Situ Transmission Electron Microscopy

In-situ TEM Microcantilevers

The in-situ TEM microcantilever experiments were performed to observe any possible dislocation motion in the UO_2 during loading. In addition, when the microcantilevers were thinned to electron transparency it provided the opportunity to implant the microcantilevers with helium from the ORION nanofab to evaluate how the deformation of the UO_2 changed with helium bubbles.

Single Crystal Room Temperature

The in-situ TEM microcanitlevers were tested at the national center for electron microscopy (NCEM) located at Lawrence Berkeley National Laboratory. The testing was performed with a JEOL 3010 microscope and a Hysitron PI-95 picoindenter. Images of the tip and the microcantilever ready for testing can be seen in Figure 3.23. In Figure 3.24 a TEM bright field image a dislocation is visible after the testing of a microcantilever. The dislocation was observably during the in-situ mechanical test of the microcantilever. During the test is was observed that the dislocation did not move. If the standard cantilever equations are used the stress the dislocation experiences is 1050 MPa and the stress the microcantilever fractured at was 1970 MPa. In addition, the strain of the in-situ TEM microantilever was 0.0344. The stress versus strain curve for the in-situ TEM microcantilever can be seen in Figure 3.25. The addition in-situ TEM microcantilever tests had similar results.

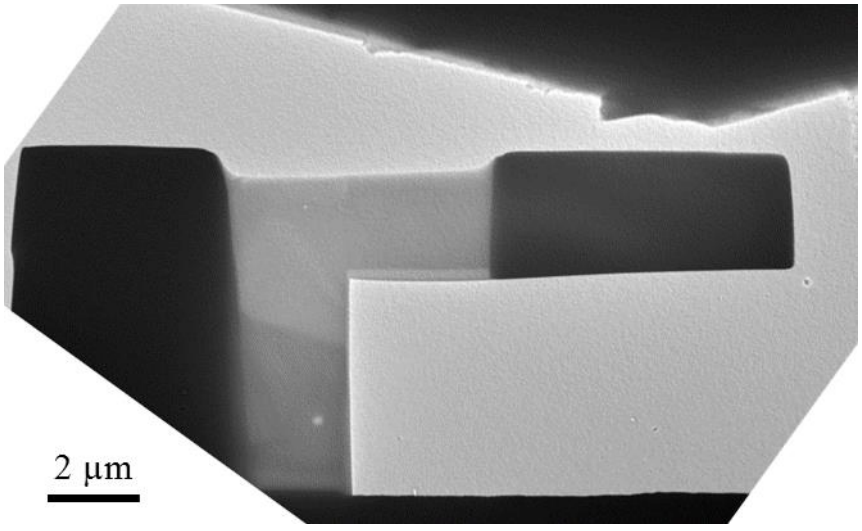

Figure 3.23: A cartoon showing how the microcantilever was load during the testing and to give the reader an understanding how the geometry of the testing apparatus.

Figure 3.24: An image of the in-situ TEM microcantilever after testing. The dislocation in the orange circle was visible during the test and it was observed that the dislocation did not move during the test.

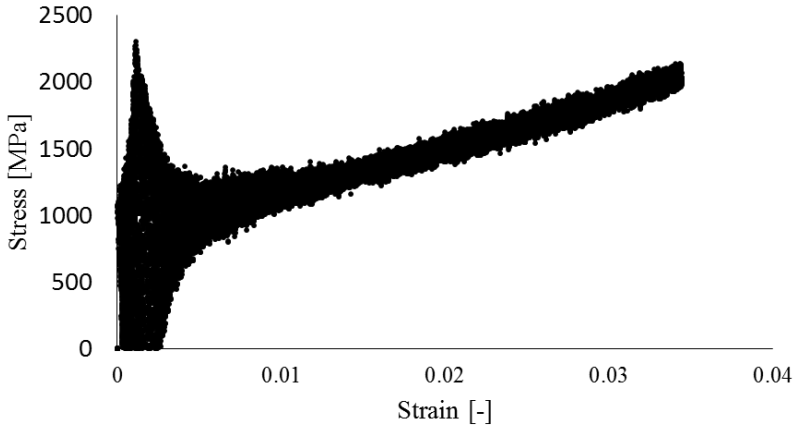

Figure 3.25: The stress versus strain curve for the in-situ TEM microcantilever with visible dislocation.

In-situ TEM Nanoindentation

In addition to the microcantilever, to try and observe the dislocation motion in UO_2 in-situ TEM nanoindentatoin was performed with the Hysitron PI-95 system. A standard Berkvoich was used for the indentation. The goal of these in-situ nanoindentation experiments was observe the deformation in real time which would allow the observation of plastic deformation and dislocation motion. The goal was not to calculate hardness values as the indented material would not be constrained. In addition, since an electron transparent foil was used the indenter tip would not be constricted and the calculation of the hardness would not be practical. These experiments showed that even when UO_2 is thinned to electron transparence and indented with a berkovich indenter it will still fail in a brittle manner. The images of the foils after indentation can be seen in Figure 3.26. The loading and unloading curve for the first indentation location and location that corresponds to the images in Figure 3.26 can be seen in Figure 3.27. In Figure 3.28 the second location for the in-situ TEM indentation can be seen before and after the indentation. The loading and unloading curve can be seen in Figure 3.29. There were some challenges with performing the in-situ nanoindentation which were mostly alignment issues. If the alignment was off the tip would slide off the foil and push the foil over instead of indenting the foil. In addition, the tip could slide down the side of the foil and it would be a failed test. In addition, it is possible to break pieces of the foil with indenter instead of performing an indent which can cause problems and destroy the indentation area. It can be seen in Figure 3.26 and 3.28 that there was no plastic deformation zone in the UO_2 foils and that indents caused cracks in the samples. Also no dislocation motion was observed during the testing of the samples.

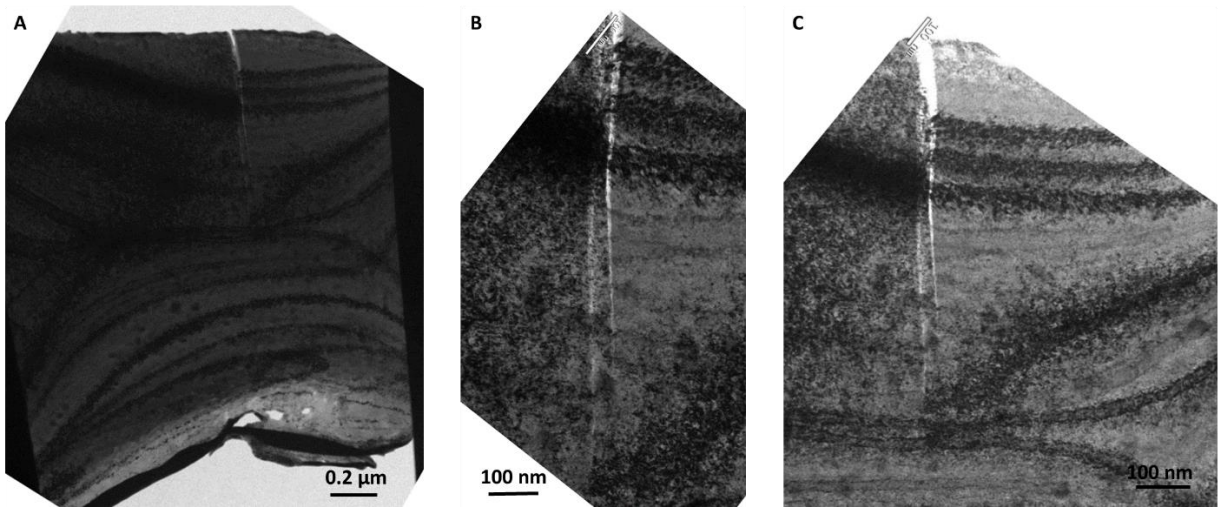

Figure 3.26: Results of the in-situ TEM indentation on UO_2 in location 1.

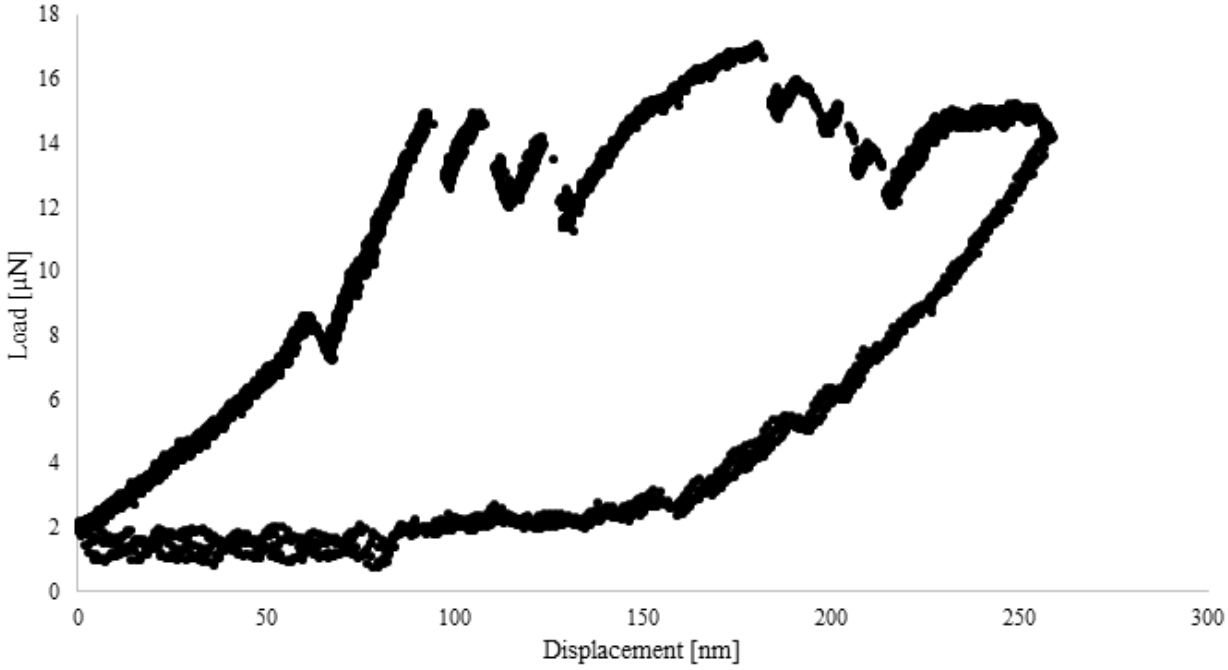

Figure 3.27: The loading and unloading curve for the in-situ TEM indentation in the UO_2.

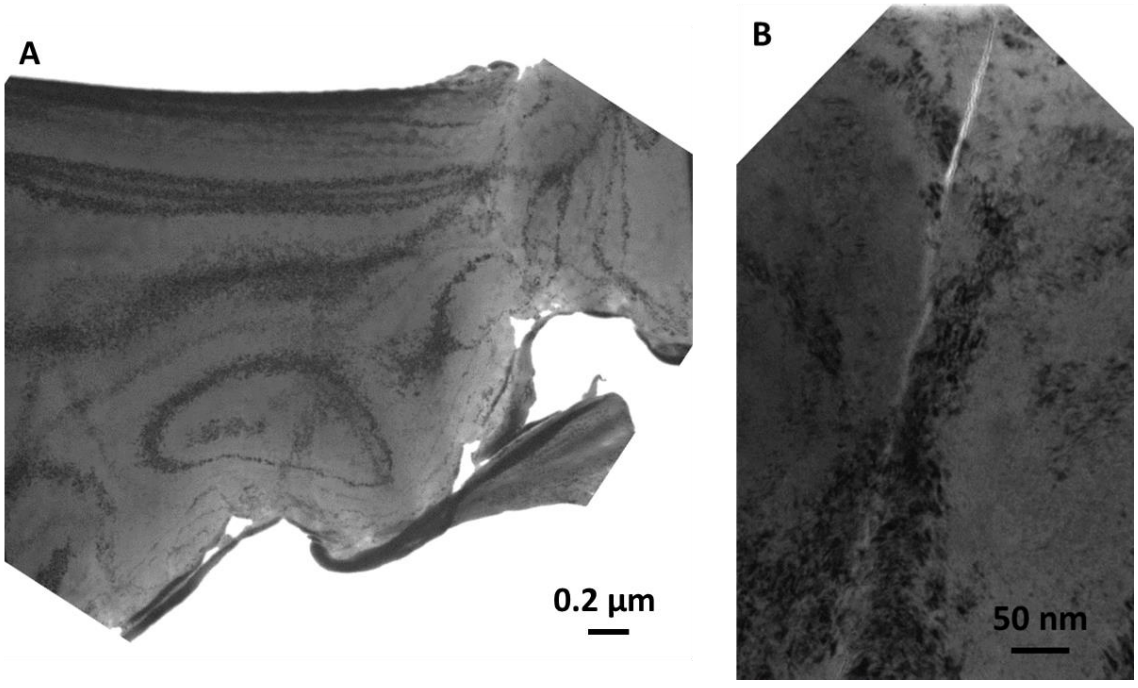

Figure 3.28: A) Before image of the second indentation location. B) The image of the crack cause in the UO_2 after the indentation.

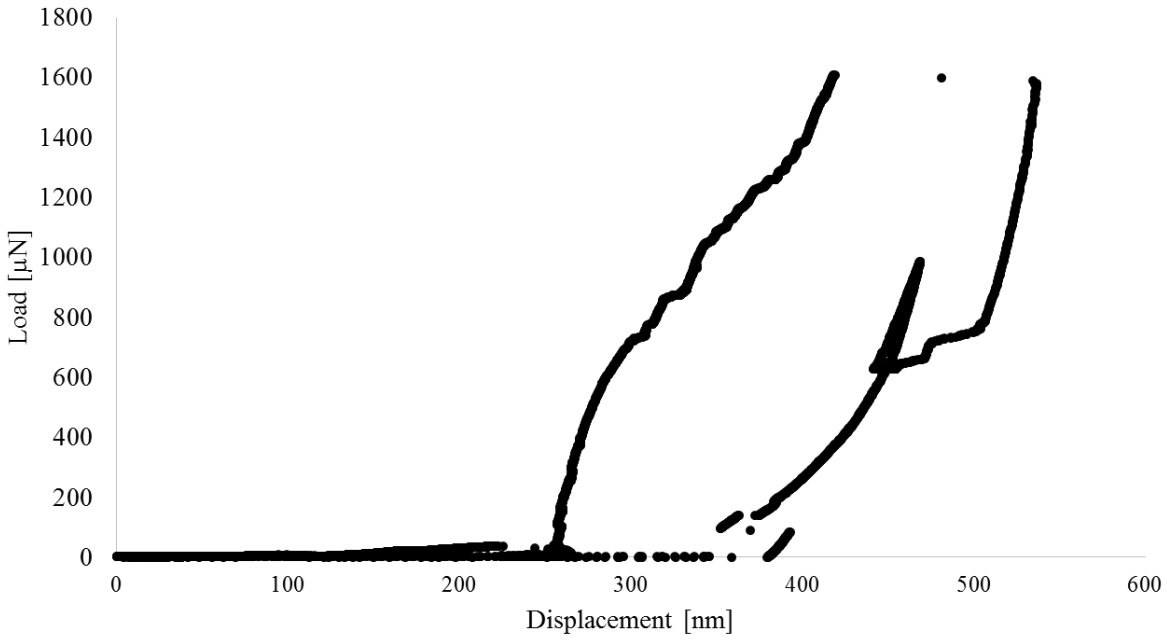

Figure 3.29: The loading and unloading curve of the second in-situ TEM indentation area.

Helium Implanted Room Temperature In-situ TEM Microcantilevers

In order to study the effects of the helium bubbles on the deformation of the UO_2 the in-situ TEM testing was used again. The samples were implanted with 25 keV helium at ~ 20 pA to doses of 1E17 and 1E18 ions/cm^2. Images of the implanted UO_2 in underfocused bright field images show the black circles which are the helium bubbles imaged using the fensel contrast technique describe earlier. The 1E17 ions/cm^2 deformed similar to the un-implanted material with one large brittle crack which can be observed in Figure 3.30a. However, the 1E18 ions/cm^2 dose sample deformed with a spider web of cracks with multiple pathways. The images of this microcantilever can be observed in Figure 3.30b. It can be observed that crack was deflected during deformation causing the crack to split and continue along many path ways.

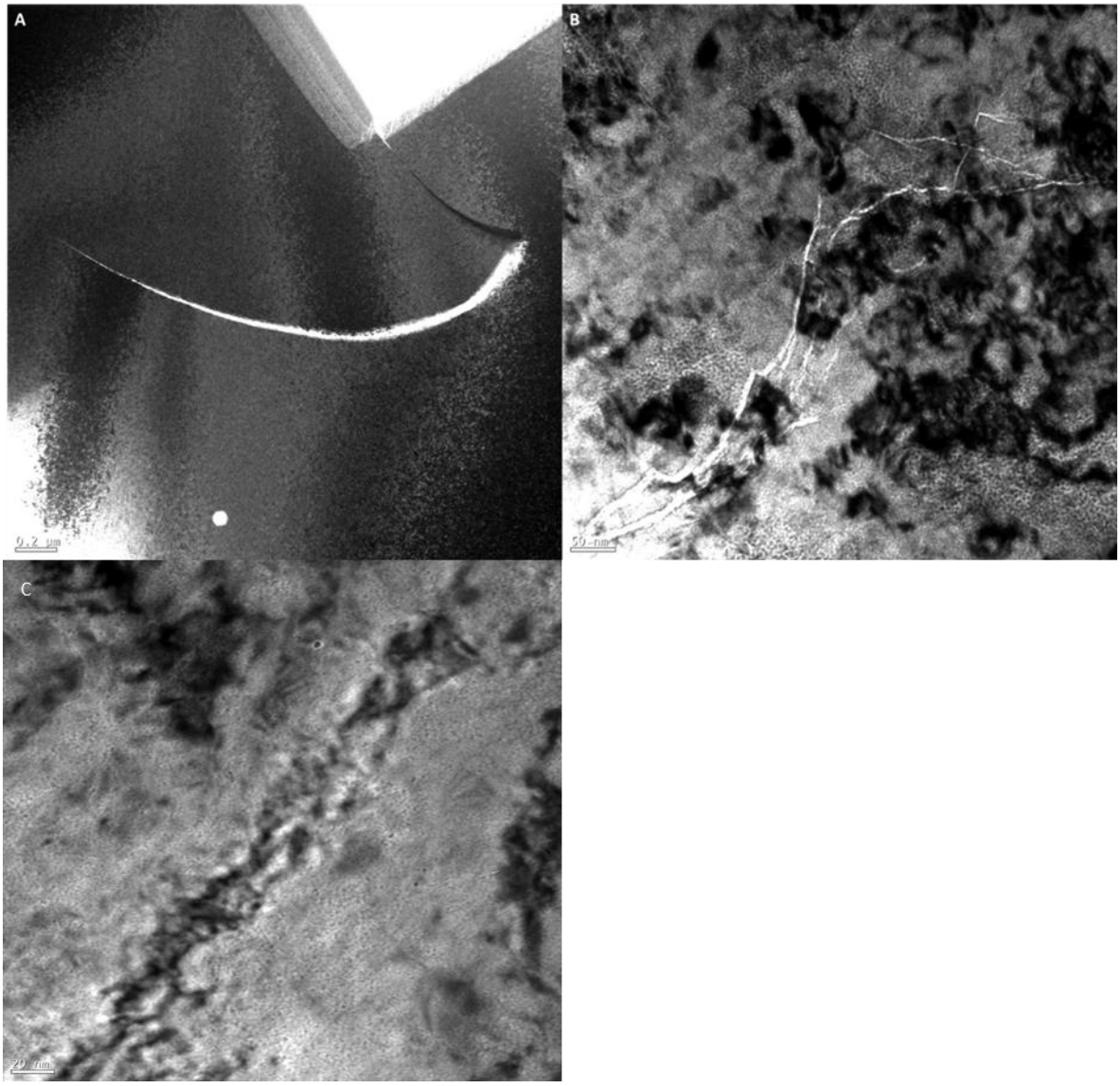

Figure 3.30: A) TEM bright field image of UO_2 microcantilever after testing. The microcantilever was implanted with 1E17 ions/cm^2. It can be seen that the implanted microcantilever failed similar to non-implanted microcantilevers. B) TEM bright field image of UO_2 microcantilever after testing. The microcantilever was implanted with 1E18 ions/cm^2. It can be seen in the image that the microcantilever did not fail with a single crack as with the non-implanted microcantilevers. Instead it had many cracks. C) An underfocus image of helium bubbles from the helium implantation using the Zeiss ORION nanofab to a dose of 1E18 ions/cm^2.

Chapter 4

Discussion

4.1 Microcantilevers

Ex-situ Room Temperature Microcantilever Testing Discussion

The results showed that the porosity of the UO_2 had a large effect on the fracture of the microcantilevers. This effect of porosity can be seen in the large standard deviations in the results of the fracture stress and elastic modulus which can be seen in Figure 4.1. In addition, in Figure 4.1 the microcantilevers with large pores and the ones with little to no pores in the fracture surface were separated and there is still large standard deviation on the values of these individual result. These initial microcantilevers were short which means that their L/H was not greater than 5 which indicates that there was substrate effects in the results that would lower the calculated values. This is especially important in the calculation of the elastic modulus as it has L^3 term. These substrate effects are an additional contributor to the fact that the calculated elastic modulus values for these microcantilevers are not in the range for the elastic modulus of UO_2. In addition, the porosity in the fracture surface had a large effect on the values of the fracture stress. This is case because in the calculations of the fracture stress only the initial dimensions of the microcanitlever were taken into account. This would cause the calculated surface area to be slightly different than the actually fracture surface area because of the porosity. This effect of porosity can be seen in the difference between the values calculated for the little/no pores and large pores values of the stress where the little/no pores values are twice that of the large pores values for the fracture stress. Also the calculations assume a perfectly flat surface which is not the case examining the fracture surface images of the microcantilever which can be seen in Figure 3.9c. These deviations from a perfectly flat surface will also have an effect in the values calculated for the microcantilevers.

Considering the technical difficulties on these samples one can come to the conclusion that this type of testing may not be suitable for these samples. These artifacts encountered make it rather difficult to interpret the intrinsic behavior of the material. Nonetheless once can clearly see the influence these microstructural features have on the data that is calculated with these microcantilevers. While the microcantilevers had challenges on this samples it could be possible to use these techniques on samples with significantly large grain sizes. The larger grain sizes would remove the effects of having multiple grains in the mircocantilever. The larger grains would allow for the entire microcantilever to be milled in a single grain and could include the possibility of greatly exceeding the L/H of 5 to better match the assumptions of slender beams and a clamped end. In addition, to removing the effects of grain boundaries it would allow for the ability to study the internist material scatter by milling multiple microcantilevers in the same orientation. Having larger grains will allow better selection of the manufacturing area which could help reduce the probability that a pore is the fracture surface of the microcantilever. Larger grain would have move area to mill which would also decrease the probability that a tested microcantilever would interact with an untested microcantilever. However, even with the low yield of successful tests this

technique did show promise with the elevated temperature testing at 300 ºC and 500 ºC as described in the next section.

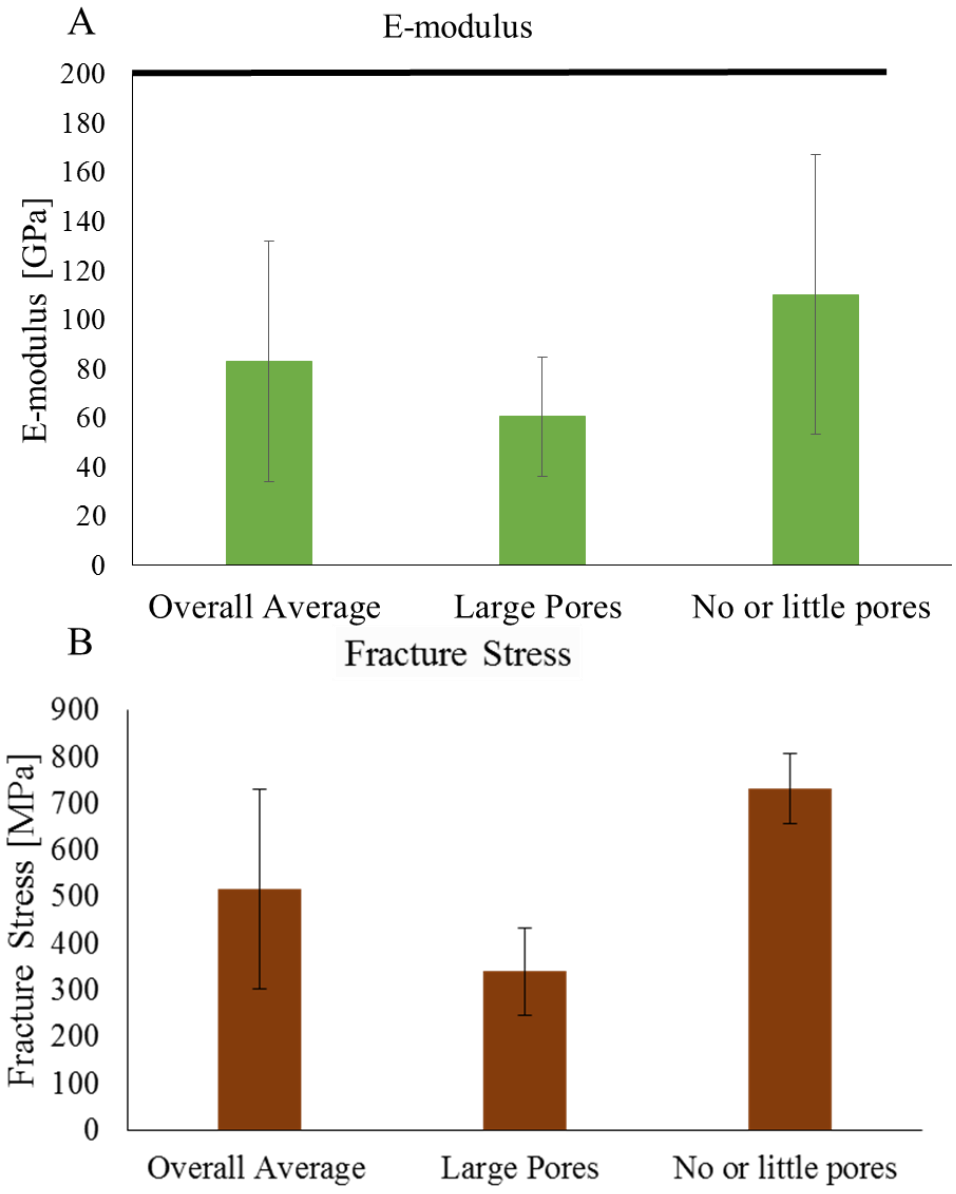

Figure 4.1: A) The elastic modulus values of the ex-situ tested microcantilevers. The values are split between the overall value, microcantilevers with large pores and microcantilevers with no or little pores. The line at 200 GPa is the overall elastic modulus of UO_2. B) The fracture stress values of the ex-situ tested microcnatilevers. The values are split between the overall value, microcantilevers with large pores and microcantilevers with no or little pores.

Ex-situ Temperature Microcantilever Testing Discussion

It can been seen in the 500 ºC ex-situ polycrystalline microcantilever test that there is a deviation from linear loading which could be thermal drift or plasticity in the microcanitlever. The brittle to ductile transition temperature for UO_2 is somewhere between 0.1-0.17 of the melting temperature of UO_2 [125] which is low for ceramics. The melting temperature of UO_2 is 2,865 ºC which makes the transition temperature 287-478 ºC. From this information plus the in-situ elevated temperature tests it is believed that the deviation from linear loading is plastic deformation in the microcantilever before fracture. As this agrees with the 570 ºC in-situ SEM tests. It can also be seen in the 300 ºC microcantilever that there is no deviation from linear loading and the entire loading was linear elastic which is also the case for the in-situ microcantilevers discussed later. These data points would therefore lower decrease the range fro the ductile to brittle transition temperature. The lower end of the temperature from [125] is 0.1 T_m or 287 ºC from these data (ex-situ and in-situ) it could be postulated that the lower end of the temperature range be moved to at least 300 ºC. While these decrease is the range is not significant it still helps better understand when the ductile to brittle transition happens. In addition, a case for the 500 ºC showing ductility is that the calculated elastic modulus from the microcantilever agrees quite well with the literature values for the elastic modulus of UO_2 at that temperature. Also the thermal drift was evaluated and minimized as much as possible before the microcantilever testing. If there was a large thermal drift it would have had effects on the elastic modulus that would have affects the calculated values. The stress values calculated are higher than the values from the macroscale mechanical testing in literature which is also seen with the in-situ microcantilever tests. It is believed that the reason for the increase in the values is because the microcantilevers can be milled in between the large pores of the polycrystalline sample. This ability to mill in between the pores causes the volume which is tested to contain small or no pores. The removal of these larger defects allows for increased value of the fracture stress to be measured. This is the case because ceramics fail by the extension of flaws in the material so macroscale tests fail at the largest flaws in the material. However, in micromechanical testing the specimen is smaller than those flaws which would cause an increase the fracture stress. This can also be seen with the smaller is stronger concept which also supports the microcantilevers having a higher fracture stress compared with the macro scale tests. In addition, elastic modulus values calculated with successful ex-situ polycrystalline samples match quite well with the macroscale literature values at both temperature tested [111]. This demonstrates that small scale mechanical testing has the ability to accurately measure mechanical properties of ceramics at the micron scale at the potential operating temperature of material. This point is only further proven with the in-situ testing and nanoindentation experiments discussed though out this section.

In-situ SEM Microcantilevers

3D EBSD

The 3D EBSD of the microcantilever tested in-situ allowed for a deeper understanding of the effects of the micro structure on the values calculated out of the microcantilevers and the development of the models. In addition, to being able to evaluate the revolution of the grains and

porosity though the microcantilever with the 3D slicing gave the models greater accuracy. The collaborators at ASU were responsible for the modeling of the OU_2 microcantilevers and their work with this data can be seen in Bowen's thesis [35].

Single Crystal

The results of the single crystal in-situ SEM microcantilevers can be seen in Figure 3.13 and 3.14. In these results it can be seen that the fracture stress for the microcantilevers is significantly larger than macro scale mechanical testing of UO_2. The compressive strength of the UO_2 is measured to be around 1 GPa while the bending stress has been measured around 0.2 GPa [118-122]. This means that these results are an order of magnitude higher than the macro scale values. The values for the micro cantilevers were around 3256 ± 532 MPa. While this values are higher than the macro scale values they are not unreasonable as the theoretically values of tensile strength of UO_2 are significantly higher which are in the range 16.4 to 93.6 GPa depending on orientation [126]. It is believed that the higher values of the fracture stress are originating from the density of the UO_2. The single crystal of UO_2 had minimal to no porosity which allowed fully dense microcantilever to be milled in the single crystal while normal large scale tests will always contain some pores. This is also supported by results of the microcantilevers in the polycrystalline porous material which had lower values of fracture stress and were more in line with the macro scale values. In addition, ceramics fail by the extension of pre-existing flaws in the material. These flaws have stress intensity factors that increase the stress at the crack tips which would reduce the overall stress experienced in the bulk of the material. In the fully dense there are no pre-existing flaws in the microcantilevers leading to the higher stress values. These results of the single crystal show that microcantilevers can be useful in measuring the mechanical properties of ceramic materials and heavy metal oxides. The elastic modulus values calculated with these microcantilevers agree well with the theoretical values for these orientations of UO_2 at room temperature. While the fracture stress are higher than the macroscale ceramics the values are not unreasonable and further validate the smaller stronger concept and Weibull distribution where if sample a smaller volume would expect a higher value. In addition, the data fits with the understanding of how ceramics fail in overall sense with the extension of pre-exiting flaws.

In-situ SEM Microcantilever High Temperature Discussion

The brittle to ductile transition temperature for UO_2 is somewhere between 0.1-0.17 of the melting temperature of UO_2 [125] which is low for ceramics. The melting temperature of UO_2 is 2,865 ºC which makes the transition temperature 287-478 ºC. This can be seen in the results of the in-situ microcantilevers. The 300 ºC microcantilevers in-situ SEM still behave in a similar to the room temperature microcantilevers with linear loading and completely elastic behavior until fracture. However the microcantilevers tested at 570 ºC exhibit some ductility in there loading curves with deviations from linear loading. These results aligns well with the brittle to ductile transition range. Since the 570 ºC test are ~100 ºC above the upper limit of the transition range it reasonable that these microcantilevers would exhibit some ductile deformation before fracture of the microcantilever. In addition, 3 different orientation of UO_2 were probed in these experiments [1-21],[-101] and [-412]. Since there is some ductility in the microcantilevers the bending yield stress

and the critical resolved shear stress (CRSS) can be calculated using the 0.2 % offset method and schmid factor respectively. The [1-21] orientation has a strong single slip system active (001)[110] with a schmid factor of 0.47, the [-101] orientation has 4 slip systems active all with a schmid factor of 0.35 and the [-412] (most likely [-413] due to small errors in the EBSD) orientation has two slip systems one with a value of 0.44 and the other with a value of 0.41. The [1-21] orientation had a bending yield stress value of 783 ± 155 MPa, the [-101] orientation had a bending yield stress value of 1579 ± 238 MPa and the [-412/-413] orientation had a value of 1586 ± 384 MPa. The CRSS values for the different orientation are 368 ± 72 MPa for [1-21], 533 ± 83 MPa [-101], and 697 ± 168 [-412/-413]. These values for the CRSS do not agree with each other that well. There could be two things to explain the reason for CRSS values not aligning which are that CRSS is anisotropic or that the slip system is not (001)[110]. In [127] the authors discuss that the CRSS for UO_2 can be anisotropic and orientation depend which would explain the values here not aligning. Another explanation it that a different slip system could be active at these low temperature. In [125] the authors discuss that option that (111) [1-10] slip system could be active at low temperatures. However, if the schmid factors for (111)[1-10] slip systems are examined it does not increase the alignment of the CRSS values for the microcantilever. The CRSS values calculated using the (111)[1-10] family of slip systems are 319 ± 63 for [1-21], 644 ± 97 for [-101] and 744 ± 180 for [-412/-413]. So the reason for the discrepancy of the CRSS values is not completely understood.

4.2 Nanoindentation

Polycrystalline Sample Discussion

The polycrystalline un-strain/fresh sample had nanoindentation performed on it. The elastic modulus values measured using nanoindentation match well with other literature values available [111] over the temperature range tested. It can be seen the hardness decreased significantly over the temperature range tested starting at a value of 10.75 ± 0.95 at room temperature and decreasing to a value of 2.61 ± 0.23 at 500 ºC. The values are room temperature match well with literature values [120, 121]. Studies of nanoindentation at elevated temperature were not found in the literature, however; there was a study performed using Vickers indentation over temperature [128]. The value of the Vickers indents changed to GPa give lower values over the temperature test which could be because of the porosity and larger volume sampled with the Vickers indents. In addition, there could be some effects from the smaller is stronger concept. The nanoindentation results show that nanoindentation could be available tool in evaluating the elastic modulus and hardness of a material when there is a limited amount of material available like neutron irradiated ceramics. The nanoindentation results match literature values well and produced these values even in the ~20 µm grain size porous sample with reasonable values. It could be expected room and elevated temperature nanoindentation could be a valuable tool in measuring the elastic modulus and hardness of neutron irradiated accident tolerant fuels and commercial spent fuel in order to increase the data available for these materials.

Spark Plasma Sintered Samples

Fracture Toughness

As stated above SPS sampels were provided to us from RPI. While it was possible to measure the fracture toughness for the 2 and 10 µm grain size samples it was not possible to measure it for the nanocrystalline (125 nm grain size) material due to the additional cracking that was observed during the fracture toughness measurements as seen in Figure 3.20. In the literature there several reports of increase in the fracture toughness of nanoceramics [129-131]. While it cannot be verified with these experiments that the fracture toughness of nanocrystalline UO_2 is higher this phenomenon has been seen in other UO_2 samples [32, 132] where the nanocrystalline high burn structure formed in the UO_2 has a higher fracture toughness. The phenomenon that cause this increase in the fracture toughness are still worth discussing here. The mechanism that are believed to increase the fracture toughness also are believed to increase the hardness which was seen in these experiments. Nanoceramics usually have 3 characteristics: 1) grains do not exceed 100 nm in size, 2) the volume fraction occupied by grain boundaries and their triple junctions are large, 3) Grain boundaries are short [129-131]. In nanoceramics cracks usually propagate in an intergranular manner instead of a transgranular manner. Due to the high peierls barrier for lattice dislocation slip in ceramics, dislocation slip is suppressed at ambient temperatures. This requires alternative deformation modes mediated by grain and interphase boundaries to come into play. Possible alternative deformation modes would be: 1) grain boundary sliding, 2) grain boundary diffusional creep, 3) triple junction diffusional creep, and 4) rotational deformation mode [129-131]. The grain boundaries in nanoceramics can effectively contribute to toughening of nanocrystalline materials. It is assumed grain boundary sliding in not accommodated at low temperature and is accommodated at high enough temperatures [131]. If the material however is strained at sufficiently low temperature ($T < T_{GBD}$) cracks can initiate grain boundary sliding which leads to the generation of immobile dislocations at the triple junctions of grain boundaries. The grain boundary produced dislocations cause a partial stress relaxation in the vicinity of crack tip which hampers the crack growth in the material [129-131]. Rotational deformation is the deformation accompanied by a change in the orientation of crystal planes in grains [131]. This type of deformation can occur under the action of local shear stresses in the vicinities of crack tips and results in their partial relaxation that increases fracture toughness. The rotational deformation in the nanograins occurs under the action of the applied stress through the formation of immobile disclinations located in the triple junctions of the boundaries of a single nanograin. An illustration of rotation deformation can be seen in Figure 4.2. The model proposed by Morozov *et al.* [133] shows that the presence of rotational deformation can increase the facture toughness by approximately 12% and does not depend on the materials parameters.

It is believed that the due to the large amount of grain boundaries present in the nanocrystalline UO_2 it would be there be multiple path ways for crack propagation and nucleation that would cause the additional crack formation and flaking of material that is seen in Figure 3.20. This would be reasonable as there is a large volume of grain boundaries and triple points in the material and that most nanocrystalline ceramics fail by intergranular fracture caused by the cavitation at grains

boundaries. Having numerous crack initiation points and pathways in the high stress regions of the indenter would allow for multiple cracks to nucleate and propagate in the material which could intersect and cause the phenomenon seen in Figure 4.20. In addition, close examination of the area under the flacks give the impression of intergranular fracture in the material where the flakes have broken off from the material.

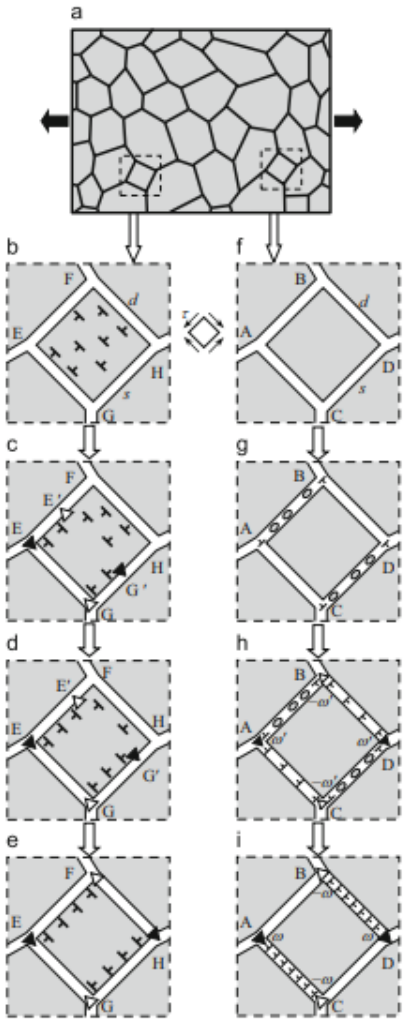

Figure 4.2: Rotational deformation modes in model square grains of a nanocrystalline specimen (schematically). (a) Tensile deformation of a nanocrystalline specimen. General view. (b)–(e) Standard rotational deformation is carried by mobile disclinations (triangles). A quadrupole of disclinations at points E, E0 , G and G0 is formed. The disclinations at points E and G are immobile, while the disclinations at points E0 and G0 move along grain boundaries EF and GH through absorption of lattice dislocations from grain interior. These moving disclinations carry rotational deformation. (f)–(i) Special rotational deformation occurs in a nanograin through formation of immobile disclinations (triangles), whose strengths gradually increase during the formation process conducted by grain boundary sliding and diffusion-controlled climb of grain boundary dislocations. Grain boundary sliding occurs through local shear events (grey ellipses)

in grain boundaries AB and CD. Grain boundary sliding results in formation of grain boundary dislocations at junctions A, B, C and D. Diffusion-controlled climb of the dislocations along grain boundaries AC and BD provides special rotational deformation accompanied by formation and evolution of a quadrupole of wedge disclinations at junctions A, B, C and D [133].

Nanoindentation of SPS Material

It can been seen that the nanocrystalline material had a higher hardness values at all of the temperatures tested compared to the 2 and 10 µm grain size samples. The hardness value for the nanocrystalline UO_2 was 12.47 ± 0.35 GPa which is approximately a 40 % increase over the 2 and 10 µm grain size samples. The nanocrystalline sample maintains it hardness better over the temperature range tested with a hardness of 6.06 ± 0.79 GPa at 600 ºC which a 51 % decrease in the hardness compared with room temperature. While both the 2 and 10 µm sample decreased 79 % in hardness at 600 ºC compared to room temperature. The elastic modulus of all of the samples is approximately the same which is expected and match well with literature values [111]. The increase in hardness in the nanocrystalline UO_2 is not unexpected. It had been shown in literature that materials with smaller grains have an increase in strength [123, 134]. Nanoceramics exhibit an increase in strength because of reduction of flaw size, structural homogenization (leading to reduction of residual stress level), barriers to dislocation motion (large amount of grain boundaries) and crack propagate along grain boundaries compared to intergranular fracture [123, 129-131].

In metals there is the Hall-Petch effect which is that a materials strength increase with decreasing grain size to a point. The dislocation pile up at the grain boundaries which causes an increase in the observed strength of the material. The equation that describes this increase in strength with grain size is shown below in equation 22.

$$H = H_0 + k_y d^{-\frac{1}{2}} \qquad \text{Eq. 22}$$

Where H is the hardness, H_0 is a materials constant for the starting stress for dislocation movement, k_y is the strengthening coefficient and d is the average grain diameter. It is important to note that the Hall Petch relationship is an empirical fit to experimental data. The Hall-Petch relationship has been observed in materials down to grain size of 10 nm after which there is usually a decrease in yield strength with decrease grain size because other deformation mechanisms are available such as grain boundary sliding [129-131, 134]. In this work, there appears to be a Hall-Petch like behavior in the 3 SPS samples that were investigated at the 3 temperatures tested. The plot of the H versus $d^{-1/2}$ can be seen in Figure 4.3 with the linear fits and equations. The calculated H_0 were 8.1249, 3.5635, and 0.9794 at room temperature, 300 º C and 600 º C, respectively. The k_y values show good agreement over the temperature range tested with room temperature having a value of 1.5409, 300 º having a value 1.3889, and 600 ºC having a value 1.7815. There has been work done on evaluating the Hall-Petch relationship with creep data at significantly higher temperatures (> 1000 ºC) [135] that this data would have difficulty comparing to. One relationship with SPS material at room temperature with Vickers indentation converted to GPa was found [136]. In that relationship the authors had calculated a H_0 of 4.7 GPa and a k_y value of 3.25. The reasons for the

difference in this work could be indenter geometry and the lack of dislocation movement at room temperature in the ceramic material. The work here used a berkovich indenter. In addition, the values are converted from Vickers values which samples a larger volume of material compared with nanoindentation. In addition, these are two different samples manufactured with different machines, parameters, locations and purities which all could have an effect on the values of the hardness.

In addition to evaluating the Hall-Petch relationship the relationship between hardness and temperature was evaluated for the 3 SPS samples depending on grain size. The equations that relates temperature and hardness is given by [137, 138] and shown below in equation 23.

$$H = A\exp(-BT) \qquad \text{Eq. 23}$$

Where H is the hardness, A is the extrapolated hardness value at 0 K (called intrinsic hardness), B is the softening coefficient of the material, and T is the temperature in K. In order to evaluate the constants A and B the ln (H) versus Temperature is plotted. This has been done for the 3 different grain size SPS samples as seen in Figure 4.4. It can be observed that the 2 and 10 μm grain size sample match extremely well with both having a slope of 0.0027 for B and ln (A) values being close with the 2 μm sample having a ln (A) value equal to 3.0061 and the 10 μm sample having a value of 2.9585. However, the 125 nm grain size sample had a slope of 0.0012 for B but similar value for ln (A) close to the 2 and 10 μm samples with a value of 2.8323. The difference in slope between the nanocrystalline and the other 2 samples could be different deformation mechanics being activated at different temperatures such as grain boundary sliding or other deformation mechanism described earlier [129-131]. The slopes are similar to the value reported in [139] for pure UO_2. The ability to see the a difference in the softening coefficient agrees well with the hardness data as the nanocrystalline material decrease a different percentage as compared with 2 and 10 μm samples. It would therefore be expect that the samples would have different softening coefficients which would suggest that the materials are deforming with difference mechanism or that the large amount of grain boundary in the nanocrystalline material continue to act as dislocation barriers over the temperature range. The grain boundaries are still strong barriers to dislocation motion over the temperature range that would infer that as the temperature increases in this range there is more deformation inside the grains is occurring. While this discussion can be verified with this data this phenomenon could be of interest for further investigation as the deformation at the sub-grain level is of interest for modeling applications of fuel.

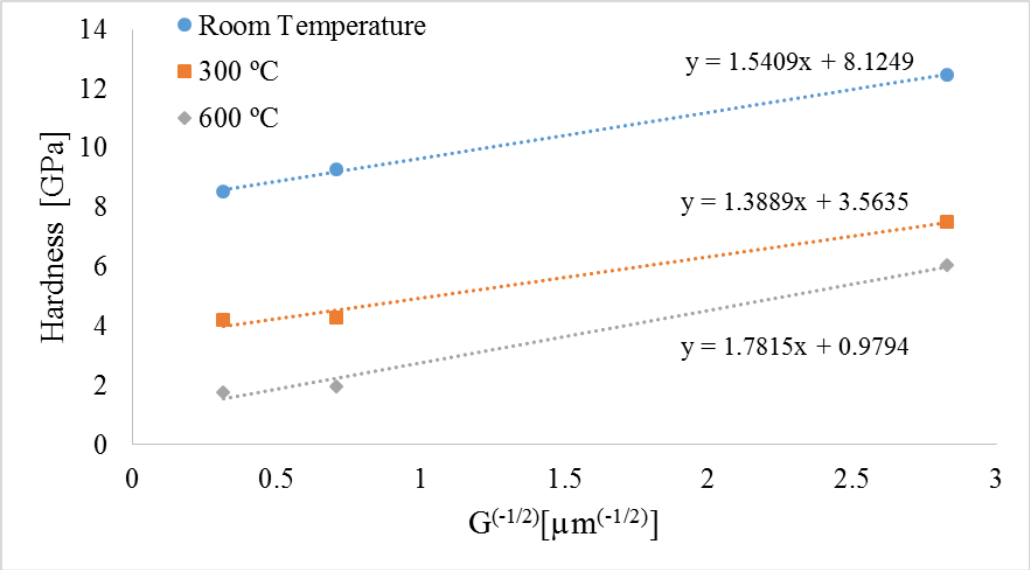

Figure 4.3: A Plot of the grain diameter raised to (-1/2) power versus the hardness of 3 different samples from RPI at the 3 different temperatures tested.

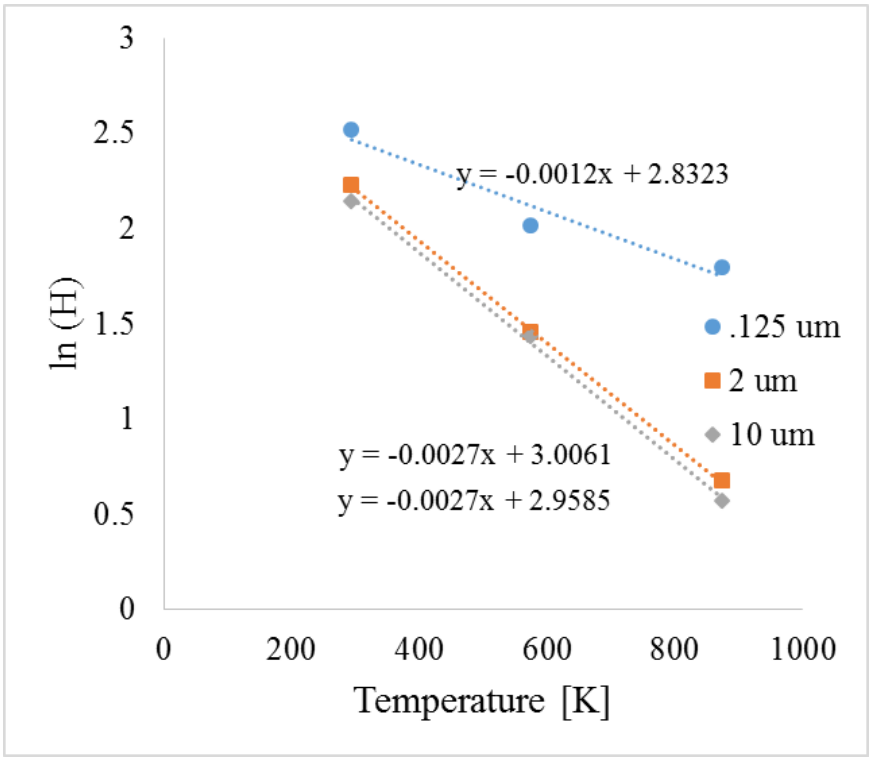

Figure 4.4: A plot of Ln (hardness) versus the temperature to evaluate the change in hardness with temperature. In addition it allows the calculation of the intrinsic hardness and softening coefficient.

Discussion pre-strained condition

The structure of the dislocation core in ceramics depend on three factors: 1) Charge of the ions, 2) Size of the ions, and 3) Presence of directional bonds. At lower temperature the nucleation and formation of dislocations in UO_2 is difficult [125]. It can be seen that the pre-strained material had lower hardness values at all of the tested temperatures, which suggests and aggress with [125] that plasticity in UO2 at lower temperatures might be hindered by the energetic barriers to dislocation nucleation. It is believed that the additional dislocations introduced in the sample from the deformation cause the decrease in the hardness [140-142]. It would increase density of dislocations in the material and therefore not as many would need to be nucleated for the deformation to occur. It has been seen in irradiated UO_2 that there is an initial increase in the hardness in the material from irradiation however once larger doses are reach there is a reduction of the hardness of the UO_2 [75]. While fission and neutron damage would not necessary cause the same damage in UO_2 as a compressive load it does show that additional defects in the UO_2 can cause a reduction in hardness. The decrease in hardness was 12 %, 19 %, 29 % and 12 % for room temperature, 100 ºC, 300 ºC, 500 ºC respectively. These percentage decrease in hardness illustrate that the highest reduced in hardness was around 300 ºC. This is right at the beginning of the potential ductile to brittle transition range 287-478 ºC. The nanoindentation creep data will be discussed in the next section but an important results is the stress exponent for 300 ºC tests starts at above 10 for the fresh/unstrained materials and decrease to ~7 for the pre-strained material. This illustrates that pre-strained material has dislocation motion possible at the stress in the nanoindentation creep case. This could show that the reduction in hardness is because of the ability to move the dislocations at the stress and temperatures. The high hardness is because of the need to nucleate the dislocations to allow the deformation to happen. The thermal assistance from the temperature and the stress at 300 ºC allows for the decrease in hardness because the pre-strained material already has the dislocations present to allow for the deformation of the material. The reason for the reduction in the percentage decrease at 500 ºC is that dislocations can easily be nucleated and moved at that temperature. It will be seen that both the fresh/unstrained materials and pre-strain material at 500 ºC had stress exponents below 10. This also strengths the argument that plasticity at lower temperatures is hinder by energy to nucleate of dislocations. The reduction for room temperature and 100 ºC was not as large as 300 ºC because it still required high stress to move the dislocations and since they did not have as much thermal assistance.

The change in the hardness over temperature for both the pre-strained and un-strained/fresh samples was plot same as for the PRI. The softening coefficient for both samples were 0.0029 which agrees well with micron grain size samples from RPI which had a softening coefficient of 0.0027. In addition the intrinsic hardness of the pre-strain was 22.1 GPa and the un-strained/fresh sample it was 26.5 GPa which matches well with the RPI samples. The plots for these two samples can be seen in Figure 4.5.

In addition, the ability to measure the change in the hardness for the different grains size and pre-strained and un-strained material again illustrates the nanoindentation can be a valuable tool to measure the elastic modulus and hardness of materials with limited volumes. Also since nanoindenation samples a small volume it can be used to measure the difference in the mechanical

properties along the length of the spent fuel pellet. This could allow for the investigation of the mechanical properties in different region based on the different microstructures which is not possible with conventional macroscale mechanical testing due to pellets cracking, high level of radioactivity, and size of specimen need for macroscale mechanical testing. The use of this technique of neutron irradiated fuel could greatly decrease the post irradiation examination time while allowing more information to be gathered from a single specimen. Also since the reduced size samples would have the potential to be removed from hot cells which would greatly reduce the cost of work with the sample.

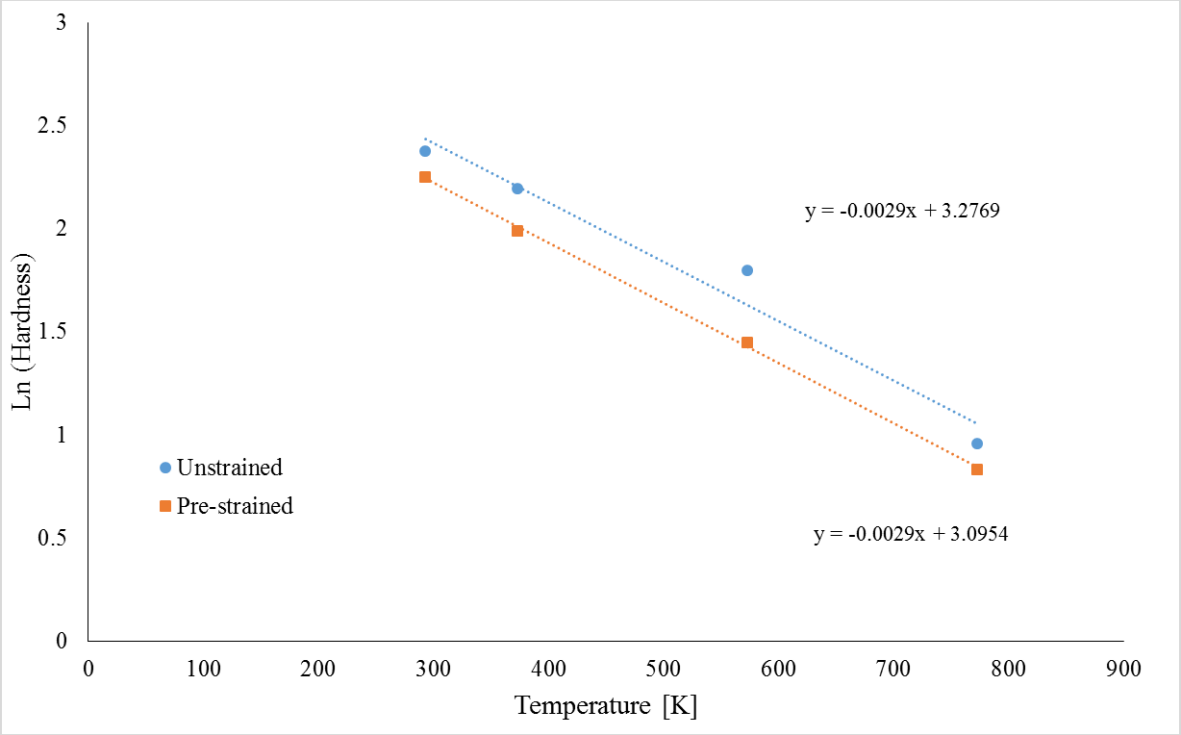

Figure 4.5: The ln(hardness) versus temperature for the un-strain/fresh and pre-strained sample to evaluate the softening of the two different materials.

Nanoindentatoin Creep Discussion

The n values for unstrained and prestrained values are high because most of the creep was dislocation motion since it was taking place a low temperatures and high stress. The reason for the increased creep rates for the pre-strain samples are same as summarized in the previous hardness section which is an increase in the defect density because of the deformation and that plasticity is hinder at lower temperature because of the energetic barriers to dislocation motion. The addition of dislocations allowed for dislocation motion and gave enough statistically necessary dislocations to allow plastic deformation to occur. The can be seen with the difference in the stress exponents of the unstrained and pre-strained samples at 300 ºC. It is believed that the same phenomenon that decreased the hardness of the pre-strained material also increased the creep rate and lowered the n values which will be shown in this section. The stress exponents for the pre-

strained sample were 8.83 ± 0.21 at 300 ºC and 4.65 ± 0.14 at 500 ºC. The stress exponents for the un-strained/fresh sample were 17.16 ± 2.87 at 300 ºC and 7.28 ± 1.04 at 500 ºC. By examining the errors and the creep curves it can be seen that the pre-strained samples had more uniformed behavior at both temperatures. The more uniform behavior could because of the increase of the dislocation density in the samples because of the pre-straining. The value range for dislocation creep is 3-8 [84-89]. Addition sources have but the range for dislocation creep at 3-10 [86, 88]. When the stress exponent is large (n > 10) it is typical explained by introducing a "threshold stress" below which creep cannot be measured. The values of the exponents would indicate that the pre-strained sample is deforming by dislocation creep at both temperatures. The un-strained/fresh sample appears to be deforming by dislocation creep at 500 ºC while at 300 ºC it appears that there is little to no creep. The value of n in 300 ºC unstrained experiment is quite large which would indicate that there is threshold stress for creep to occur. This can be seen in the curves at 300 ºC in Figure 3.22 where there is no/little change in displacement during the second stage creep segment. It would also appear that value ~ 6 GPa is not above the threshold to cause creep at this temperature. The pre-strained material also has lower n values at both temperatures. While it is difficult to compare this n values with literature values as most creep testing of UO_2 is performed at > 1000 ºC, low stress (compared to these experiments) and in a uniaxial fashion it can be seen that the 500 ºC pre-strain values are in the range of macroscale creep experiments [143-149]. It can be seen with the un-strained/fresh fuel that the n values are headed in the right direction and make sense with the values of the macroscale tests. The brittle to ductile transition temperature for UO_2 is somewhere between 0.1-0.17 of the melting temperature of UO_2 which is low for ceramics. The melting temperature of UO_2 is 2,865 ºC which makes the transition temperature 287-478 ºC. This could help explain why the 500 ºC un-strained/fresh sample has n value that is when the range for dislocation creep while the 300 ºC sample has an extremely large n value as it would require high stresses to move dislocations in the material. This would again support increasing the lower value of this range to 300 ºC as while the microcantilever tested earlier. In the 500 ºC case the sample is above this transition temperature range and dislocations have the thermal energy for mobility and nucleation to allow deformation to occur. The ability to calculate stress exponents with nanoindentation and see differences with different materials would be extremely useful when evaluating the mechanical properties of spent nuclear fuel as the as the creep behavior of is important for modeling and understanding the pellet clad mechanical interactions.

4.3 Transmission Electron Microscopy

In-situ TEM Microcantilevers at Room Temperature Discussion

As with the ex-situ and in-situ microcantilevers at room temperature the in-situ TEM microcantilevers failed in a brittle mode. It can even be seen in one test that a visible dislocation did not move during the bending test and the cantilever failed in a brittle manner. It is believe that the high pieriels stress need to move a dislocation in UO_2 is the cause for the brittle failure [141, 150]. In [141, 150] the CRSS to move at dislocation is greater than 2 GPa at room temperature. The dislocations in this experiment experienced a stress of ~ 1 Gpa. So the results of this experiment agrees with what is expected in the literature from modeling efforts. The sample failed

in a brittle manner just like the microcantilever specimens did. This is was also observed in the in-situ TEM nanoindentation. It has been shown in literature that the high stress field caused by indentation can cause dislocation motion in otherwise brittle materials [151]. It was thought that same approach could be used here to observe dislocation motion and then characterize the dislocations. It was expected that the nanoindentation tip could produce stress fields that were greater than 2 GPa necessary to move a dislocation at room temperature. However, instead the foils failed by cracking instead of dislocation motion. It is believed that since the indenter is no longer constrained as is the case with an indent into the bulk material it did not exhibit plastic deformation. Even though the material was thinned to electron transparency the UO_2 exhibited deformation mode and results that were similar to macroscale testing illustrating that this technique could be valuable tool in evaluating ceramics deformation and behavior.

In-situ TEM Microcantilevers at Room Temperature Implanted with Helium Discussion

The helium implanted in-situ TEM microcantilevers did exhibit a difference in deformation behavior with dose. The 1E18 ions/cm^2 dose sample failed with some pseudo-plasticity. The 1E17 ions/cm^2 dose sample behaved similarly to the room temperature unimplanted samples. For the 1E17 ions/cm^2 it is believed that the bubbles were not large enough or had a high enough density to effect any changes in the behavior of the foils. However the 1E18 ions/cm^2 crack deflection can be seen along with a pseudo-plasticity in the test. It is believed that the helium bubbles are large enough and in a high enough density that the UO_2 is more in a foam structure than a solid piece of UO_2. The foam structure means that the ligaments between the bubbles are fracturing [151]. This prevents a crack from unstably propagating through the material as is the case with the 1E17 ions/cm^2 and the unimplanted material. This fracturing of the ligaments causes the crack to defect and allows for multiple crack pathways to form. In addition, the bubbles could blunt the crack tips which causes the multiple path ways and crack deflection to occur. Some care in the interpretation of these results to bulk property characteristics needs to be included as these are thin (electron transparent) foil with large amounts of helium implanted in them. Lastly, the bubbles could nucleate dislocations [151] which would allow for more plastic deformation as it can be seen that the plasticity of UO_2 is hindered at lower temperatures because of the energy need to nucleate dislocations. In the bubbles nucleated dislocations a lower stress it would allow for plastic deformation at room temperature. However due to the ability to see a difference in the deformation at this scale and the fact that the un-implanted cantilevers deformed in a similar manner to the macroscale it possible with further technique development and modeling efforts to use this testing methods with spent fuel to examine the mechanical properties in the different regions of the fuel and minimize the amount of material needed for testing.

Chapter 5

Conclusion

In this work it was shown that small scale mechanical testing at room and elevated temperature can be used to evaluate the mechanical properties of UO_2. Microcantilever and nanoindentation measurements of the elastic modulus agree well with literature values on bulk samples over the temperature tested in this research. In addition, some plasticity could be seen in the in-situ SEM single crystal microcanitlevers at temperatures of 570 ºC before the fracture of the UO_2 which agrees with literature about the brittle to ductile temperature of UO_2 again on bulk samples. The microstructure investigations of the microcantilvers also showed for the polycrystalline material the grains closest to the indented fracture surface had the largest effect on the calculated result and values of the grains and porosity in the nearest 1/3 of the microcanitlever to the indent fracture surface needed to be taken into account. The elevated temperature testing showed that the microcantilevers can be used at high temperature to accuracy measure the elastic modulus of material being tested. The in-situ TEM testing showed that the UO_2 remains brittle at room temperature even when it has been thinned to electron transparency. The in-situ TEM microcantilever testing even showed a dislocation remaining stationary during the test to fracture. In addition, the in-situ TEM studies illustrated how the helium bubbles could affect the deformation of the UO_2 changing the large single brittle failure seen in the unimplanted specimens to the pseudo-plasticity with bubbles deflecting cracks in the UO_2 implanted to 1E18 ions/cm^2.

The nanoindentation results demonstrated that grain size of the UO_2 does have an effect on the hardness and that the smaller grained material (~125 nm grain size) has less of reduction in hardness at elevated temperature compared to the larger grained material. This affect can also be seen in the softening curves of the 3 samples tested with elevated temperature nanoindentation. This can be demonstrating that nanocrystalline material has different deformation mechanism occurring over this temperature range than the larger grained material. It can also be seen that sample that where pre-strained prior to testing had lower hardness over the temperature range that the pre-stained and un-strain samples were tested. This could elucidate that the plasticity of UO_2 might be hindered at lower temperatures because of the energetic barriers to dislocation nucleation.

This work has shown that it possible to test UO_2 and potentially other heavy actinide oxides using small scale mechanical testing and measure accurate values of their mechanical properties. In addition this work has developed the producers for working at elevated temperatures with oxygen sensitive samples and has shown that the oxidation of the samples can be prevented. The technique applied here have shown that even with the small volumes of material probed with these techniques they still produce correct mechanical properties. A benefit of this is that since small volumes are probed it allows for the ability perform these techniques over a sample with a changing microstructure and mechanical properties and have the ability to measure the change as it occurring. This is especially valuable in materials that crack while in operation which could prevent the use of macroscale testing to measure the mechanical properties. In addition, since only limited volumes of material are sampled the size of the sample need can be smaller. This is

especially important for radioactive materials where substantially reducing the size of the sample can greatly reduce the costs in characterizing it. Lastly, with these results it would be possible for this techniques to be applied to neutron irradiated UO_2 or spent UO_2 to measure its mechanical properties.

Chapter 6

References

[1] World Nuclear Association, from http://www.world-nuclear.org/information-library/current-and-future-generation/nuclear-power-in-the-world-today.aspx

[2] IEA, Electricity Information 2015, International Energy Agency, 2015.

[3] Filker, D. "Revival of nuclear power in North American" World Pumps 469 (2005) 38-43

[4] Verbruggen A, Laes E, Lemmens S, "Assessment of the actual sustainability of nuclear fission power" 32 Renewabe and sustainable energy reviews (2014) 16-28

[5] Alonso G, Valle E, "Economical analysis of an alternative strategy for CO+2+ mitigation based on nuclear power" 52 (2013) 66-76

[6] https://www.cbsnews.com/news/nuclear-projects-at-georgias-plant-vogtle-to-continue/

[7] http://valdaiclub.com/a/highlights/five-years-after-fukushima-nuclear-power-sees-unlikely-revival/

[8] Walsk B, "Japan Mulls Nuclear Revival Not Even 3 Years After Fukushima" Science online http://time.com/9684/japan-mulls-nuclear-revival-not-even-3-years-after-fukushima/

[9] Y.Chen, G. Martin, C. Chabert, R. Eschbach, H. He, G. Te "Prospects in China for nuclear development up to 2050" 103 Progress in Nuclear Energy 81-90

[10] O. Diaconu, M.T. Maloney "Is Nuclear Power Viable in Russia?" 16 The Electricity Journal (2003) 80-87

[11] M. Sharmina "Low-carbon scenarios for Russia's energy system: A participative backcasting approach" 104 Energy Policy (2017) 303-315

[12] S. Kumar, S. Harikumar, C.S. Varghese, D.K. Shukla "Regulatory aspects of nuclear power program in India" 101 Progress in Nuclear Energy 146-159

[13] R.B. Grover "Green growth and role of nuclear power: A perspective from India" 1 Energy Strategy Reviews (2013) 255-260

[14] Z. Karoutas, J. Brown, A. Atwood, L. hallstadius, E. Lahoda, S. Ray, J. Bradfute "The maturing of nuclear fuel: Past to Accident Tolerant Fuel" 102 Progress in Nuclear Engergy (2018) 68-78

[15] K. Terrani " Accident tolerant fuel cladding development: Promise, status, and challenges" Journal of Nuclear Materials (2018)

[16] https://www.atomicheritage.org/history/chicago-pile-1

[17] Stephen M. Goldberg and Robert Rosner " Nuclear Reactors: Generation to Generation" American Academy of Arts &Sciences

[18] "Structural Materials for Generation IV Nuclear Reactors" Editor Pascal Yvon, Woodhead Publishing Series in Energy, 2017

[19] G. Locatelli, M. Mancini, N. Todeschini "Generation IV nuclear reactors: Current status and future prospects" Energy Policy 61 (2013) 1503-1520

[20] https://www.atomicheritage.org/history/chicago-pile-1

[21] https://newnuclearenergy.files.wordpress.com/2011/12/020-i-nuclear-pwr_large2.png

[22] http://www.latimes.com/business/la-fi-diablo-canyon-nuclear-20180111-story.html

[23] http://www.bertrandbarre.com/diffenergie_en_nucpow05.htm.

[24] Reprinted from U.S. Department of Energy, Office of Nuclear Energy, "Generation IV Nuclear Energy Systems: Program Overview" (Department of Energy, n.d.), http://nuclear.energy.gov/genIV/neGenIV1.html

[25] Paul Breeze. Nuclear Power academic press is an imprint of Elsevier

[26] Keith J, Laidler and John M Meiser, Physical Chemistry (Benjamin/Cummings 1982) pp18-19

[27] Advanced Structural Ceramics, First Edition. Bikramjit Basu, Kantesh Balani. © 2011 The American Ceramic Society. Published 2011 by John Wiley & Sons, Inc.

[28] http://metalclaymag.blogspot.com/2011/06/understanding-metal-clay-sintering.html

[29] Z.A. Munir, U. Anselmi-Tamburini, M. Ohyanagi "The effect of electric field and pressure on the synthesis and condolidation of materials: A review of the spark plasma sintering method" J. Mater. Sci. 41 (2006) 763-777

[30] X. J. CHEN, K. A. KHOR, S . H. CHAN and L. G. Y U, Mater. Sci. Eng. A374 (2004) 64

[31] H. FURUHASHI and O. OHHASHI, J. Jpn. Instit. Metals 67 (2003) 448

[32] D. KUSANO and Y. HORI, ibid. 66 (2002) 1063

[33] R. M. GERMAN, Sintering Theory and Practice, (Wiley, New York, 1996) p. 482.

[34] M. TOKITA, Mater. Sci. Forum 308–311 (1999) 83.

[35] Z. SHEN, M. JOHNSSON, Z. ZHAO and M. NYGREN, J.Amer. Ceram. Soc. 85 (2002) 1921.

[36] D. ZHANG, Z. F U, R. YUAN and J. GUO, in Multiphased Ceramic Materials, edited by W. H. Tuan and J. K. Guo (Springer, Berlin, 2004) p. 65

[37] M. NYGREN and Z. SHEN, Solid State Sci. 5 (2003) 125.

[38] S . W. WANG, L. D. CHEN, T. HIRAI and Y. S . KANG, J. Mater. Sci. Lett. 18 (1999) 1119.

[39] G. XIE, O. OHASHI, K. CHIBA, N. YAMAGUCHI, M. SONG, K. FURUYA and T. NODA, Mater. Sci. Eng. A359 (2003) 384.

[40] H. B. HUNTINGTON, in "Diffusion in Solids", edited by A. S. Nowick and J. J. Burton (Academic Press, New York, 1975) p. 306.

[41] P. ASOKA-KUMAR, M. ALATALO, V. J. GOSH, A. C. KRUSEMAN, B. NIELSON and K. G. LYNN, Phys. Rev. Lett. 77 (1996) 2097

[42] J. E. GARAY, S . C. GLADE, U. ANSELMI-TAMBURINI, P. ASOKA-KUIMAR and Z. A. MUNIR, Appl. Phys, Lett. 85 (2004) 573.

[43] Yeo S, McKenna E, Baney R, Subhash G, Tulenko J. Enhanced thermal conductivity of uranium dioxide–silicon carbide composite fuel pellets prepared by Spark Plasma Sintering (SPS). J Nucl Mater 2013;433(1–3):66–73.

[44] Z. Chen, G. Subhash, J.S. Tulenko "Raman spectroscopic investigation of graphitization of diamond during spark plasma sintering of UO_2-diamond composite nuclear fuel" J. Nucl. Mater. 475 (2016) 1-5

[45] D.S. Tucker, Y. Wu, J. Burns "Uranium migration in spark plasma sintered W/UO_2 CERMETS" J. Nucl. Mater. 500 (2018) 141-144

[46] L. Ge, G. Subhash, R.H. Baney, J.S. Tulenko "Influence of processing parameters on thermal conductity of uranium dioxide pellets prepared by spark plasma sintering" J. Euro Ceram. Soc. 34 (2014) 1791-1801

[47] T. Yao, S.M. Scott, G. Xin, J. Lian "TiO_2 doped UO_2 fuels sintered by spark plasma sintering" J. Nucl. Mater. 469 (2016) 251-261

[48] A.H. Heuer, R.J. Keller, T.E. Mitchell *Deformation processes in Minerals, Ceramics and Rocks Chapter 15: On the slip systems in uranium dioxide* D.J. Barber, P.G. Meredith Unwin Hyman Ltd.

[49] L.B. Skinner, C.J. Benmore, J.K.R. Weber, M.A. Williamson, A. Tamalonies, A. Hebden, T. Wiencek, O.L.G. Alderman, M. Guthrie, L. Leibowitz, J.B. Parise " Molten uranium dioxide structure and dynamics" 346 Science (2014) 984-987

[50] G. Leinder, T. Cardinaels, K. Binnemans, M. Verwerft "Accurate lattice parameter measurements of stoichiometric uranium dioxide" 459 J. Nucl. Mater. (2015) 135-142

[51] D.R. Olander *Fundamental Aspects of Nuclear Reactor Fuel Elements* NTIS (1976)

[52] D.D. Baron, L. Hallstadius " Fuel Performance of Light Water Reactors (Uranium Oxide and MOX)"

[53] M.S. Veshchunov, V.I. Tarasov "Modelling of pore coarsening in the high burn-up structure of UO_2 fuel" 488 J. Nucl. Mater. (2017) 191-195

[54] V.V. Rondinella, T. Wiss "The high burn-up structure in nuclear fuel" (13) Mater. Today (2010) 24-32

[55] V.G. Baranov, A.V. Lunev, A.V. Tenishev, A.V. Khlunov "Interaction of dislocations in UO_2 during high burn-up structure formation" (444) J. Nucl. Mater. (2014) 129-137

[56]https://www.survivalistboards.com/showpost.php?p=1890873&postcount=17 visited: 7/13/2018

[57] D. Olander "Nuclear Fuels – Present and future" (389) J. Nucl. Mater. (2009) 1-22

[58] I. Fritz "Elastic Properties of UO_2 at high pressure" J. Appl. Physi. 4353-4353

[59] B. Gong "Finite Element Analysis of Micro-cantilever Beam Experiments in UO_2" (2015) ASU Thesis

[60] M. Salvo, J. Sercombe, J. Menard, J. Julien, T. Helfer, T. Desoyer "Experimental characterization and modelling of UO2 behavior at high temperatures and high strain rates" J. Nucl. Mater. 456 (2015) 54-67

[61] X. Iltis, N. Gey, C. Cagna, A. Hazotte, Ph. Sornay "Microstructural evolution of uranium dioxide following compression creep tests: An EBSD and image analysis study" J. Nucl. Mater. 456 (2015) 426-435

[62] Z.J. Wang, F.I. Allen, Z.W. Shan, P. Hosemann "Mechanical behavior of copper containing a gas-bubble superlattice" 121 Acta Meteria. (2016) 78-84

[63] J.L. Cao, W.T. Geng "Migration of helium-pair in metals" 479 J. Nucl. Mater. (2016) 12-25

[64] Z. Talip, T. Wiss, E.A. Maugen, J.Y. Colle, P.E. Raison, E. Gilabert, M. Ernstberger, D. Staicu, R.J.M. Konings "Helium behavior in stoichiometric and hyper-stoichiometric UO_2" 34 J. Euro. Ceram Soc. (2014) 1265-1277

[65] C. Ferry, J.P. Piron, A. Ambard "Effect of helium on the microstructure of spent fuel in a repository: An operational approach" 407 J. Nucl. Mater. (2010) 100-109

[66] C. Dethloff "Modeling of helium bubble nucleation and growth in neutron irradiated RAFM steels" Dissertation, Karlsruher Institut für Technologie (KIT) Fakultät für Maschinenbau Tag der mündlichen Prüfung: 20. Juli 2012

[67] J. Pelleg *Deformation in ceramics. In: Mechanical Properties of Ceramics. Solid Mechanics and Its Applications*, (213) Springer, Cham (2014)

[68] A.H. Heuer, R.J. Keller, T.E. Mitchell *Deformation processes in Minerals, Ceramics and Rocks Chapter 15: On the slip systems in uranium dioxide* D.J. Barber, P.G. Meredith Unwin Hyman Ltd.

[69] P. Hosemann "Small-scale Mechanical testing on nuclear materials: bridging the experimental length-scale gap" 143 scripta materialia (2018) 161-168

[70] M.A. Kirk, M. Li, D. XU, B.D. Wirth "Predicting neutron damage using TEM with in-situ ion irradiation and computer modeling" 498 J. Nucl. Mater. (2018) 199-212

[71] N. Galy, N. Toulhoat, N. Moncoffre, Y. Pipon, N. Bererd, M.R. Ammar, P. Simon, D. Deldicque, P. Sainsot, "Ion irradiation to simulate neutron irradiation in model graphites: Consequences for nuclear graphite" 408 Nucl. Instr. Meth. Phys. Res. B (2017) 235-240

[72] H.T. Vo, A. Reichardt, D. Frazer, N. Bailey, P. Chou, P. Hosemann, "*In situ* micro-tensile testing on proton beam-irradiated stainless steel" 493 J. Nucl. Mater. (2017) 336-342

[73] Personal communication with Peter Hosemann and Hi Vo.

[74] D. Frazer, M.D. Abad, D. Krumwiede, C.A. Back, H.E. Khalifa, C.P. Deck, P. Hosemann "Localized mechanical property assessment of SiC/SiC composite materials" 70 Compos. Part A: Appl. Sci. Manuf. (2015) 93-101

[75] J. Spino, J. Cobos-Sabate, F. Rousseau "Room-temperature microindentation behaviour of LWR-fuels, part 1: fuel microhardness" J. Nucl. Mater. 322 (2003) 204-216

[76] F. Cappia, D. Pizzocri, M. Marchetti, A. Schubert, P Van Uffelen, L. Luzzi, D. Papaioannou, R. Macian-juan, V.V. Rondinella "Micoharndess and Young's modulus of high burn-up UO_2 fuel" J. Nucl. Mater. 479 (2016) 447-454

[77] J.M. Wheeler, D.E.J. Armstrong, W. Heinz, R. Schwaiger, "High Temperature nanoindentaiton: The start of the art and future challenges" 19 Curr. Opin. Solid State Mater. Sci. (2015) 354-366

[78] K.W. McElhaney, J.J. Vlassak, W.D. Nix, "Determination of indenter tip geometry and indentation contact area for depth-sensing indentation experiments" 13 J. Mater. Res. (1998) 1300-1306

[79] W.C. Oliver, G.M. Pharr, "An improved technique for determining hardness and elastic-modulus using load and displacement sensing indentation experiments" 7 J. Mater. Res. (1992)1564–1583.

[80] http://www.micromaterials.co.uk/

[81] https://www.hysitron.com/

[82] M. Wheeler, R.A. Oliver, T.W. Clyne "AFM observation of diamond indenters after oxidation at elevated temperatures" Diam Relat Mater, 19 (2010), pp. 1348-1353

[83] Ashby, Michael F.; Jones, David R. H. (1980). Engineering Materials 1: An Introduction to their Properties and Applications. Pergamon Press. ISBN 0-08-026138-8.

[84] S.N.G. Chu, J.C.M. Li, "Impression creep; a new creep test" 11 (1977) 2200-2208

[85] F. Li, Y. Xie, M. Song, S. Ni, S. Guo, X. Liao, "A detailed appraisal of the stress exponent used for characterizing creep behavior in metallic glasses" Materials Science and Engineering: A 654 (2016) 53-59

[86] P. Sudharashan Phani, W.C. Oliver "A direct comparison of high temperature nanoindentation creep and uniaxial creep measurements for commercial purity aluminum" acta materialia 111 (2016) 31-38

[87] A.F. Bower, N.A. Fleck, A. Needleman, N. Ogbonna "Indentatoin of a power law creeping solid" Proc. R. Soc. London Ser. A, 441 (1993) 97-124

[88] C. Su, E.G. Herbert, S. Sohn, J.A. LaManna, W.C. Oliver, G.M. Pharr "Measurement of power-law creep parameters by instrumented indentation methods" J. of the mechanics and physics of solids 61 (2013) 517-536

[89] J. Dean, A. Bradbury, G. Aldrich-Smith, T.W. Clyne "A procedure for extracting primary and secondary creep parameters from nanoindentation data" Mechanics of Materials 65 (2013) 124-134

[90] B.R. Lawn, R. Wilshaw "Indentation fracture: principles and applications" Journal of materials Science 10 (1975) 1049-1081

[91] P. Hosemann, J.N. Martos, D. Frazer, G. Vasudevamurthy, T.S. Byun, J.D. Hunn, B.C. Jolly, K. Terrani, M. Okuniewski "Mechanical characteristics of SiC coating layer in TRISO fuel particles" 442 (2013) 133-142

[92] R.F. Cook, G.M. Pharr :Direct Observation and Analysis of Indentatoin Cracking In Glasses and Ceramics" Journal of the American Ceramic Society 73 (1990) 787-817

[93] K.I. Schiffmann "Determination of fracture toughness of bulk materials and thin films by nanoindentation: comparison of different models" 91 (2011) 1163-1178

[94] J.H. Lee, Y.F. Gao, K.E. Johanns, G.M. Pharr "Cohesive interface simulations of indentation cracking as a fracture toughness measurement method for brittle materials" Acta Materialia 60 (2012) 54448-4567

[95] Y. Feng, T. Zhang "Determination of fracture toughness of brittle materials by indentation" Acta mechanica solid sinica 28 (2015)

[96] Evans,A.G. and Charles,E.A., Fracture toughness determinations by indentation. Journal of The American Ceramic Society, 1976, 59(7-8): 371-372.

[97] M. Sebastiani, K.E. Johanns, E.G. Herbert, G.M. Pharr "Measurement of fracture toughness by nanoindentation methods: recent advances and future challenges" current opinion in solid state and materials science 19 (2015) 324-333

[98] G.M. Pharr, D.S. Harding, W.C. Oliver "Mechanical Properties and deformation behavior of materials having ultra-fine microstructures" M. Nastasi, et al. (Eds.), Kluwer Academic Press (1993), pp. 449-461

[99] D.E.J. Armstrong, A.J. Wilkinson, S.G. Roberts " Measuring anisotropy in Young's modulus of copper using microcantilever testing" Berkeley Library, on 04 Mar 2018 at 00:17:18

[100] Tim Maitland and Scott Sitzman, *Scanning Microscopy for Nanotechnology Techniques and Applications: Chapter 2 Electron Backscatter Diffraction (EBSD) Technique and Materials Characterization Examples* Weilie Zhou and Zhong Lin Wang eds. Springer Science+Business, LLC (2006)

[101] Stokes, Debbie J. *Principles and Practice of Variable Pressure Environmental Scanning Electron Microscopy* (PV-ESEM) John Wiley & Sons (2008)

[102] J. Orloff "Fundamental limits to imaging resolution for focused ion beams" (6) J. Vacu. Sci. Tech. (1996) 3759

[103] https://www.zeiss.com/microscopy/int/products/multiple-ion-beam/orion-nanofab-for-materials.html

[104]V.Veligura,G.Hlawacek,R.vanGastel,H.J.W.Zandvliet,B.Poelsema,BeilsteinJ.Nanotechnol. 3, (2012)501.

[105]V.Veligura,G.Hlawacek,R.P.Berkelaar,R.vanGastel,H.J.W.Zandvliet,B.Poelsema,BeilsteinJ .Nanotechnol.4, (2013) 453.

[106] Kim, Y.S. "A thermodynamic evaluation of the U-O system from UO_2 to U_3O_8" J. Nucl. Mater. 279 (2000) 173-180

[107] D.D. Maio, S.G. Roberts "Measuring fracture toughness of coatings using FIB-machined microbeams" 20 J. Mater. Res. (2005) 299-302

[108] https://www.bruker.com/products/surface-and-dimensional-analysis/nanomechanical-test-instruments/nanomechanical-test-instruments-for-microscopes/pi-85l-sem-picoindenter/overview.html

[109] https://www.bruker.com/products/surface-and-dimensional-analysis/nanomechanical-test-instruments/nanomechanical-test-instruments-for-microscopes/pi-95-tem-picoindenter/overview.html

[110] "Nanofabrication, below 10 nanometer" Materialstoday 15 (2012) 413

[111] D. Varshney, S. Shtiya "Pressure and temperature dependent elastic, mechanical and thermodynamical properties of nuclear fuel: UO_2 and UN_2" 440 J. Nucl. Mater. (2013)

[112] J.W. Wittwer, L.L. Howell "Mitigating the Effects of Local Flexibility at the Built-in End of Cantilever Beams" 71 J. App. Mechan. Transaction of ASME (2004) 748-751

[113] personally communication with Pedro Peralta

[114] J.M. Gatt, J. Sercombe, I. Aurburn, J.C. Menard "Experimental and numerical study of fracture mechanisms in UO_2 nuclear fuel" 47 Eng. Fail. Analy. (2015) 299-311

[115] J.T.A. Roberts and Y. Ueda "Influence of porosity on Deformation and Fracture of UO_2" 55 J. the Ameri. Ceram. Soc. (1972) 117-124

[116] M. Oguma "Microstructure Effects on Fracture Strength of UO_2 Fuel Pellets" 19 J. Nucl. Sci. Tech. (1982) 1005-1014

[117] J.B. Ainscough, P.F. Messer "The room temperature fracture strength of sintered UO_2 rings containing deliberately introduced impurities" 11 J. Mater. Sci. (1976) 767-775

[118] R.F. Canon, J.T.A. Roberts, R.J. Beals "Deformation of UO_2 at High Temperatures" 54 J. The Ameri. Ceram. Soc. (1971) 105-112

[119] W.D. Callister. Fundamentals of Materials Science and Engineering, 2nd ed. Wiley & Sons. pp. 252.

[120] M.S. Elbakjsjwam, Y. Miao, J.F. Stubbins, B.J. Heuser "Mechanical properties of UO_2 thin films under heavy ion irradiation using nanoindentation and finite element modeling" 479 J. Nucl. Mater. (2016) 548-558

[121] K. Kurosaki, Y. Saito, H. Muta, M. Uno, S. Yamanaka "Nanoindentation studies of UO_2 and (U, Ce)O_2" 381 J. Alloys Comp. (2004) 240-244

[122] T.R.G Kutty, K.N. Chandrasekharan, J.P. Panakkal, J.K. Ghosh, " Fracture toughness and fracture surface energy of sintered uranium dioxide fuel pellets" J. Mater. Sci. 6 (1987) 260-262

[123] K. Yamada, S. Yamanaka, M. Katsura "Mechanical Properties of (U, Ce)O_2" 271-273 J. Alloys Compou. (1998) 697-701

[124] K. Kapoor, A. Ahmad, A. Laksminarayana, G.V.S. Hemanth Rao " Fracture properties of sintered UO_2 ceramic pellets with duplex microstructure" 366 J. Nucl. Mater. (2007) 87-98

[125] R.J. Keller, T.E. Mitchell, A.H. Heuer "Plastic Deformation in nonstoichiometric UO_{2+x} single crystals—I. Deformation at low Temperatrues 36 Acta Metall. (1988) 1061-1071

[126] L. Li, W. Bao-Tian, Z. Ping "Ideal Strenghts and Bonding Properties of UO_2 under Tension" 32 Chin. Phys. Lett. (2015)

[127] P.T. Sawbridge, E.C. Sykes "Dislocation glide in UO_2 single crystals at 1600 K" The Phil. Mag. J. Theor. Experi. And Appl. Phys. 187 (1971)

[128] A.K. Sengupta, R.K. Bhagat, T. Jarvis, J.Banerjee, T.R.G. Kutty, K. Ravi, O.L. D'Souza, R. Keswani, M.R. Nair, R. Ramachandran, D.S.C. Purushotham "Some Important properties of Simulated UO_2 fuel" Radiometallurgy Division Government of India Atomic energy commission (1999)

[129] I.A. Ovid'ko, A.G. Sheinerman, E.C. Aifantis "Stress-driven migration of grain boundaries and fracture processes in nanocrystalline ceramics and metals" 56 Acta Metaer. (2008) 2718-2727

[130] S.V. Bobylev, A.K. Mukherjee, I.A. Ovid'ko "Emission of partial dislocation from amorphous intergranular boundaries in deformed nanocrystalline ceramics" 60 Scripta Mater. (2009) 36-39

[131] *Mechanical Properties of Nanocrystalline Materials* editor James C.M. Li Pan Stanford publishing Pte. Ltd. 2011

[132] J. Noirot, L. Desgranges, J. Lamontagne "Detailed charcterisations of high burn-up structures in oxide fuels" 372 J. Nucl. Mater. (2008) 318-339

[133] N.F. Morozov, L.A. Ovid'ko, A.G. Sheinerman, E.C. Aifanties, "Special rotational deformation as a toughening mechanism in nanocrystalline solids" 58 J. Mechan. And Phys. Of Solids (2010) 1088-1099

[134] C. Schuh, T.G. Nieh "Hardness and abrasion resistance of nanocrystalline nickel alloys near the Hall-Petch breakdown regime" Mater. Res. Soc. SYmp. Proc. 740

[135] B. Burton, G.L. Reynolds, J.P. Barnes, "The influence of grain size on the creep of uranium dioxide" 8 J. Mater. Sci. (1973) 1690-1694

[136] L. Ge, G. Subhash, R.H. Baney, J.S. Tulenko, E. McKenna "Densification of uranium dioxide fuel pellets prepared by spark plasma sintering (SPS)" 435 J. Nucl. Mater. (2013) 1-9

[137] K. Itoh, Scientific Paper, Sendai, University Series 1, 12 (1923) 137

[138] V.P. Shishokin, Z. Anor, Chem. 189 (1930) 263

[139] A.K. Sengupta, C.B. Basak, T. Jarvis, R.K. Bhagat, V.D. Pandey, S. Majumdar, "Effect of titania addition on hot hardness of UO_2" 325 J. Nucl. Mater. (2004) 141-147

[140] C.S. Yust, C.J. McHargue "Dislocation substructures in deformed uranium dioxide single crystals" 31 J. Nucl. Mater. (1969) 121-137

[141] P. Fossati, L.V. Brutzel, B. Devincre "Molecular dynamics simulation of dislcations in uranium dioxide" 443 (2013) 359-365

[142] C.S. Yust, J.T.A. Roberts "On the observation of lattice and grain boundary dislocation in UO_2 deformed at high temperatures" 48 J. Nucl. Mater. (1973) 317-329

[143] W.M. Armstrong, W.R. Irvine, R.H. Martinson "Creep deformation of stoichiometric uranium dioxide" 7 J. Nucl. Mater. (1962) 133-141

[144] J.C. Gao, L.F. Wang, Y. Wang, S.F. Wu "High-temperature creep properties of uranium dioxide pellet" 20 Trans. Nonferr. Metals Soc. China (2010) 238-242

[145] M. Ben Saada, N. Gey, B. Beausir, X. litis, H. Mansour, N. Maloufi "Sub-boundaries induced by dislocation creep in uranium dioxide analyzed by advanced diffraction and channeling electron microscopy" 133 Mater. Chara. (2017) 112-121

[146] X. Iitis, M. Ben Saada, H. Mansour, N. Gey, A Hazotte, N. Maloufi " A new characterization approach for studying relationships between microstructure and creep damage mechanisms of uranium dioxide" 474 J. Nucl. Mater. (2016) 1-7

[147] X. IItis, N. Gey, C. Cagna, A. Hazotte, Ph. Sornay "Microstructural evolution of uranium dioxide following compression creep tests: AN EBSD and image analysis study" 456 J. Nucl. Mater. (2015) 426-435

[148] F.A. Mohamed, M.S. Soliman "On the creep behavior of uranium dioxide" 79 J. Nucl. Mater. (1979) 143-153

[149] O.A. Ruano, J. Wolfenstine, J. Wadswoth, O.D. Sherby " Harper-Dorn and power law creep in uranium dioxide" 39 Acta Metall. (1991) 661-668

[150] A. Le Prioux, P. Fossati, S. Maillard, T. Jourdan, P. Maugis "Empirical potential simulations of interstitial dislocation loops in uranium dioxide" 479 J. Nucl. Mater. (2016) 576-584

[151] A.M. Minor, E.T. Lilleodden, M. Jin, E.A. Stach, D.C. Chrzan, J.W. Morris Jr. " Room temperature dislocation plasticity in silicon" 85 (2005) 323-330

[152] M.S. Ding, J.P. Du, L. Wan, S. Ogata, L. Tian, E. Ma, W.Z. Han, J. Li, Z.W. Shan "Radiation-Induced Helium Nanobubbles enhance Ductility in submicron-sized single-crystalline copper" 16 Nano Lett. (2016) 4118-4124